RELIABILITY ANALYSIS OF NATURAL SOIL SLOPE CONSIDERING THE EFFECT OF VEGETATION

Mr. Nguyen Thanh Son
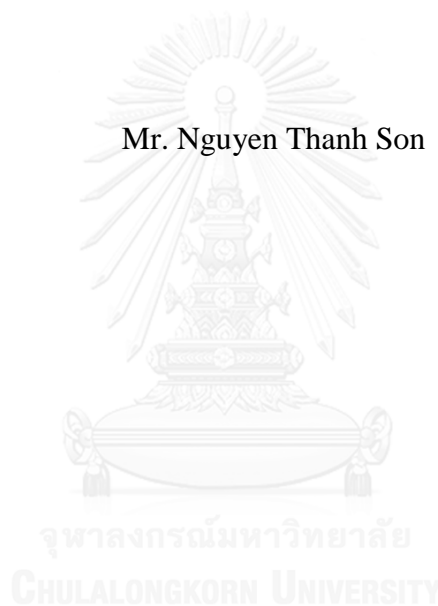
A Dissertation Submitted in Partial Fulfillment of the Requirements
for the Degree of Doctor of Philosophy Program in Civil Engineering
Department of Civil Engineering
Faculty of Engineering
Chulalongkorn University
Academic Year 2016
Copyright of Chulalongkorn University

การวิเคราะห์ความเชื่อมั่นของลาดดินธรรมชาติโดยพิจารณาผลกระทบของพืช

นายเหงียน ทาน ซัน

Thesis Title	RELIABILITY ANALYSIS OF NATURAL SOIL SLOPE CONSIDERING THE EFFECT OF VEGETATION
By	Mr. Nguyen Thanh Son
Field of Study	Civil Engineering
Thesis Advisor	Professor Suched Likitlersuang, D.Phil.

Accepted by the Faculty of Engineering, Chulalongkorn University in Partial Fulfillment of the Requirements for the Doctoral Degree

.... Dean of the Faculty of Engineering
(Associate Professor Supot Teachavorasinskun, D.Eng.)

THESIS COMMITTEE

.... Chairman
(Associate Professor Supot Teachavorasinskun, D.Eng.)

.... Thesis Advisor
(Professor Suched Likitlersuang, D.Phil.)

.... Examiner
(Associate Professor Tirawat Boonyatee, D.Eng.)

.... Examiner
(Associate Professor Boonchai Ukritchon, Sc.D.)

.... External Examiner
(Associate Professor Apiniti Jotisankasa, Ph.D.)

เหงียน ทาน ซัน : การวิเคราะห์ความเชื่อมั่นของลาดดินธรรมชาติโดยพิจารณาผลกระทบ ของ พืช (RELIABILITY ANALYSIS OF NATURAL SOIL SLOPE CONSIDERING THE EFFECT OF VEGETATION) อ.ที่ปรึกษาวิทยานิพนธ์ หลัก: สุเชษฐ์ ลิขิตเลอสรวง, 120 หน้า.

ในช่วงหลายทศวรรษที่ผ่านมา การเปลี่ยนแปลงสภาพภูมิอากาศรวมถึงการเกิดฝนตก หนักส่งผลต่อการวิบัติของลาดดินเป็นจำนวนมาก ปัจจุบันงานวิจัยด้านกลไกการเกิดแผ่นดินถล่ม จากฝนตกมุ่งศึกษาการวิเคราะห์วิบัติของลาดดินด้วยทฤษฎีความน่าจะเป็น การเสริมแรงของราก พืชก็เป็นที่รับรู้กันว่าสามารถช่วยเพิ่มเสถียรภาพของลาดดินได้โดยเฉพาะกรณีลาดดินที่ปกคลุม ด้วยพืช งานวิจัยนี้ดำเนินการศึกษาผลของพืชต่อการวิเคราะห์ความเชื่อมั่นของเสถียรภาพลาดดิน ในการวิเคราะห์ค่าความแปรปรวนเชิงพื้นที่ของคุณสมบัติดินและพืชถูกจำลองด้วยการสุ่มแบบคงที่ ค่าทางสถิติของพารามิเตอร์กำลังรับแรงเฉือนของดินและแรงเชื่อมประสานของรากพืชจะต้อง กำหนดขึ้น กรณีศึกษา 2 พื้นที่ถูกนำมาพิจารณา กรณีแรกเป็นการวิบัติของลาดหินทรายที่ประเทศ ญี่ปุ่น ชุดการวิเคราะห์การไหลของน้ำและเสถียรภาพของลาดดินถูกวิเคราะห์ด้วยเทคนิคการสุ่ม ผล การวิเคราะห์พบว่าการวิเคราะห์ด้วยทฤษฎีความน่าจะเป็นสามารถใช้อธิบายตำแหน่งการวิบัติของ ลาดดินจากความแปรปรวนเชิงพื้นที่ของค่ากำลังรับแรงเฉือนของลาดดินได้ ภายใต้สมมติฐานการ วิบัติแบบลาดอนันต์และเงื่อนไขฝนตก สำหรับกรณีที่สอง เป็นกรณีศึกษาลาดดินที่เกิดอยู่กับที่ใน ประเทศไทย เส้นโค้งลักษณะเฉพาะระหว่างดินกับน้ำและค่าความซึมผ่านได้ของน้ำที่ได้จากผลการ ทดสอบถูกนำมาใช้ในการวิเคราะห์การซึมผ่านได้ของน้ำในดินที่เปลี่ยนแปลงตามเวลา ผลการ วิเคราะห์การซึมผ่านได้ของน้ำถูกนำไปเปรียบเทียบกับค่าแรงดันน้ำที่วัดได้จากในสนาม ค่ากำลัง รับแรงเฉือนของดินและค่าแรงเชื่อมประสานของรากพืชถูกจำลองขึ้นให้สอดคล้องกับกรณีศึกษา ค่าแฟกเตอร์ความปลอดภัยจากการวิเคราะห์เสถียรภาพของลาดดินถูกนำมาเปรียบเทียบระหว่าง กรณีที่เสริมแรงและไม่เสริมแรงด้วยรากพืช นอกเหนือจากนี้ความแปรปรวนเชิงพื้นที่ของค่าแรง เชื่อมประสานของรากพืชได้ถูกนำมาพิจารณาในการวิเคราะห์ด้วย ผลการวิเคราะห์แสดงให้เห็นว่า การกระจายตัวอย่างสม่ำเสมอของรากพืชมีผลต่อการเพิ่มสเถียรภาพของลาดดินที่ปกคลุมด้วยราก พืชอย่างมีนัยสำคัญ

ภาควิชา	วิศวกรรมโยธา	ลายมือชื่อนิสิต	....
สาขาวิชา	วิศวกรรมโยธา	ลายมือชื่อ อ.ที่ปรึกษาหลัก	....
ปีการศึกษา	2559		

5671471521 : MAJOR CIVIL ENGINEERING

KEYWORDS: SLOPE STABILITY, RAINFALL, VEGETATION, PROBABILITY

NGUYEN THANH SON: RELIABILITY ANALYSIS OF NATURAL SOIL SLOPE CONSIDERING THE EFFECT OF VEGETATION. ADVISOR: PROF. SUCHED LIKITLERSUANG, D.Phil., 120 pp.

Over the past decades, effects of climate change including intense rainfalls have resulted in many slope failures. Research activity in understanding the mechanism of rainfall-induced landslides has recently focused on the probability of slope failure. In addition, the effect of root reinforcement on slope stability has been recognized especially for vegetated slope. In this research, a reliability analysis of soil slope considering the effect of vegetation is performed. The spatial variability of soil properties and vegetation is assumed to be modelled as a stationary random field in slope reliability analysis. The shear strength parameters of soil and root cohesion quantified by statistical characteristics are considered. Two natural slopes are selected as case studies. Firstly, a case study of shallow failure located on sandstone slopes in Japan is used to verify the analysis framework. A series of seepage and stability analyses of an infinite slope based on random fields is conducted. The results confirm that a probabilistic analysis can be efficiently used to qualify various locations of failure surface caused by spatial variability of soil shear strength for a shallow infinite slope failure due to rainfall. Secondly, a field monitoring on a residual soil slope in Thailand is modelled. The soil water characteristic curve and the saturated permeability measured from the tests are used in the transient seepage analysis. The results of pore water pressure are compared with the monitored values from the site. The shear strength of soil from the root cohesion is modelled for vegetated soil slope. Factors of safety calculated from transient seepage and slope stability analysis are compared between vegetated and non-vegetated cases. In addition, the effect of spatial variability of root cohesion on probability of slope failure is considered. The results exhibit that a uniform distribution of root can significantly contribute to slope stability especially for the vegetated slope.

Department:	Civil Engineering	Student's Signature	....
Field of Study:	Civil Engineering	Advisor's Signature	....
Academic Year:	2016		

ACKNOWLEDGEMENTS

CONTENTS

List of Tables

Lists of Figures

Notations

A	Total cross-sectional area of the soil
a_i	Mean cross-sectional area of root in size class i
A_j and B_j	Uncorrelated standard normal random variables
A_r	Total cross-sectional occupied by root
c'	Effective soil cohesion
CDF	Cumulative distribution function
c_f	Effective soil cohesion at the failure time
cov	Covariance coefficient of random variables
$Cov[X_1,X_2]$	Covariance coefficient between the input two random variables
c_r	Root cohesion
$E[F]$	Mean of the performance function
FEM	Finite element method
FORM	First order reliability method
FOSM	First order second moment
FS	Factor of safety
$G(\omega)$	Spectral density function
$I[FS(\Omega^k)]$	An indicator function characterizing the failure domain
k	Permeability function

k_s	Saturated permeability
l	Correlation length
LEM	Limit equilibrium method
l_r	Depth of root
MCS	Monte Carlo Simulation
n_i	Number of root in size class i
PDF	Probability density function
P_f	Failure probability
Q	Applied boundary flux (rainfall intensity)
RAR	Root area ratio
S_e	Effective water saturation
τ_f	Shear strength of soil
t_r	Average mobilized tensile strength of roots per unit area of soil
T_{ri}	Tensile strength of an individual root
u_a	Pore air pressure
u_w	Pore water pressure
$Var[F]$	Variance of the performance function
W_i	Weight of each slice per unit base area
$X(z)$	Random field of standard normal distribution

α, m	Fitting parameter of SWCC
β	Reliability index
δ	Angle of deformed roots with regard to shear surface
$\Delta\omega$	The frequency interval of G(ω) domain
ϕ'	Effective friction angle of soil
ϕ^b	Contribution to the shear strength due to soil suction
ϕ_f	Effective friction angle at the failure time
γ	Unit weight of soil
$\gamma(T)$	Variance reduction
μ	Mean of random variable
θ_r	Residual volumetric moisture content
θ_s	Saturated volumetric moisture content
$\rho(l)$	Correlation function
σ	Standard deviation of random variable
σ_n	Normal stress
σ^s	Suction stress
$\Omega(z)$	Random field of lognormal distribution

CHAPTER 1: INTRODUCTION

1.1. Background

Slope instability caused by heavy rainfall events is one of the major problems in geotechnical engineering. This can lead to the collapse of a variety of infrastructures even leading to loss of life. Recently, the use of vegetation to prevent slope instability has been widely applied in many parts of the world because of its relatively low cost, environmental benefits and aesthetics (Gray and Sotir, 1996a; Rahardjo et al., 2012). Most research agrees that contributions of vegetation to reinforce slope stability are well recognised for both hydrological and mechanical effects (Wu et al., 1979; Schmidt et al., 2001; Chirico et al., 2013; Fatahi et al., 2014; Jotisankasa et al., 2014; Leung et al., 2015). In terms of the hydrological effects, an increase in soil suction results when moisture is extracted by plant roots deep in soil which is known as evapotranspiration. The presence of roots in the soil can also affect soil permeability and soil-water retention behaviour (Jotisankasa and Sirirattanachat, 2017). One of the major mechanical effects of roots on slope stability is the process of increasing soil shear strength by providing additional root reinforcement (Coppin and Richards, 1990; Wu, 2013; Eab et al., 2015).

Several studies have investigated the effect of vegetation on slope stability using both the limit equilibrium and finite element method of analysis (Lin et al., 2010; Chirico et al., 2013; Wu, 2013; Tiwari et al., 2013; Leung et al., 2015). The results conclude that root cohesion played an important role in stability analysis. However, such studies have only focused on deterministic analysis, in which root cohesion was characterized by constant values. In fact, the growth of vegetation is affected by various factors, including soil moisture content due to rainfall, type of vegetation, type of soil, and environmental conditions which could cause strong variability of root cohesion in distance or space. Several studies have reported that the majority of root cohesion values of vegetation species fall within the range of 1.0 - 20.0 kPa depending on different environments (O'loughlin, 1974; Kazutoki and Iwamoto, 1986; Abernethy and Rutherfurd, 2001; Simon and Collison, 2002). Schmidt et al. (2001) measured values of root cohesion in the field and the results indicated that variability of root cohesion depended on the presence of one species of vegetation. They found that root

cohesion ranged from 6.8 - 23.2 kPa in industrial forests and 25.6 - 94.3 kPa in natural forests. In addition, Eab et al. (2015) studied the increase of soil shear strength from a vetiver root system using direct shear tests. The results can be used to correlate the root area ratio with the increase of soil shear strength. The vetivers with a root area ratio of 2.44 - 4.37% can increase root cohesion by about 6.0 - 6.8 kPa. Therefore, deterministic analysis of slope stability might lead to conservative results and these results can be underestimated or overestimated in an evaluation of slope failure.

In recent years, many investigators have contributed to understanding spatial variability of soil properties and characteristics of vegetation on slope stability. For example, Fenton and Griffiths (2008) studied the effects of spatial variability of shear strength parameters using a random finite element method. Srivastava et al. (2010) investigated the influence of spatial variability of permeability properties on steady state seepage flow and slope stability analysis. Griffiths et al. (2011) analyzed the failure probability of an infinite slope assuming a random field model of shear strength parameters. Cho (2014) performed a probabilistic stability analysis of rainfall-induced landslides considering spatial variability of permeability. Jiang et al. (2014) used a non-intrusive stochastic finite element to investigate slope reliability considering spatially variable shear strength. A new study by Zhu et al. (2017) also looked into the effect of natural characteristics of vegetation on slope stability considering in particular, the effects of variability in root length. However, these studies ignored the spatial variability of root length in reliability analysis of vegetated slope failure; thus, the spatial variability of root cohesion has not yet been specifically investigated. In addition, slope stability analysis considering the effect of spatial variability of parametric studies (i.e. shear strength parameters, root cohesion) requires a significant development of existing deterministic code for both the limit equilibrium and finite element method of analysis. This is a problem of significant difficulty for most completed problems in engineering fields which are known as coupling analyses between transient seepage and slope stability.

This research aims to examine a slope stability analysis in conditions both with and without the various effects of vegetation during heavy rainfall. Monitoring pore water pressure was possible using the rainfall period record to verify pore water

pressure of the proposed seepage analysis model. Slope stability analysis was then performed considering with the effect of soil suction (pore water pressure), variation of shear strength and root cohesion using the limit equilibrium method. One and two dimensional examples of spatial variation of soil shear strength and root cohesion were simulated with a random field approach, respectively in order to estimate the failure probability of a slope. The effects of soil shear strength variability were quantified to investigate the failure mechanism of a slope and to predict the critical rainfall duration affecting slope failure. In addition, the effect of root cohesion variability caused by root reinforcement in space or distance was also investigated in order to evaluate the contribution of vegetation with respect to the stability of a slope. The unsaturated-saturated seepage analysis and conventional limit equilibrium method were implemented for deterministic analysis while a random field model of soil shear strength parameters and root cohesion were employed in probabilistic analysis to assess the influence of spatial variability on vegetated slope stability.

1.2. Objective of the study

The objectives of this study are summarized as follows:

- To examine and verify the proposed model for seepage analysis and determine the mechanisms of failure of a soil slope caused by heavy rainfall. Two case studies were conducted with and without the effects of vegetation.

- To simulate spatial variability of soil shear strength and root cohesion based on a one and two dimensional random field model, respectively.

- To extend and modify the available computer program of SEEP/W and SLOPE/W modules to consider the effect of spatial variability of root cohesion on failure probability analysis of a natural soil slope.

1.3. Scope of the study

To clarify the research problems, the scope of the study is covered as follows:

- Seepage analysis was conducted for both unsaturated and saturated conditions using the finite element method and the Mualem-van Genuchten model (van Genuchten, 1980).

- The limit equilibrium method was applied for slope stability analysis using the extended Morh-Coulomb criterion.

- Spatial variability of soil shear strength parameters and root cohesion were generated using a random field model and Monte Carlo Simulation.

- Two case studies were conducted on a natural slope: a sandstone slope without vegetation (Japan) and a residual soil slope with vegetation (Thailand).

1.4. Research schedule

Table 1.1. The schedule of the doctoral program

Study Activities	2014												2015												2016												2017				
	Semester 1						Semester 2						Semester 1						Semester 2						Semester 1						Semester 2						Semester 1				
	Jan	Feb	Mar	Apr	May	Aug	Sept	Oct	Nov	Dec			Jan	Feb	Mar	Apr	May	Aug	Sept	Oct	Nov	Dec			Jan	Feb	Mar	Apr	May	Aug	Sept	Oct	Nov	Dec			Jan	Feb	Mar	Apr	May
Course works (subject to university's requirement)	12 units coursework																																								
English Requirement																																									
Qualifying Exam																																									
Explore Research topic	Reading																																								
Thesis Proposal														Frame and draft																											
Data Collection for Thesis																	Data collection																								
Research Analysis																																									
Conference Paper																																									
Journal Article																									The 1st Journal					The 2st Journal											
Thesis Writing																																									
Thesis Defense																																									
Completing Thesis to submit																																									
Thesis Submission																																									

CHAPTER 2: LITERATURE REVIEW

2.1. Introduction

At present, stability analyses of natural slopes are usually marked by the uncertainty of input parameters which are known as the influences of spatial variability of soil properties and characteristics of vegetation. This chapter presents background information on traditional and advanced slope stability, uncertainty in analysis of slope stability, vegetated slope stability analysis, and the random field model of parametric studies.

2.2. Deterministic methods for slope stability analysis

Slope stability analysis is usually used to calculate the safety factor of natural slopes, excavations, embankments, earth dams and landfills. Over the years, many methods have been developed from laborious manual calculations to advanced computer solutions. The following subsections describe the available methods for slope stability analysis.

2.2.1. Limit equilibrium method

In the early years of the 20th century, slope stability analysis used the limit equilibrium method in order to solve the equilibrium problem with assumption of force and/or moment equilibrium. To date, many limit equilibrium methods had been developed and applied, including the ordinary method of slices (Fellenius, 1936), Bishop's modified method (Bishop, 1955), force equilibrium methods (Lowe and Karafiath, 1960), Morgensten and Price's method (Morgenstern and Price, 1965), Spencer's method (Spencer, 1967), and Janbu's generalized procedure of slices (Janbu, 1968) which were all useful for analysis and estimation of slope stability. With respect to the limit equilibrium method, the soil shear strength could be calculated using either total stress or effective stress. For the total stress analysis, pore water pressures were not considered and the soil shear strength was described as undrained shear strength, s_u. For the effective stress analysis, the Mohr-Coulomb failure criterion was used to simulate the soil shear strength as:

$$\tau = c' + (\sigma_n - u_w)tan\phi' \qquad (2.1)$$

where c' is the effective cohesion of soil, σ_n is the normal stress, u_w is the pore water pressure, and ϕ' is the effective friction angle of soil. It should be noted that equation (2.1) is only used in fully saturated soils. For unsaturated-saturated soil conditions, the shear strength of soil can be expressed based on the extended Mohr-Coulomb failure criterion (Fredlund et al., 1978) as:

$$\tau = c' + (\sigma_n - u_w)tan\phi' + (u_a - u_w)tan\phi^b \qquad (2.2)$$

where u_a is the pore air pressure, and ϕ^b is the contribution to shear strength due to soil suction.

In the limit equilibrium method, a slip surface which can be planar, circular or non-circular in shape was assumed to analyze the stability of the slope. The factor of safety (FS) was defined as the ratio between the shear strength of soil to the shear stress and the FS was always constant for the entire slip surface. It should be noted that the limit equilibrium method was implemented within a deterministic framework. This means that the parametric studies used the best estimate value of the available field or laboratory test data (fixed values). In fact, the parametric studies were the uncertain quantity which was associated with the accuracy of the chosen method, the limits of the data, the test equipment and previous experience. Therefore, slope stability analysis using the FS was unsatisfactory for the limit equilibrium method. Hence, it was concluded that a combination of uncertainty and variability in parametric studies with slope stability analysis was required which is known as probabilistic analysis or reliability analysis of slope stability.

2.2.2. Finite element method

Recently, the finite element method (FEM) has been widely used in slope stability analysis due to the fact that available computer software can usually provide a quick and accurate estimation of the FS. In addition, the FEM can solve complex problems of geotechnical engineering. According to Griffiths and Lane (1999), the FEM has several advantages over the limit equilibrium methods:

(1) No assumption is required in advance with respect to the shape of a failure surface. Failure occurs naturally through the zones where the soil elements with shear strength are lower than the applied shear stresses.

(2) There is no need to make assumptions about internal forces, which appears to have been one of the major sources of inaccuracy for some limit equilibrium methods. The FEM preserves global equilibrium until failure is reached.

(3) The FEM provides information about deformations at pre-failure stress levels if realistic soil stiffness parameters are used.

(4) The FEM is able to provide information on progressive failure up to and including overall shear failure.

Several models have used the FEM for slope stability analysis, such as the elasto-plastic soil model conducted by Smith and Hobbs (1974), and the stability of c'-ϕ' slopes given by Zienkiewicz (1975). These studies also indicate that the factor of safety computed by the FEM was in good agreement compared with the limit equilibrium method. Since then, the FEM for slope stability analysis has been reported as the most advantageous method (Lane and Griffiths, 2000; Sainak et al., 2004; Griffiths and Marquez, 2007). In the FEM, the FS of the slope is calculated by trial strength reduction factor in order to find the factored soil shear strength parameter causing the slope failure. The factored soil strength parameters can be obtained from the following:

$$c_f = c' / FS \tag{2.3}$$

$$\phi_f = arctan(tan\phi' / FS) \tag{2.4}$$

where c_f is the effective soil cohesion at the failure time, and ϕ_f is the effective friction angle at the failure time. At the present, the finite element slope stability analysis software is available, for instance, the fourth edition of programming the finite element method (Smith and Griffiths, 2004) and some versions of the program Plaxis.

2.3. Probabilistic slope stability analysis

The calculation of the factor of safety was inadequate to consider the effect of soil variability and other sources causing slope stability uncertainty. Therefore, probability analysis has been adopted as a satisfactory approach to account for the uncertainty and variability of soil properties and other parameters in geotechnical engineering. In the literature, several probability approaches have been presented to estimate failure probability or the reliability index, including: the first order second moment (FOSM), the first order reliability method (FORM), and Monte Carlo simulation (MSC).

2.3.1. First order second moment

The first order second moment (FOSM) is a simple method which accounts for the effects of the variability of random input variables with respect to performance function. This method is based on a first-order of Taylor series expansion of performance function at some points to be evaluated, and the expansion was truncated after the linear term (first order, the mean and standard deviation are defined from the first two moments of the performance function).

The accuracy of the method deteriorates for the second and higher partial derivatives if the performance function is non-linear due to the truncation of the Taylor series after the first order term. Therefore, a few assumptions need to be made to evaluate the partial derivatives and sometimes they can become cumbersome. However, Duncan (2000) demonstrated that FOSM could be applied to many geotechnical problems including slope stability by using this simplified approach.

Consider a performance function $f(X_1, X_2, X_3, ..., X_n)$ of random variables $X_1, X_2, X_3 ... X_n$, the Taylor series expansion is

$$
\begin{aligned}
F = f(\mu_{X_1}, \mu_{X_2}, ..., \mu_{X_n}) + \sum_{i=1}^{n} (X_i - \mu_{X_i}) \frac{\partial f}{\partial x_i} \\
+ \frac{1}{2} \sum_{i=1}^{n} \sum_{j=1}^{n} (X_i - \mu_{X_i})(X_j - \mu_{X_j}) \frac{\partial^2 f}{\partial x_j \partial x_j} + ...
\end{aligned}
\tag{2.5}
$$

The first two moments of performance function:

$$E[F] = \mu_F \approx f(\mu_{X_1}, \mu_{X_2}, ..., \mu_{X_3})$$
(2.6)

$$Var[F] = \sigma_F^2 \approx \sum_{i=1}^{n} \left[\left(\frac{\partial f}{\partial x_i} \right)^2 Var[X_i] \right] + 2 \sum_{i=1}^{n} \sum_{j=1}^{n} \left[\left(\frac{\partial f}{\partial x_i} \frac{\partial f}{\partial x_j} \right) Cov[X_i, X_j] \right]$$
(2.7)

In general, $E[F], Var[F]$ are the mean and variance of the performance function, respectively, $Cov[X_i, X_j]$ is the covariance coefficient between the two random input variables x_i and x_j and n is the number of random variables. The reliability index can be calculated with the equation $\beta = \dfrac{\mu_F}{\sigma_F}$ and the probability of failure $P_f = \phi(-\beta)$, where $\phi(.)$ is the cumulative distribution function (CDF). Applications of the FOSM method for slope stability analysis have been described in previous studies and a detailed formulation of the method can be found in the publications of Fenton and Griffiths (2008).

2.3.2. First order reliability method

Hasofer and Lind (1974) proposed an approach estimating the reliability index which is referred to as the first order reliability method (FORM). The reliability index was estimated by the minimum distance from the origin to a point on the failure criterion. In the FORM approximation, if the vector of random variables has non-Gaussian variables, they would be transformed to the standard normal space U, where U is a vector of the independent Gaussian variables with zero mean and unit standard deviation, and $G(U)$ is a linear function. A model of the FORM is presented in Figure 2.1.
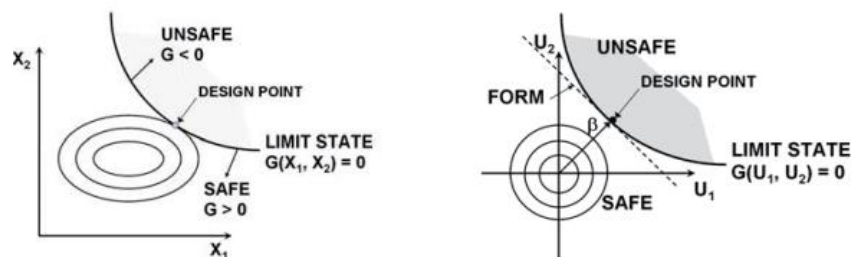
Figure 2.1. FORM approximation for reliability index β

Low (2003) presented a method for finding the reliability index in the original space. His approach was based on the matrix formulation of the Hasofer-Lind reliability index β as follows:

$$\beta = \min_{x \in F} \sqrt{(x - \mu)^T C^{-1} (x - \mu)} \tag{2.8}$$

or, equivalently:

$$\beta = \min_{x \in F} \sqrt{\left[\frac{x_i - \mu_i}{\sigma_i} \right]^T [R]^{-1} \left[\frac{x_i - \mu_i}{\sigma_i} \right]} \tag{2.9}$$

where x is the vector representing the set of random variables, μ is the vector of the mean value, C is the covariance matrix, R is the correlation matrix and F is the failure domain.

Figure 2.2 shows the geometry of a reliability index for a two variables problem which can be interpreted as finding the smallest ellipsoid (the probability distribution of the variables) tangent to the limit state surface. It can be implemented using built-in Excel (Low and Tang, 2004) and Matlab programs.
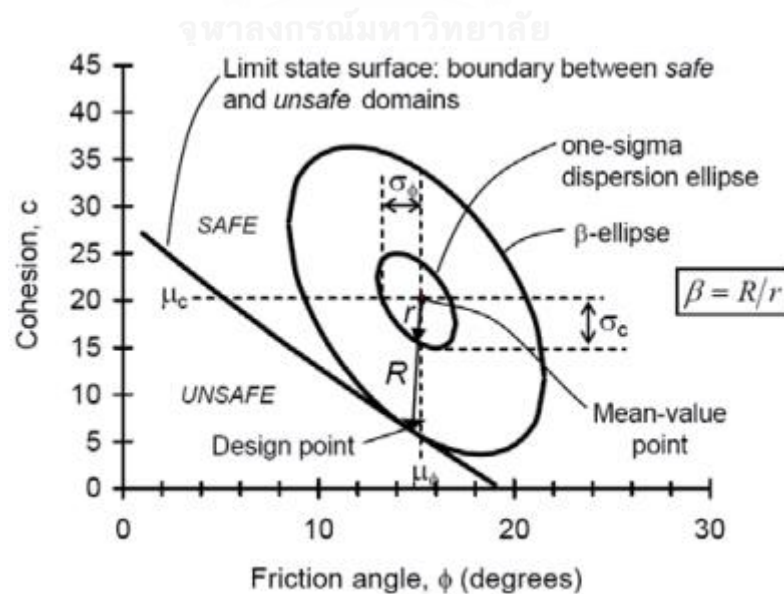
Figure 2.2. Reliability index in the plane of original variables (Low, 2003)

2.3.3. Monte Carlo Simulation

Another way to estimate the mean and standard deviation of performance function is the use of a Monte Carlo simulation (MCS) based on generated random variables of input parameters. The process is repeated thousands of times in order to establish the statistical characteristics of the performance function (FS). The major advantage of this method is that no assumption is required about the shape of the probability distribution of the performance function.

Consider the problem of failure probability of a system which has n random variables X_1, X_2, X_3...,X_n. The performance function $g(X_1, X_2, X_3..., X_n)$ also has random variables because the input parameters are random variables if system failure occurs whenever $g(X_1, X_2, X_3..., X_n) < g_{crit}$, where g_{crit} is the critical value, equal to 1.0. The failure probability can be calculated with n dimensional integral of the joint probability density function $f_{X_1 X_2}(x_1, x_2)$.

$$p_f = \int_{x_1 \in F} \int_{x_2 \in F} \cdots \int_{x_n \in F} f_{X_1 X_2, ..., X_n}(x_1, x_2 ..., x_n) dx_1 dx_2 ... dx_n \tag{2.10}$$

in which F denotes the failure region. Unfortunately, in some cases, the equation (2.10) is complete for analytical solutions and may be difficult to implement in numerical integration algorithms. An alternative solution to evaluate equation (2.10) is simulated by a sequence of realizations of X_1, X_2,..., X_n. $g(X_1, X_2, ..., X_n)$ calculated for each realization. The failure probability can be estimated by an equation called a Monte Carlo simulation as follow:

$$P_f = \frac{1}{n} \sum_{i=1}^{n} I_i \tag{2.11}$$

where $I = 1$ if $g(X_1, X_2, ..., X_n) < g_{crit}$ and $I = 0$ otherwise.

Figure 2.3 illustrates the fundamental issue of the Monte Carlo simulation i.e. that the performance function only includes the two parameters of X_1, X_2. From these two plots, the true failure probability can be $P_f = 0$ or more than zero depending on the

statistical characteristics of input parameters as well as the number of realizations. However, the Monte Carlo simulation is the best method to estimate the failure probability for cases in which there are many independent variables or the performance functions are strongly non-linear. However, it should be noted that the limitation of the Monte Carlo simulation is the number of trials necessary to ensure a desired level of accuracy in the results and how to reduce error in the sampling process or decrease the number of trials necessary to achieve the desired accuracy. This leads to a cumbersome calculation of probability if problems are more complex.
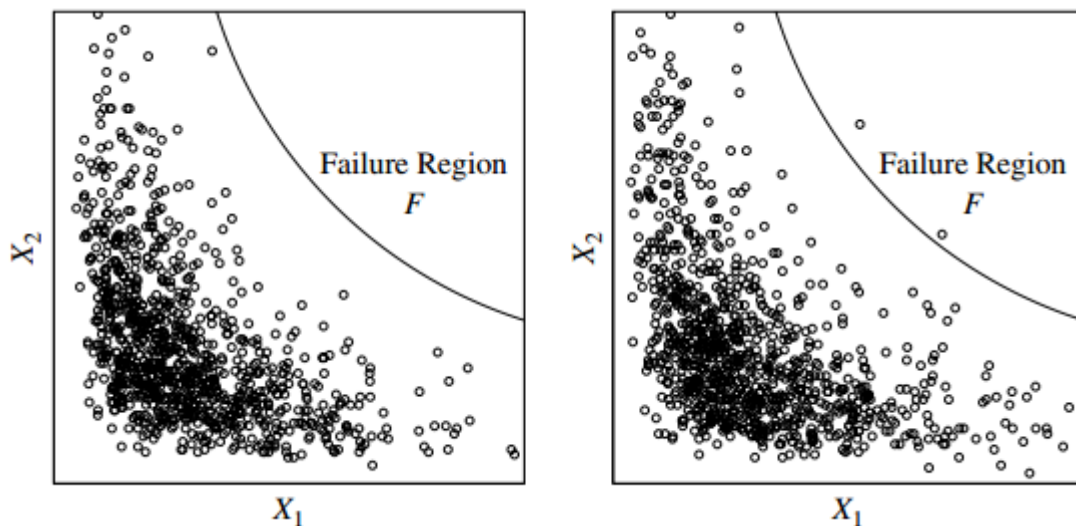
Figure 2.3. Monte Carlo simulation of two parameters X_1, X_2

2.4. Variability of parametric studies

In geotechnical engineering, the properties of natural soils are uncertain and inherently variable from one location to another, even within a relatively homogeneous deposit. According to Vanmarke (1977), the uncertainty of soil properties can be divided into three primary sources: limited sampling data, measurement errors from testing equipment, and empirical error using correlation models relating to the characterization of soil properties. The following section presents methods to quantify the variability of parametric studies and to generate data require to do reliability analysis.

2.4.1. Statistical characteristics

Parametric studies are recognized as random variables. Instead of estimating a deterministic value, an input parametric study of soil property is defined by the statistical characteristics and its probability density function (PDF).

2.4.1.1. Mean of a random variable

The mean is the most important characteristic of a random variable describing its central tendency. For X, a random variable with probability density function *f(x)*, the mean of X (expected value), denoted μ_X, is defined by:

$$\mu_X = E[X] = \sum_{i=1}^{n} x_i f(x_i) \qquad (2.12)$$

if *X* is a discrete function.

$$\mu_X = E[X] = \int_{-\infty}^{+\infty} xf(x)dx \qquad (2.13)$$

if *X* is a continuous function

2.4.1.2. Variance, standard deviation and coefficient of variation of a random variable

The other important characteristics of a random variable are expressed as the distribution if it is wide or narrow around a mean value. This distribution is commonly measured by a quantity called the variance of a random variable.

Similarly, *X* is still a random variable with probability density function *f(x)*. Variance of *X* can be defined by:

$$\sigma_X^2 = Var[X] = E[(X - \mu_X)^2] = \sum_{i=1}^{n} (x_i - \mu_X)^2 f_X(x_i) \qquad (2.14)$$

if *X* is a discrete function.

$$\sigma_X^2 = Var[X] = E[(X - \mu_X)^2] = \int_{-\infty}^{+\infty} (x - \mu_X)^2 f_X(x)dx \qquad (2.15)$$

if X is a continuous function.

The square root of the variance, σ_x^2, is called the standard deviation and the coefficient of variation, cov, is the ratio of the standard deviation to the mean value, as given by:

$$\text{cov} = \frac{\sigma_x}{\mu_x} \tag{2.16}$$

2.4.1.3. Covariance and correlation coefficient of two random variables

Let *X* and *Y* be a pair of random variables with joint probability distribution $f_{XY}(x, y)$ that depend on each other. The covariance, *Cov[X,Y]*, is described by:

$$Cov[X,Y] = E[(X - \mu_X)(Y - \mu_Y)] \tag{2.17}$$

Discrete case:

$$Cov[X,Y] = \sum_{i=1}^{n} \sum_{j=1}^{m} (x_i - \mu_X)(y_j - \mu_Y) f_{XY}(x, y) \tag{2.18}$$

Continuous case:

$$Cov[X,Y] = \int_{-\infty}^{+\infty} \int_{-\infty}^{+\infty} (x - \mu_X)(y - \mu_Y) f_{XY}(x, y) dxdy \tag{2.19}$$

The correlation coefficient between *X* and *Y* is defined as be:

$$\rho_{XY} = \frac{Cov[X,Y]}{\sigma_X \sigma_Y} \tag{2.20}$$

The correlation coefficient has a value from -1 to +1, when the two variables are perfectly related, $\rho_{XY} = \pm 1$, and if the two random variables are independent, $\rho_{XY} = 0$. Table 2.1 presents statistical characteristics of soil shear strength which were conducted from the various laboratory tests.

Table 2.1. Mean and cov of shear strengths parameters (Phoon and Kulhawy, 1999)

Property	Soil type	No. of data group	cov	Mean
c (UC)	Fine grained	38	0.06 - 0.56	101
c (UU)	Clay, silt	13	0.11 - 0.49	33
c (CIUC)	Clay	10	0.18 - 0.42	47
c (TC)	Clay, silt	11	0.08 - 0.38	13
c (DS)	Clay, silt	2	0.19 - 0.20	15
c (LV)	Clay	15	0.05 - 0.37	-
ϕ (TC)	Clay, silt	4	0.07 - 0.56	10
ϕ (DS)	Clay, silt	5	0.03 - 0.29	11
ϕ (DS)	Sand	2	0.13 - 0.14	26
tanϕ (TC)	Clay, silt	4	0.06 - 0.46	-
tanϕ (DS)	Clay, silt	3	0.06 - 0.46	-
tanϕ (TC)	Sand, silt	6	0.02 - 0.22	-
tanϕ (DS)	Clay	6	0.06 - 0.22	-

2.4.2. Spatial variability

Since the characteristics of soil tend to vary from one point to another, the variation of soil in distance or space is known as the spatial variability. A random field model was investigated to describe the correlation structure of soil (Vanmarcke, 1983). In order to simulate a relationship between data points, the Markov correlation function is commonly used in geotechnical engineering (Fenton and Griffiths, 2008; Phoon, 2008) as follows:

$$\rho(\tau) = \exp\left\{-\frac{2\tau}{l}\right\} \tag{2.21}$$

where $\tau = z\text{-}z'$ is the distance between data points (element size in one dimension) and l is an autocorrelation length describing whether the spatial soil properties show a strong

or weak relationship. A large autocorrelation length implies a smoothly varying field while a small correlation length indicates a ragged field.

In practical conditions, the different element sizes within a problem can be generates with complex geometry. Therefore, the variance reduction factor is used to compute the locally averaged statistics applied to data points (or elements) which can be expressed as follow:

$$\gamma(T) = \frac{2}{T^2} \int_0^T (T - \tau)\rho(\tau)d\tau \tag{2.22}$$

where T is the length of the domain (or elements). Figure 2.4 illustrates the Markov correlation function and variance reduction function for the correlation length $l = 1.0$.
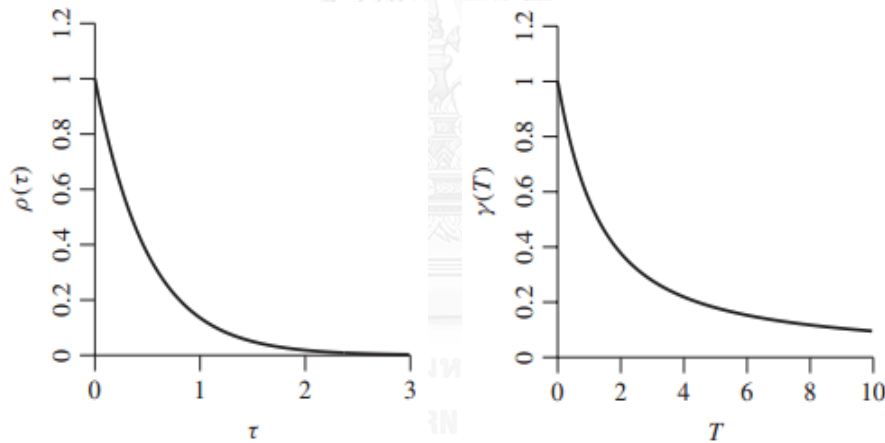
Figure 2.4. Markov correlation function and variance function

For the higher dimension (of two dimensions), the Markov correlation function and variance reduction are defined by equation (2.23) and (2.24), respectively, as shown in Figure 2.5.

$$\rho(\tau_x, \tau_y) = \exp\left\{-\frac{2\tau_x}{l_x}\right\}\exp\left\{-\frac{2\tau_y}{l_y}\right\} \tag{2.23}$$

$$\gamma(T_x, T_x) = \frac{4}{T_x^2 T_y^2} \int_0^{T_x}\int_0^{T_y} (T_x - x)(T_y - y)\rho(\tau_x, \tau_x)dxdy \tag{2.24}$$
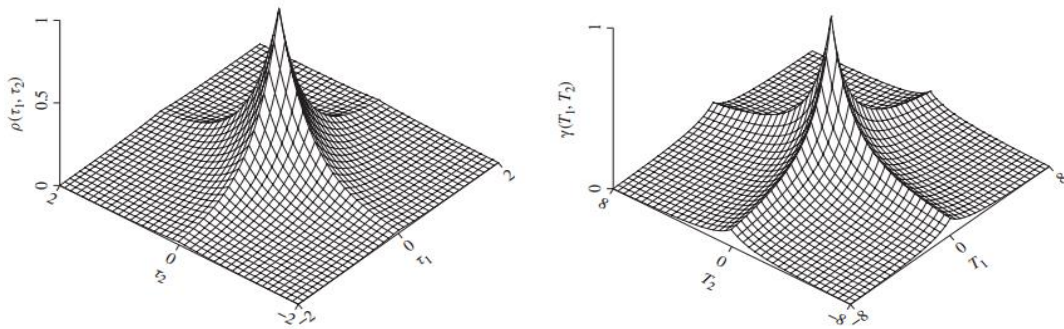
Figure 2.5. Two dimension correlation function and covariance function

(autocorrelation length $l_1 = l_2 = 1.0$)

As mentioned above, the spatial variability of the parametric studies is becoming increasingly common for generation of random fields. This leads to the recognition that probabilistic analysis of complex geotechnical engineering is no longer sufficient based solely on the mean value and covariance coefficient. Uncertain and variable parametric studies must be incorporated with the correlation length (equation (2.21) and (2.23)) to calculate failure probabilities associated with the typical performance function. Figure 2.6 (a) and (b) show a one and two dimensional random field model for a typical autocorrelation length, respectively. Nowadays, many different random field models are available to simulate spatial variability of parametric studies of which the following are perhaps the most common: 1) Moving-average (MA) method, 2) Covariance matrix decomposition, 3) Discrete Fourier transform (DFT) method, 4) Fast Fourier transform (FFT) method, 4) Turning-bands method (TBM) and 6) Local average subdivision (LAS) method. The detail of these methods can be seen in the publication of Fenton and Griffiths (2008).
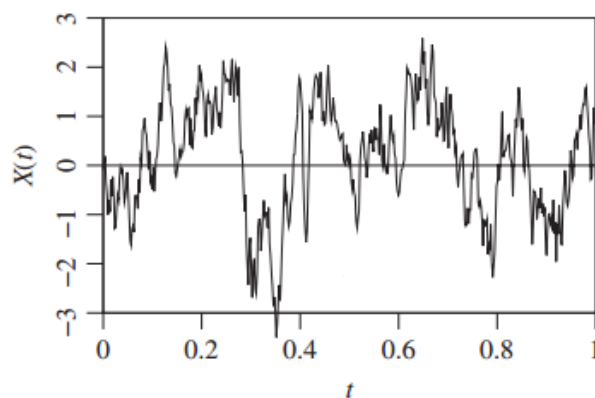
a) One dimensional random field
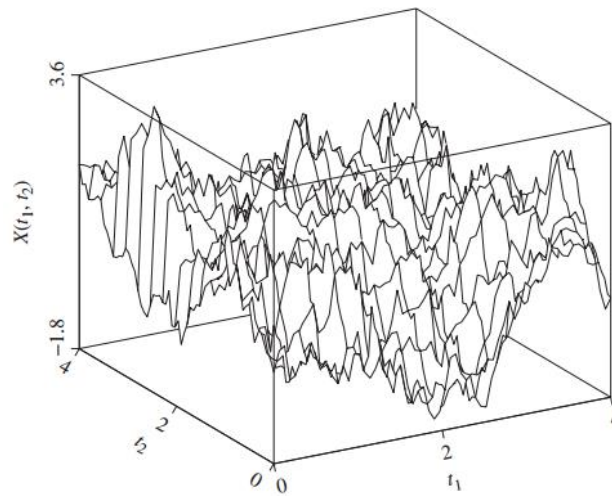
b) Two dimensional random field

Figure 2.6. Typical random field generation

2.4.3. Transformation approach

In the field of geotechnical engineering, parametric studies usually have positive values; thus, the random variables of parametric studies are assumed to be statistical characteristics by a lognormal distribution (Fenton and Griffiths, 2008) defined by the mean μ_x and standard deviation σ_x. Because the Gaussian distribution (the normal distribution) is often used to generate random variables for reasons of convenience and lack of available data, the standard deviation and mean of the underlying the normal distribution of *lnX* are given by:

$$\sigma_{\ln X} = \sqrt{(1 + \text{cov}^2)} \tag{2.25}$$

$$\mu_{\ln X} = ln\mu_X - 0.5\sigma_{\ln X}^2 \tag{2.26}$$

The corresponding probability density function can be written as:

$$f(x) = \frac{1}{x\sigma_{\ln X}\sqrt{2\pi}} exp\left[-\frac{(lnx - \mu_{\ln X})^2}{2\sigma_{\ln X}^2} \right] \tag{2.27}$$

Normal random variables can be calculated from the pseudo-random-number generator of the uniform distribution (Fenton and Griffiths, 2008). Random variables

having a lognormal distribution can be generated from the normal distribution function which was presented in equation (2.27).

2.5. Model of stability analysis on a vegetated slope

2.5.1. Background

The effects of vegetation which impact slope stability were used to determine slope stability in the 1960s but they have been considered a minor effect and are ignored in slope stability analysis at present. Although the effects of vegetation had been investigated at the time, they were only well recognized by a few research pioneers (Betlahmy, 1962; Bishop and Stevens, 1964; Endo and Tsuruta, 1969). Recent studies propose the use of vegetation effects on slope stability analysis in two ways: (1) through mechanical effects using the root reinforcement and (2) hydrological effect (Barker, 1995). The mechanical effect has been studied to understand the physical interaction between vegetation and soil slope (Stockes and Mattheck, 1996; Wu et al, 1988) and benefits in considering slope stability with vegetation (Greenway et al, 2004). In contrast, hydrological effects refer to the modification of soil moisture content caused by plant evapotranspiration and rainfall infiltration. However, because of its minor contribution during heavy rainfall, evapotranspiration is ignored in this study. Detail of vegetation relating to slope stability analysis can be found in many publications. (Gray and Leiser, 1982; Coppin and Richards, 1990; Gray and Sotir, 1996b).

2.5.2. Shear strength of root-soil

The roots of tree, shrubs, grass and other plants can reinforce the soil due to their tensile strength and adhesion properties (Coppin and Richards, 1990). It is widely recognized that the tensile strength of plant roots acts to resist tensile cracking or can be converted to the shear strength of soil. The tensile strength of plant roots contribution to slope stability depends on a number of factors, including the type of soil, geomorphology, climate conditions and plant species. In addition, the calculation of the effects of small plants on soil shear strength will be carried out in some cases and the surcharge load dismissed for large plants. Although the mechanical effects comprise various aspects, the available literature has generally focused on investigating the

influence of root reinforcement on the stability of slopes so quantifying the effect of root reinforcement will be reviewed this section.

The effect of the presence of plant roots in soils can be reviewed in the work of Endo and Tsuruta, (1969); O'Loughlin, (1974) and Waldron, (1977). The primary estimation of root reinforcement is based on an estimation of the term in the Mohr-Coulomb criterion:

$$\tau = c_s' + c_r + (\sigma_n - u_w)\tan\varphi' \tag{2.28}$$

where c_s' is the effect of cohesion of the soil, c_r is the apparent cohesion provided by roots, σ_n is the normal stress due to the weight of the soil and water of sliding mass, u_w is the soil pore water pressure, and ϕ' is the effective internal friction angle of soil.

The contributions of root reinforcement for soil shear strength have been calculated by several authors, including in-situ direct shear tests on a soil block with plant roots (Wu et al., 1988; Wu and Watson, 1998; Abernethy and Rutherfurd, 2001) and laboratory direct shear tests of soil with roots (Waldron, 1977; Terwilliger and Waldron, 1991).

2.5.3. Root area ratio

Root area ratio (RAR) is defined as the ratio of the total cross-sectional area that is occupied by all roots in a given cross-section of soil, A_r, to the total cross-sectional area of the soil being considered, A. The RAR can be determined using an equation suggested by Coppin and Richards (1990) as follow:

$$RAR = \frac{A_r}{A} = \frac{\sum n_i a_i}{A} \tag{2.29}$$

where n_i is the number of roots in size class i; a_i is the mean cross-sectional area of roots in size class i.

The depth of root is significant to the variability of the RAR which depends on plant species and environmental conditions (Greenway, 1987). Most grass roots are located within the upper 50 mm of soil (Coppin and Richards, 1990). For trees and

shrubs, root depth is specified in the range of 1.0 to 3.0 m. Normally, the depth of roots is constrained by bedrock at relatively shallow depths (less than 2 m) in many slopes (Schmid et al., 2001).

2.5.4. Root tensile strength

The tensile strength of roots can be measured using a tensile test in the laboratory or in-situ and has been reported by many researchers. The root tensile strength depends on many factors such as vegetation species, environmental conditions, and root diameter as established by previously cite authors. Table 2.2 shows the root tensile strength of some different species of plant provided by Coppin and Richards (1990). It is clear that the root tensile strength ranges widely for various plants. In addition, the root tensile strength shows significant variability with root diameter. Most studies have recognized that there is a decrease in root tensile strength with increasing diameter (Wu et al., 1979; Simson and Collison 2002, Ji et al., 2012). Figure 2.7 shows the relationship between the root tensile strength and root diameter in Loess Plateau, China.

Table 2.2. Root tensile strength (Coppin and Richards, 1990)

Species	Tensile strength (MPa)
Elymus (Agroppyron) repens (Cough grass)	7.2 - 25.3
Campanula trachelium (Bellflower)	0.0 - 3.7
Convolvulus arvenis (Bindweed)	4.8 - 21.0
Plantago lanceolate (Plantain)	4.0 - 7.8
Taraxacum officianal (Dandelion)	0.0 - 4.4
Trifolium pratense (Red Clover)	10.9 - 18.5
Medicago sativa (Alfalfa)	25.4 - 86.5
Populus nigra (Black Poplar)	5.0 - 12.0
Populus euramericana (Hybird Poplar)	32.0 - 46.0
Pseudotsuga menziesii (Douglas Fir)	19.0 - 61.0
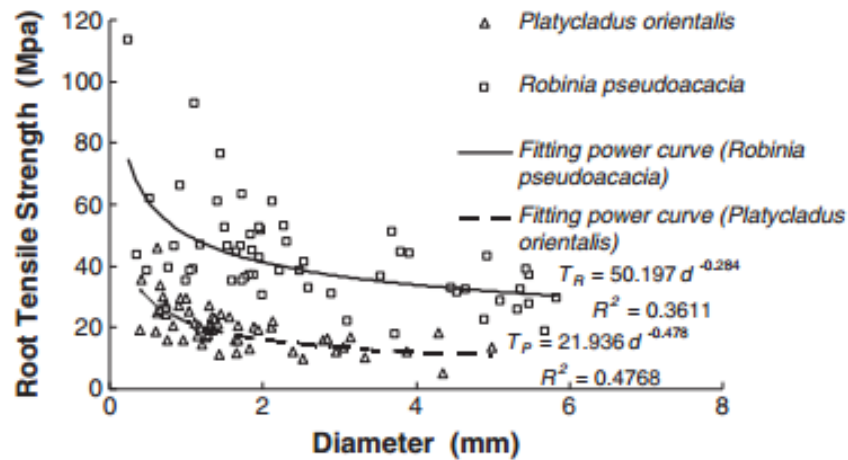
Figure 2.7. Relationship between root tensile strength and root diameters

2.5.5. Root cohesion

Following the root reinforcement models of Wu (1976), Gray and Ohashi (1983), roots are assumed to have elastic behavior, and initially perpendicular to the shear zone, the root cohesion can be defined as:

$$c_r = t_r (\cos \delta \tan \varphi' + \sin \delta) \tag{2.30}$$

where δ is the angle of deformed roots with regard to shear surface and t_r is the average mobilized tensile strength of roots per unit area of soil. The equation (2.30) is modified to determine the root cohesion from the tensile strength of an individual root T_{ri} and the root area ratio $\left(\dfrac{A_{ri}}{A_s}\right)$ of root cross-sectional area (A_{ri}) to soil cross-sectional area (A_s), where n is the number of roots in area A_s. Root cohesion can be rewritten as (Wu et al, 1979):

$$c_r = 1.2 \sum_{i=1}^{n} T_{ri} \left(\frac{A_{ri}}{A_s}\right) \tag{2.31}$$

In addition, root cohesion can be measured by a field test or a laboratory direct shear test (Eab et al., 2015) and back analysis on failed slopes. In the literature, many investigators have published that root cohesion values had different ranges due to the effect of various vegetation species growing in different environments. Table 2.3

summarizes typical values for root cohesion which vary from 1.0 to 94.3 kPa depending on type of vegetation and environments. Normally, values of root cohesion fall within the range of 1.0 - 20.0 kPa.

Table 2.3. Typical value for root cohesions, c_r.

Species	c_r (kPa)	Investigator
Alder (Japan)	2.0 - 12.0	Endo and Tsuruta, 1969
Hemlock, spruce (Alaska, USA)	3.4 - 4.4	Swanston, 1970
Conifers (British Columbia, Canada)	1.0 - 3.0	O'Loughlin, 1974
Conifer (Oregon, USA)	3.0 - 17.5	Burroughs and Thomas, 1977
Ponderosa pine, Douglas-fir (Idaho, USA)	2.8 - 6.2	Gray and Megahan, 1981
54-month-old yellow pine (Laboratory)	3.7 - 6.4	Waldron et al., 1983
Sphagnum moss (Alaska, USA)	3.5 - 7.0	Wu, 1984a
Hemlock, sitka pruce (Alaska, USA)	5.6 - 12.6	Wu, 1984b
Japanese cedar (Japan)	1.0 - 5.0	Abe and Iwamoto, 1986
Grass, sedges, shrubs, sword fem (USA)	1.6 - 2.1	Buchanan and Savigny, 1990
Natural forest-conifers (USA)	25.6 - 94.3	Schmidt et al., 2001
Industrial forest-hardwood (USA)	6.8 - 23.2	Schmidt et al., 2001
Vetiver grass (Thailand)	6.0 - 6.8	Eab et al., 2015

2.5.6. Spatial variability of root cohesion

Root cohesion is also characterized by spatial variability due to non-uniformity of the species, size, and spacing of tress on a slope. Recently, Abernethy and Rutherfurd (2001) conducted tests on two Australian riparian species which varied both vertical and horizontal dimensions. They calculated root cohesion based on the measured values of the root area ratio and root tensile strength using the perpendicular root reinforcement model. A non-linear regression was applied to estimate root cohesion which was the exponential function of distance from the tree trunk (d_h) and the depth below the soil surface (d_v).

For the river red gum:

$$c_r = e^{4.920-0.099d_h-1.333d_v} \quad r^2 = 0.70 \tag{2.32}$$

For the swamp paperbark:

$$c_r = e^{4.769-0.540d_h-1.891d_v} \quad r^2 = 0.63 \tag{2.33}$$

Schmidt et al. (2001) also conducted root cohesion calculations of some species of vegetation at the Oregon Coast Range, USA. The results show that the root cohesion values ranged from 6.8 to 23.2 kPa in industrial forests with significant deciduous vegetation and from 25.6 to 94.3 in natural forest dominated by coniferous vegetation. In their study areas, landslides tended to occur due to a reduction in root strength.

According to previous studies, slope stability analysis, which has considered the effect of various types of vegetation has ignored the spatial variability of root cohesion (Wu et al., 1979; Greenway, 1987, Lin et al., 2010; Chirico et al., 2013; Wu, 2013; Tiwari et al., 2013; Leung et al., 2015) though it was well recognized and verified by recent field measured data. In this research, random fields of root cohesion are generated using mean values, an assumption of covariance and autocorrelation length. Probabilistic analysis is then performed with generated random fields of root cohesion. The results indicated that the spatial variability of root cohesion has significant effects on slope failure.

2.5.7. Shallow failure on vegetated slopes

Vegetated slope failure is usually known as shallow translational or planar failure overlying a bedrock where a thin soil layer is less than 2.0 m thick and the length-to-depth ratio is very high. Therefore, infinite slope analysis is commonly adopted for slope stability analysis in this situation (Lu and Godt, 2008; Ray et al., 2010; Li et al., 2013). The factor of safety (FS) is defined as the ratio of the available shear strength to the shear stress expected along the failure surface. In the case of a shallow landslide, the FS can be estimated by a modification of the original equation (Wu et al., 1979) if calculation of pore air pressure in equation (2.28) is almost equal to atmospheric pressure, $u_a = 0$ as the flowing function:

$$FS = \frac{c' + c_r + \left[(W + S_w) \cos^2 \beta - u_w l \right] \tan \phi'}{(W + S) \sin \beta + D}$$

(2.34)

where: c' is the effective soil cohesion, c_r is the root cohesion, W is the total weight of the slices, S_w is the surcharge due to weight of vegetation, β is the slope angle, u_w is the pore water pressure, l is the length of slices; ϕ' is the effective friction angle of soil, and D is the wind loading (Figure 2.8). However, in this study where a vetiver grass of vegetation is focused on for slope stability analysis, the contribution of the acting force may not be so important and can be ignored in consideration of attributed vegetation.
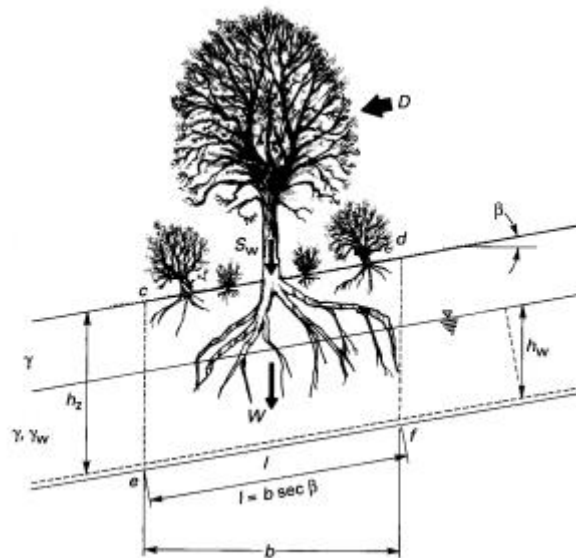
Figure 2.8. Model of a vegetated slope considering the influences of root reinforcement and acting forces

2.5.8. Deep-seated failures on a vegetated slope

Deep-seated failures usually occur in humid tropical environments where the soil layers are rather deep reaching up to 30 m depth (Collison and Anderson, 1996). Therefore, roots of plant cannot occupy the entire soil layer and the failure mechanism may be circular, or non-circular, or rotational rather than in the case of shallow failure where critical surfaces may pass beneath the root zone. To study the influences of vegetation on deep-seated slope failures, Greenwood (2006) developed a spreadsheet-based program using the traditional limit equilibrium method modified to consider the contribution of root cohesion, surcharge, and wind loading while hydrological effects

were only calculated according to changes in pore water pressure. Several researchers the University of Bristol, UK also developed a stability model in order to study the effects of rainfall infiltration on vegetated slope stability analysis. This model simulated the flow system using a forward explicit finite difference scheme with Darcy's law in a saturated condition. For the unsaturated condition, water flow is computed using Richards' equation. Evapotranspiration and root water uptake were modelled using the Penman-Monteith equation and an increase in apparent soil using the root reinforcement model of Wu et al. (1979).

2.6. Unsaturated seepage analysis

2.6.1. The continuity equation of unsaturated seepage analysis

Water flow through unsaturated soil is governed by the same physical law, Darcy's law, as fluid flow through saturated soils. The major difference between water flow in saturated and unsaturated soil is that the coefficient of permeability is assumed to be a constant in saturated soil while it is a function of matrix suction in unsaturated soils. However, the partial differential equation of flow is similar in the two cases. Richards (1931) developed Darcy's law in order to simulate the sum of the rates of change flows plus an external applied as equal to the rate of change of the volumetric moisture content with respect to time which can be expressed using a continuity equation as follow:

$$\frac{\partial}{\partial x}\left[k_x \frac{\partial h}{\partial x}\right] + \frac{\partial}{\partial y}\left[k_y \frac{\partial h}{\partial y}\right] + \frac{\partial}{\partial z}\left[k_z \frac{\partial h}{\partial z}\right] + Q = \frac{\partial \theta}{\partial t} \tag{2.35}$$

where k_x, k_y, k_z, is the permeability function (coefficient permeability) in x, y, z directions, respectively, h is the total hydraulic head, θ is the volumetric moisture content, t is time, and Q is the applied boundary flux calculated from the difference between rainfall and runoff. It should be noted that the amount of water stored within the soil depends on the soil suction and volumetric moisture content, as shown in Figure 2.9 for typical soil. In addition, the hydraulic conductivity is also highly non-linear depending on pore water pressure in unsaturated soil (Figure 2.10). The volumetric moisture content and hydraulic conductivity are associated with soil type, in the

literature, many models have adopted in unsaturated soil framework as mentioned in the following section.
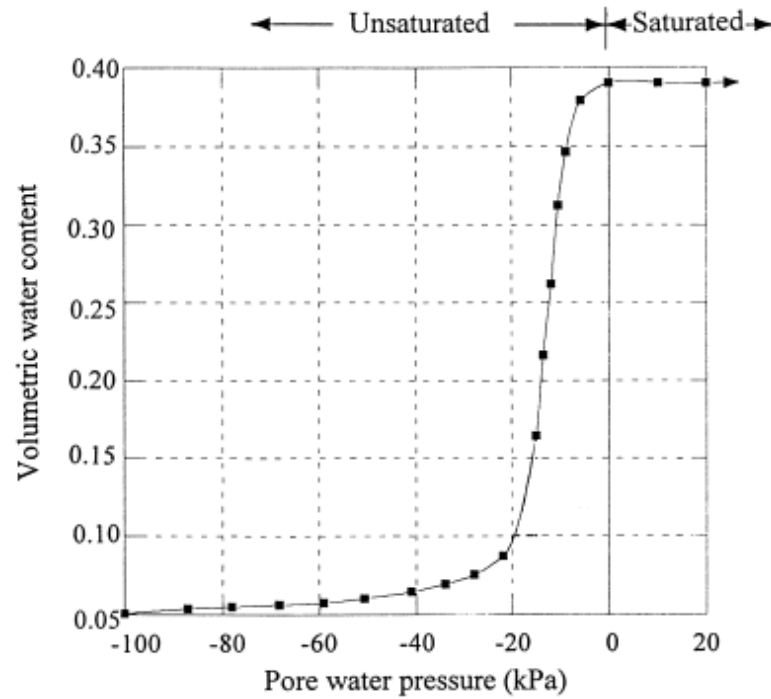
Figure 2.9. Volumetric moisture content versus pore water pressure
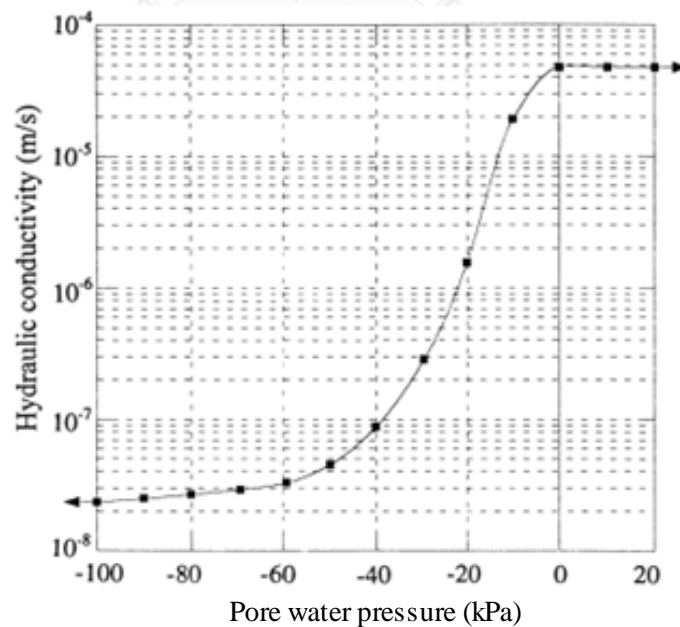
Figure 2.10. Hydraulic conductivity versus pore water pressure

2.6.2. Soil water characteristic curves (SWCC)

As mentioned in section 2.6.1, the relationship between suction (negative pore water pressure) and the amount of water stored within the soil, known as SWCC, is important for unsaturated seepage analysis. Nowadays, a large number of closed-form solutions and empirical equations have been proposed to best fit laboratory data or field data for SWCCs, as presented in Table 2.4.

Table 2.4. Empirical equation used to best fit SWCC data

Reference	Equation	Description
Gardner (1958b)	$$\Theta_d = \frac{1}{1 + a_g \psi^{n_g}}$$ where $$\Theta_d = \frac{w(\psi)}{w_s}$$	a_g = fitting parameter which is a function of air-entry value of the soil n_g = fitting parameter which is a function of rate of water extraction from soil once air-entry value of soil has been exceeded
Brooks and Corey (1964)	$w(\psi) = w_s$ or $\Theta_n = 1$ for $\psi \leq \psi_{aev}$ $$\Theta_n = \left[\frac{\psi}{\psi_{aev}}\right]^{-\lambda_{bc}} \quad \psi > \psi_{aev}$$ where $$\Theta_n = \frac{w(\psi) - w_r}{w_s - w_r}$$	ψ_{aev}= air-entry value of soil λ_{bc} = pore size distribution index w_r = residual water content located through trial-and-error process that yields straight line on semi log plot of degree of saturation versus suction
Brutsaert (1967)	$$\Theta_n = \frac{1}{1 + [\psi/a_b]^{n_b}}$$ where $$\Theta_n = \frac{w(\psi) - w_r}{w_s - w_r}$$	a_b = fitting parameter which is a function of air-entry value of soil n_b = fitting parameter which is a function of rate of water extraction from soil once air-entry value has been exceeded
Laliberte (1969)	$$\Theta_n = \frac{1}{2}\text{erfc}\left[a_l - \frac{b_l}{c_l + (\psi/\psi_{aev})}\right]$$ where $$\Theta_n = \frac{w(\psi) - w_r}{w_s - w_r}$$	a_l, b_l, c_l = parameters assumed to be unique functions of pore-size distribution index λ
Campbell (1974)	$w = w_s, \psi < \psi_{aev}$ $$w = w_s \left[\frac{\psi}{\psi_{aev}}\right]^{-1/b_c}, \psi \geq \psi_{aev}$$	ψ_{aev} = air-entry value of soil b_c = fitting parameter
van Genuchten (1980)	$$\Theta_n = \frac{1}{[1 + (a_{vg}\psi)^{n_{vg}}]^{m_{vg}}}$$ where $$\Theta_n = \frac{w(\psi) - w_r}{w_s - w_r}$$	a_{vg}, a_{vm}, a_{vb} = fitting parameters primarily related to inverse of air-entry value (units equal to 1/kPa) n_{vg}, n_{vm}, n_{vb} = fitting parameters primarily related to rate of water extraction from soil once air-entry value has been exceeded m_{vg}, m_{vm}, m_{vb} = fitting parameters that are primarily related to residual water content conditions
van Genuchten (1980)–Mualem (1976)	$$\Theta_n = \frac{1}{[1 + (a_{vm}\psi)^{n_{vm}}]^{m_{vm}}}$$ where $$m_{vm} = 1 - \frac{1}{n_{vm}}$$	

Reference	Equation	Description
van Genuchten (1980)– Burdine (1953)	$$\Theta_n = \frac{1}{[1+(a_{vb}\psi)^{n_{vb}}]^{m_{vb}}}$$ where $$m_{vb} = 1 - \frac{2}{n_{vb}}$$	
McKee and Bumb (1984) (Boltzmann distribution)	$$\Theta_n = \exp\left[\frac{a_{m1}-\psi}{n_{m1}}\right]$$ where $$\Theta_n = \frac{w(\psi)-w_r}{w_s-w_r}$$	a_{m1} = curve-fitting parameter n_{m1} = curve-fitting parameter
McKee and Bumb (1987) (Fermi distribution)	$$\Theta_n = \frac{1}{1+\exp[(\psi-a_{m2})/n_{m2}]}$$ where $$\Theta_n = \frac{w(\psi)-w_r}{w_s-w_r}$$	a_{m2} = curve-fitting parameter n_{m2} = curve-fitting parameter
Fredlund and Xing (1994)	$$w(\psi) = C(\psi)\frac{w_s}{\left[\ln\left[e+(\psi/a_f)^{n_f}\right]\right]^{m_f}}$$ where $$C(\psi) = 1 - \frac{\ln(1+\psi/\psi_r)}{\ln[1+(10^6/\psi_r)]}$$ $$\Theta_d = \frac{w(\psi)}{w_s}$$	a_f = fitting parameter which is primarily a function of air-entry value of soil n_f = fitting parameter which is primarily a function of rate of water extraction from soil once air-entry value has been exceeded m_f = fitting parameter which is primarily a function of residual water content $C(\psi)$ = correction factor which is primarily a function of suction corresponding to residual water content.
Pereira and Fredlund (2000)	$$w(\psi) = w_r + \frac{w_s-w_r}{\left[1+\left[\psi/a_p\right]^{n_p}\right]^{m_p}}$$	a_p = fitting parameter which is primarily a function of air-entry value of soil n_p = fitting parameter which is primarily a function of rate of water extraction from soil, once air-entry value has been exceeded m_p = fitting parameter which is primarily a function of residual water content
Pham and Fredlund (2005)	$$\begin{cases} w_1(\psi) = w_s - S_1\log(\psi) & 1 \leq \psi < \psi_{aev} \\ w_2(\psi) = w_{aev} - S_2\log\left(\dfrac{\psi}{\psi_{aev}}\right) & \psi_{aev} \leq \psi < \psi_r \\ w_3(\psi) = S_3\log\left(\dfrac{10^6}{\psi}\right) & \psi_r \leq \psi < 10^6 \text{ kPa} \end{cases}$$	S_1, S_2, S_3 = slope of straight line portions of SWCC within each of three zones w_s = water content at 1 kPa w_{aev} = water content at air-entry value w_1, w_2, w_3 = water content in line segments 1, 2, and 3, respectively.

The equation in Table 2.4 can be included in two-parameter SWCC equations and three-parameter SWCC equations. Each of these equations can be best fit to laboratory or field data using a non-linear regression analysis in order to find curve-fitting parameters as input hydraulic parameters in unsaturated seepage analysis.

2.6.3. Numerical solutions for multi-dimensional problem

The nonlinear partial differential equation (2.35) has no general analytical solution and hence the use of numerical approximation is one of the best solutions. Numerical models of unsaturated flow have also been combined with slope stability models to examine a wide variety of geotechnical engineering problem. Three approaches have been used to solve the Richard's equation: 1) Finite Different Method (Zarba et al., 1990); 2) Finite Element Method (Panday et al., 1993; Forsyth et al., 1995); 3) Finite Volume Method (Takeuchi et al., 2010; Zambra et al., 2012). Table 2.5 lists several of the freely available and commercial models for simulating variable unsaturated flow.

Table 2.5. Numerical software for simulation of unsaturated flow.

Model	Dimensions	Licensing	Description	Reference
VS2DI	2	Freely available	Finite difference solution of the Richard's equation, solute and heat transport, graphical user interface	Hsieh et al., 1999; Healy, 2008
HYDRUS 1-D	1	Freely available	Finite element solution of the Richard's equation, graphical user interface, inverse modeling of material properties from observation	Simunek et al., 2005;
HYDRUS 2D/3D	3	Commercial	3-D finite element solution to the Richard's equation, hysteresis of soil hydraulic properties, non-linear solute transport	Simunek et al., 1999, 2005;
TOUGH2	3	Freely available	3-D integrated finite-difference solution to the Richards equation, hysteresis of soil hydraulic properties, non-linear hear transfer	Pruess et al., 2011
Geo studio/ SEEP/W	2	Commercial	Finite element method to solve Richards's equation for unsaturated-saturated condition.	Geo Studio 2007

CHAPTER 3: RESEARCH METHODOLOGY

3.1. Introduction

This chapter discusses the implementation of the finite element method for seepage analysis during heavy rainfall and the determination of the factor of safety using the limit equilibrium method. Probabilistic analysis was approximated considering the effect of spatial variability of soil shear strength parameters. The available software was modified in order to analyze the effect of spatial variability of root cohesion on vegetated slope failure. The procedure will be carried out in a subsequent chapter.

3.2. Definition of spatial variability of parametric studies

In this study, the effective soil cohesion, friction angle of soil, and root cohesion are defined as random variables at a given point. The mean values of these random variables are calculated form both laboratory and field test while their cov is taken from previous researchers with the exception of root cohesion. The assumption of cov of root cohesion is set because no data has been reported. In order to describe the spatial correlation between two random variables, autocorrelation lengths are varied following the typical case study, as shown in Table 3.1.

Table 3.1. Spatial variability characteristic of parametric studies

Parametric studies	Mean value	cov	Autocorrelation length
Effective cohesion (c') Effective friction angle (ϕ') Root cohesion (c_r)	Laboratory and field test	Previous researchers Assumptions	Varied

3.3. Finite element method for seepage analysis

For seepage analysis in an unsaturated soil layer, Darcy's law originally derived for saturated soil, was modified to accommodate the flow of water through unsaturated soil (Richards, 1931). The only difference made is that under conditions of unsaturated flow, hydraulic conductivity is no longer a constant. There are some empirical and semi-empirical functions which have been proposed to present hydraulic conductivity.

In this study, nonlinear functions of the volumetric moisture content and the coefficient of permeability of the unsaturated soil were adopted based on the Mualem-van Genuchten model (van Genuchten, 1980) as:

$$S_e = \frac{\theta - \theta_r}{\theta_s - \theta_r} = \frac{1}{\left[1 + (\alpha h)^n\right]^m} \tag{3.1}$$

where $m = 1 - \dfrac{1}{n}$, n > 1 are dimensionless parameters, and

$$k_z = k_s S_e^{1/2} \left[\left(1 - S_e^{1/m}\right)^m\right]^2 \tag{3.2}$$

in which S_e is the effective water saturation, θ_r is the residual volumetric moisture content, θ_s is the saturated volumetric moisture content, k_s is the saturated permeability (m/hr), and α is the fitting parameter (1/m).

The numerical codes were developed on the basis of the theory of unsaturated flow. In this study, the finite element method was applied using the SEEP/W module of Geo-Studio 2007 to solve the equation (2.35) in one and two dimensional directions. To obtain the result, the time step increment and element size should be defined in the advantage (Pan et al., 1996; Van Dam and Feddes, 2000; Caviedes-Voullième et al., 2013).

3.4. Determination of factor of safety

Factor of safety (FS) is defined as the ratio of the available shear strength to the shear stress calculated along the failure surface. Normally, traditional limit equilibrium is used to determine the factor of safety of a slope under transient infiltration condition (Lu and Godt, 2013). Therefore, a method of slices was adopted to calculate the factor of safety along the potential failure surface and to search for a critical surface, the factor of safety can be expressed as:

$$FS = \frac{\sum_{i}^{n} \tau_f l_i}{\sum_{i}^{n} W_i \sin\beta_i} \tag{3.3}$$

where n is the total number of slices, τ_f is the shear strength of soil which was defined as equation (2.2), i is the slice index, l_i is the length of each slice, W_i is the weight of each slice per unit base area; β_i is the base inclination of the slice. The factor of safety is then calculated with the apparent seepage analysis.

3.5. Random field generation

Spatial variability of a random field of standard normal distribution (Gaussian random field) can be simulated using the following spectral approach:

$$X(z_i) = \sum_{i=1}^{n} R_i \left[A_i \sin(2\pi f_i z_i) + B_i \cos(2\pi f_i z_i) \right] \tag{3.4}$$

in which $R_i = \sqrt{G(f_i)\tau}$ and $f_i = (2i-1)\tau/2$

where n is the number of discrete frequency, equal to the power of 2 , $G(f)$ is the one-sided spectral density function, f is the frequency interval of $G(f)$ domain, A_j and B_j are uncorrelated standard normal random variables.

Since the second-moment of a Gaussian random field (covariance function, $C(\tau)$) is the Fourier transform of the one-sided spectral density function $G(f)$ the inverse transform can be applied to find the one-sided spectral density function as follow:

$$G(f) = \frac{2}{\pi} \int_0^\infty \frac{C(\tau)}{\sigma_X^2} \cos(2\pi f \tau) d\tau \tag{3.5}$$

in which $C(\tau) = \rho(\tau)\sigma_X^2$ and $\sigma_X^2 = 1$ with the standard normal distribution. Equation (3.5) can be written in terms of the correlation function as:

$$G(f) = \frac{2}{\pi} \int_0^\infty \beta(\tau) \cos(2\pi f \tau) d\tau \tag{3.6}$$

For a random field model, the value of parametric study assigned to each element is itself a random variable which can be correlated to one another by controlling the correlation coefficient. Because the size of each element might be different within the domain, the mean value assigned for each element is affected by local averaging. For a

finite element size T, the variance reduction factor due to local averaging with numerical solution from equation (2.22) is:

$$\gamma(T) = \frac{l^2}{2T^2}\left[\frac{2T}{l} + exp\left(-\frac{2T}{l}\right) - 1\right] \tag{3.7}$$

and the spatial variability of random field of parametric study can be generated by equation:

$$\Omega(z_i) = exp\left[\mu + \sigma\gamma(T)X(z_i)\right] \tag{3.8}$$

3.6. Failure probability

The probabilistic analysis of slope failure can be formulated using a set of random variables. Let Ω denote random variables of parametric study; $f(\Omega)$ is the joint probability density function of Ω, and $FS(\Omega)$ is the factor of safety. The failure probability can be calculated by the following integral (Baecher and Christian, 2003):

$$P_f = P\left[FS(\Omega) \leq 1\right] = \int_{FS(\Omega)\leq 1} f(\Omega)d\Omega \tag{3.9}$$

A Monte Carlo simulation (MCS) is adopted to calculate the failure probability due to the variability of root cohesion as:

$$P_f \approx \frac{1}{n}\sum_{k=1}^{n} I\left[FS(\Omega^k)\right] \tag{3.10}$$

where n is the number of simulations, and $I\left[FS(\Omega^k)\right]$ is an indicator function characterizing the failure domain defined as:

$$I\left[FS(\Omega^k)\right] = \begin{cases} 1 & FS(\Omega^k) \leq 1 \\ 0 & FS(\Omega^k) > 1 \end{cases} \tag{3.11}$$

3.7. Flow chart of the methodology

The procedure of the probabilistic method considering the effect of spatial variability of parametric studies during heavy rainfall can be summarized as shown in Figure 3.1.
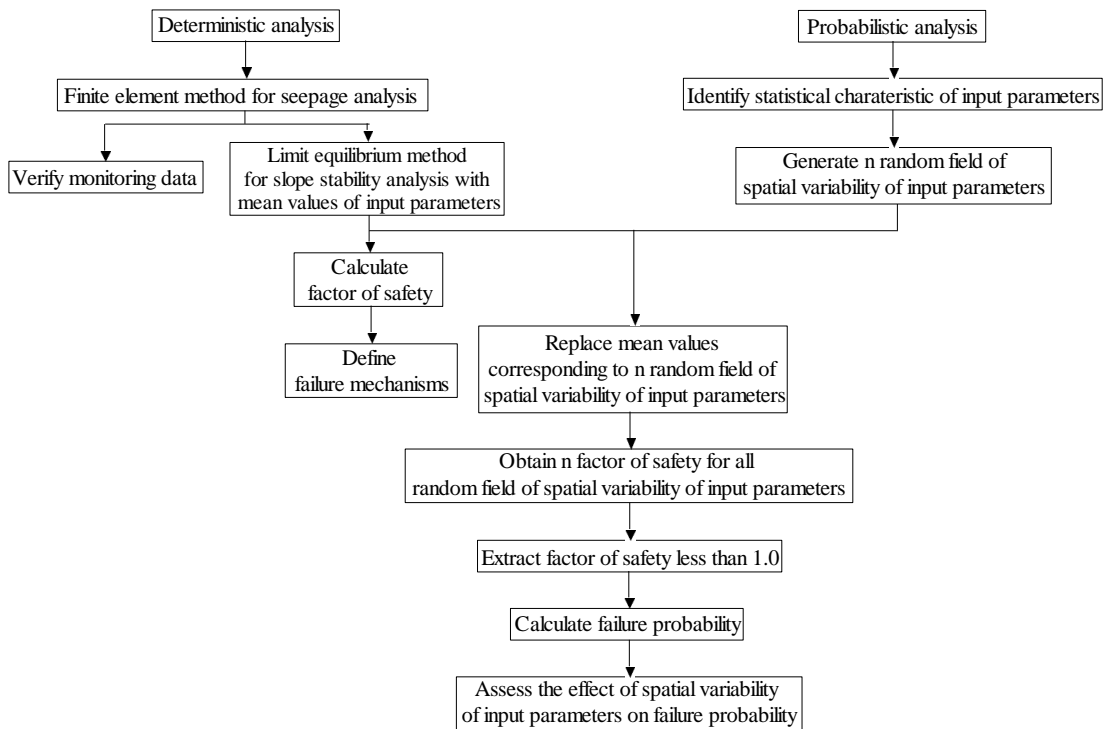
Figure 3.1. Flow chart of methodology

CHAPTER 4: THE INFLUENCE OF SPATIAL VARIABILITY IN SHEAR STRENGTH PARAMETERS ON RAINFALL INDUCED LANDSLIDE: A CASE STUDY OF SANDSTONE SLOPES IN JAPAN

4.1. Introduction

This chapter describes in detail the influence of spatial variability in shear strength parameters on rainfall induced slope failure. The study site is located in the southwest Boso Peninsula, central Japan including the three sandstone slopes: S-1, S-2, S-3 and the three mudstone slopes: M-1, M-2, and M-3, as seen in Figure 4.1.
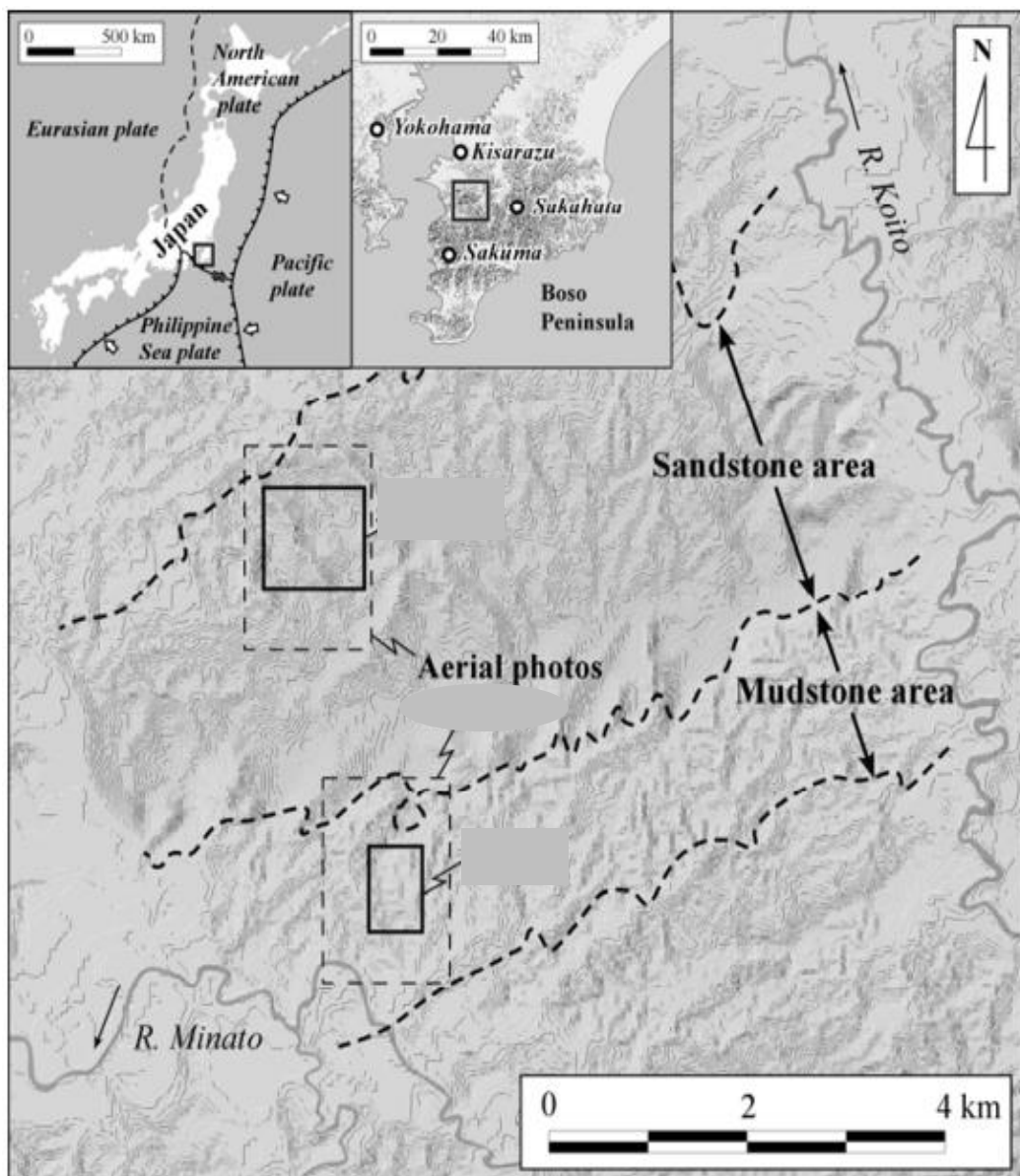
Figure 4.1. Site location.

4.2. Data collection and analysis

4.2.1. Landslide characteristics: slope geometry and soil profile

A 1989 rainstorm which caused landslides along the sandstone and mudstone slopes was recorded at four meteorological stations (Yokohama, Kisarazu, Sakuma, and Sakahata) within a 30 km radius from the study site (Figure 4.2). The sandstone slope S-1, which has an angle of $\beta = 38.4^0$, slip depth of 1.6 m, sliding area of 620 m^2 and volume of 990 m^3 was selected in this study (Matsushi et al., 2006). Figure 4.3 shows the longitudinal section and failure surface of the S-1 slope, and Table 4.1 shows landslide characteristics of slope S-1. The properties of the upper 1.5 m soil layer were evaluated from undisturbed soil core samples of 5.0 cm diameter and 5.1 cm height, which was extracted at every 10-15 cm depth intervals, as summarized in Table 4.2 (Matsushi, 2006).
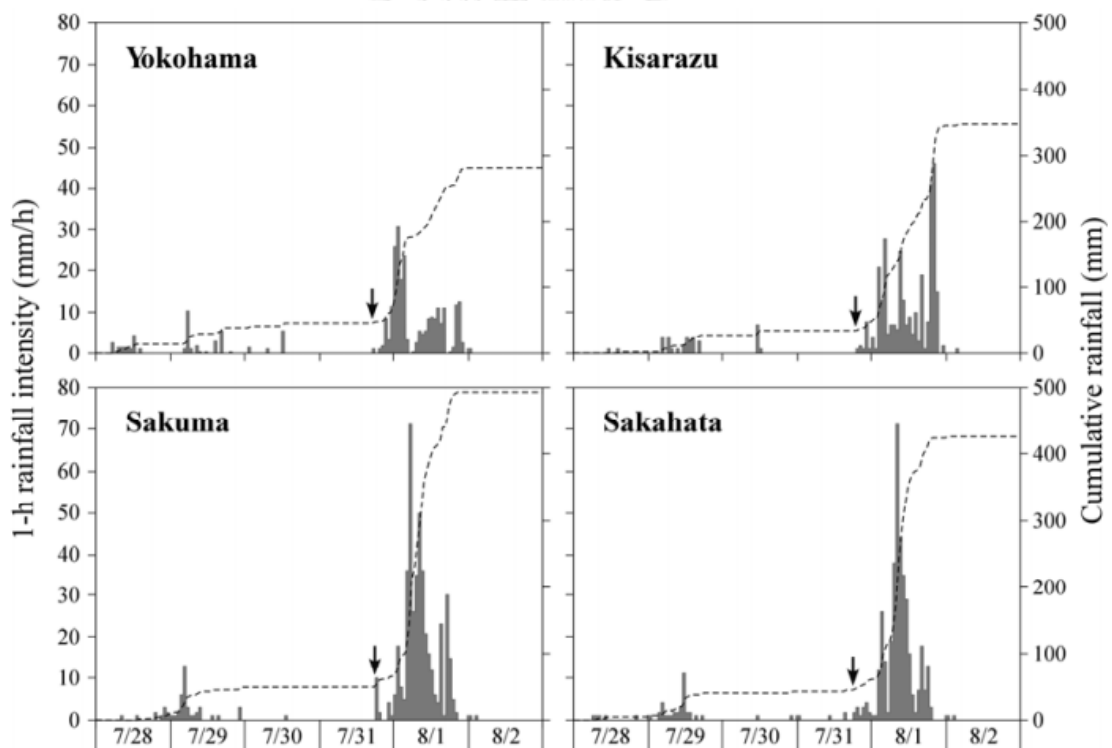
Figure 4.2. A 1989 storm at four meteorological stations (Data from Matsushi (2006)).
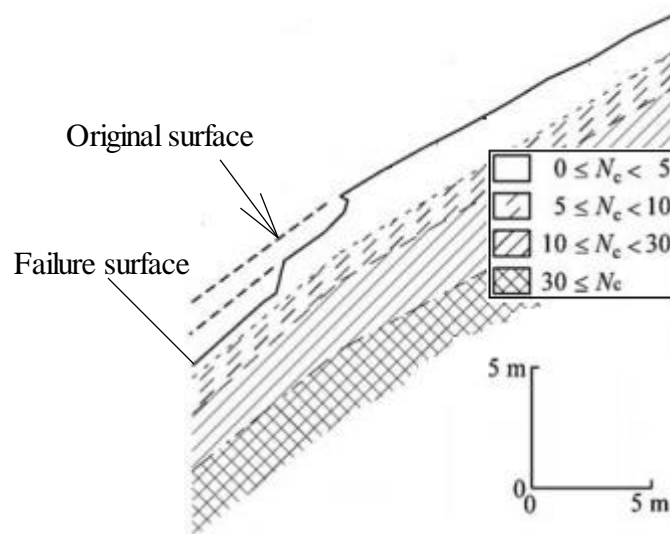
Figure 4.3. The longitudinal section and failure surface of slope S-1 (adapted from Matsushi (2006))

The soil profile of slope S-1 was classified using a dynamic cone penetration test (DCPT) value (N_c), as shown in Figure 4.4. Wakatsuki et al. (2005) classified the ground into four soil layers: $0 \leq N_c < 5$ (upper layer), $5 \leq N_c < 10$ (middle layer), $10 \leq N_c < 30$ (lower layer), and $N_c \geq 30$ (bedrock). In the classification of weathered rock by the Geological Society (1995), the upper layer and the middle layer correspond to "Grade V/VI" (completely weathered soil), the lower layer corresponds to "Grade IV" (highly weathered rock) and the bedrock corresponds to "Grade I-III" (slightly weathered rock and fresh rock). According to the Unified Soil Classification System (USCS), the upper layer can be classified as silty sand (SM) based on grain-size distribution (Table 4.2).

Table 4.1. Dimensions of landslide.

Slope	Slope angle (degrees)	Slip depth[*] (m)	Sliding area (m²)	Volume (m³)
Sandstone S-1	38.4	1.6	620	990

[*] Measured vertically from the original ground surface to the slip plane.

(records of the 1989 storm)

Table 4.2. Physical soil properties.

Depth (cm)	Dry unit weight (kN/m^3)	Porosity	Grain-size distribution (%)		
			Clay	Silt	Sand
10	9.8	0.63	3.5	14.6	81.9
30	12.1	0.54	6.2	19.5	74.2
45	12.8	0.52	-	-	-
60	13.3	0.50	3.7	8.0	88.3
75	13.7	0.48	-	-	-
90	13.7	0.48	8.4	7.9	83.6
120	12.9	0.51	7.1	6.5	86.4
150	13.3	0.50	4.7	4.3	91.0
Average	*12.7*	*0.52*	*5.6*	*10.1*	*84.3*
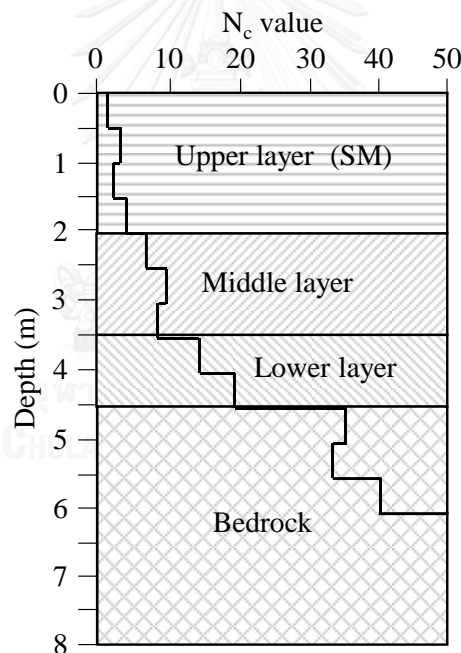
Figure 4.4. Soil profile of slope S-1

4.2.2. SWCC parameters and saturated permeability of slope S-1

The soil suction and volumetric moisture content of the upper layer were obtained from pressure plate tests. The soil water characteristic curve (SWCC) and its curve-fitting of the van Genuchten model using the SWRC-Fitting program (Seki, 2007) are presented in Figure 4.5. In this study, the types of the middle and lower layer of soil can be reasonably assumed to be the same as the top layer based on the DCPT;

therefore, the same set of SWCC parameters were used for all soil layers. The saturated permeability was determined from a constant head permeability test which was obtained from the upper soil layer down to the bedrock, as shown in Figure 4.6. Table 4.3 summarizes the fitting parameters of the soil-water characteristic curve and the average saturated permeability of all soil layers as input parameters for unsaturated seepage analysis.
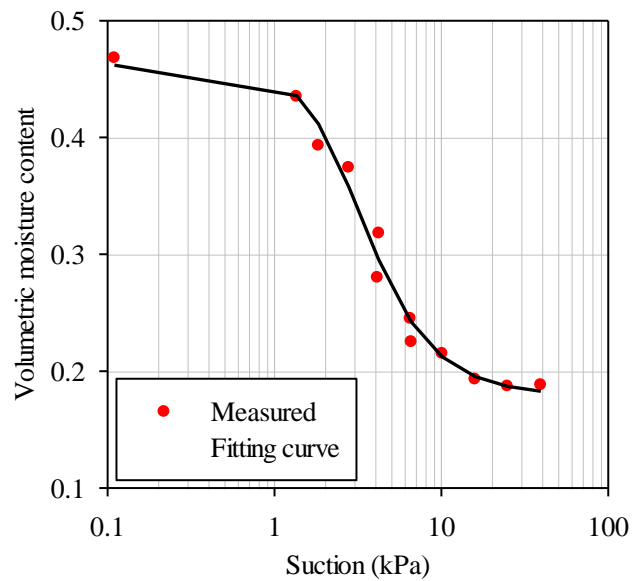
Figure 4.5. Soil water characteristic curve of upper layer
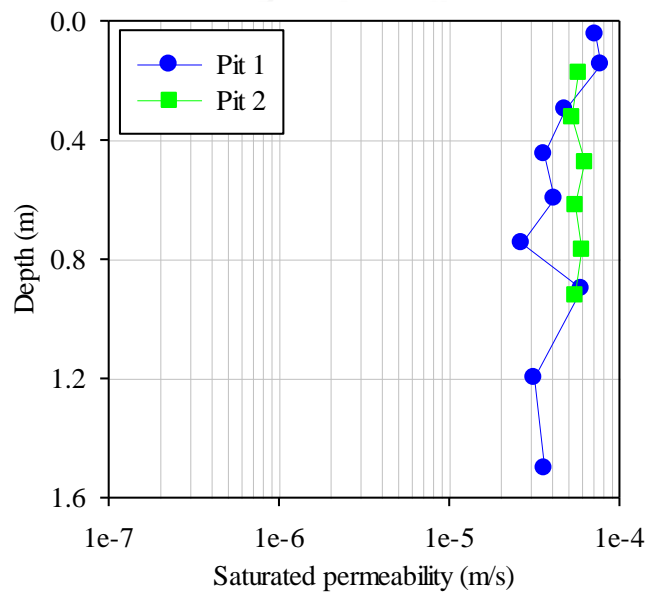
Figure 4.6. Saturated permeability varied with depth from a constant head permeability test

Table 4.3. SWCC parameters and saturated permeability.

Parameters	Value
θ_r	0.179
θ_s	0.462
α (1/m)	3.73
n	2.598
k_s (m/s)	4.28×10^{-5}

4.2.3. Soil shear strength of slope S-1

The shear strength of soils determined under four different normal stresses with various volumetric moisture contents (Matsushi et al., 2006) were used in the analysis. The best fitting curves of shear strength versus volumetric moisture content for normal stress of 10, 20, 30 and 40 kPa are presented in Figure 4.7. The apparent soil cohesion (soil cohesion in dry condition), the frictional angle, and the reduction coefficient were calculated as the input shear strength parameters for the stability analysis, as summarized in Table 4.4. It is noted that the direct shear tests were performed for the upper layer (i.e., < 2 m depth). The analysis was then focused on the upper layer.

$$\tau_f = 35.8e^{-4.81\theta} + \sigma_n tan(28.3)$$
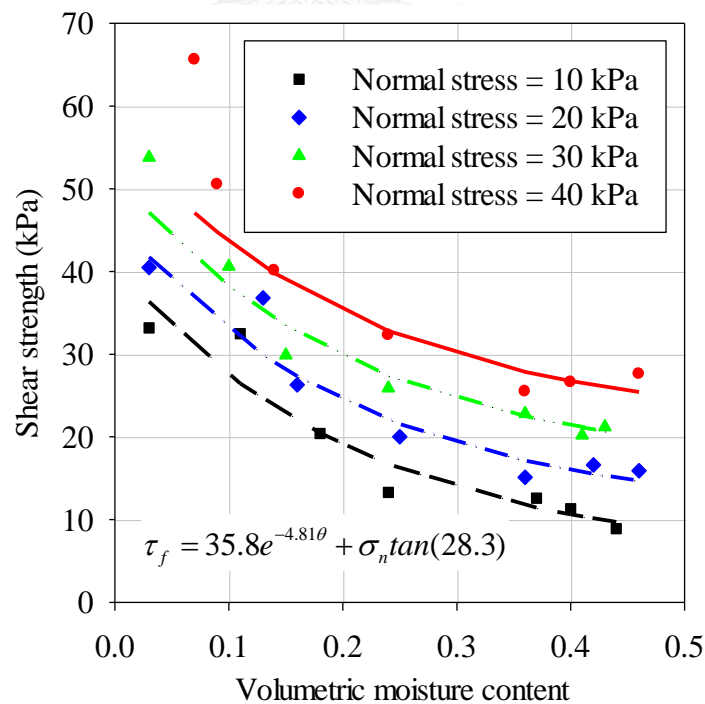
Figure 4.7. Best fitted shear strength versus volumetric moisture content curves for four normal stresses

Table 4.4. Soil shear strength parameters

Parameters	Meaning	Value
c (kPa)	Apparent soil cohesion	35.8
ϕ (^{0})	Friction angle	28.3
μ	Reduction coefficient	4.81

Remark: $C = ce^{-\mu\theta}$ is total soil cohesion under unsaturated condition

4.3. Modelling seepage analysis of the SM layer

4.3.1. Boundary and initial condition
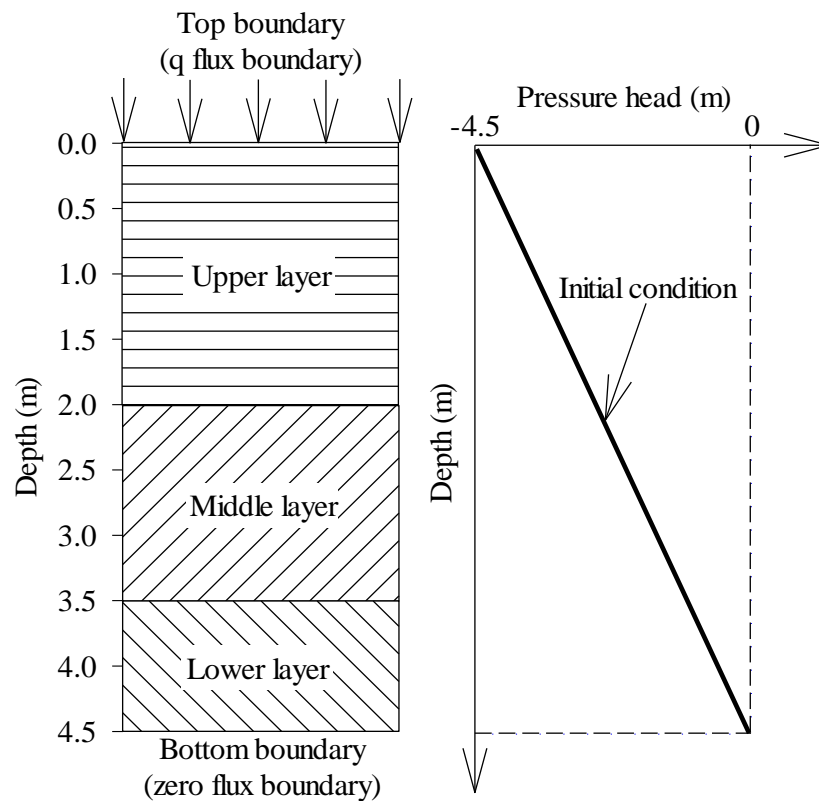
Figure 4.8. One dimension of transient seepage analysis model of S1-slope (element size, $\Delta z = 0.05$ m)

In this section, a one-dimensional transient seepage analysis was conducted to study the effect of the 1989 rainstorm causing the shallow slope failure in the Japan site. For the S-1 slope, the bedrock located at 4.5 m depth (Figure 4.4) was designated the bottom undrained boundary (zero flux boundary), while the top boundary of the model should be designated a flux boundary (q), which is equivalent to the desired

rainfall intensity. The average rainfall intensity from four recorded stations (Figure 4.2), which was equivalent to a flux of 0.032 m/hr, was defined as the top boundary condition. The linear pressure head (zero at bedrock and -4.5 m at the surface slope) was set as the initial condition. No ponding on the top surface of the soil column can be reasonably assumed due to the fact that when the rainwater exceeds the infiltration capacity of soil the excess water will drain away as surface runoff. A small time step increment of 1 second, and element size of 0.05 m were used in the analysis. A one-dimensional transient seepage analysis model of the S1-slope is presented in Figure 4.8.

4.3.2. Volumetric moisture content from the unsaturated seepage analysis
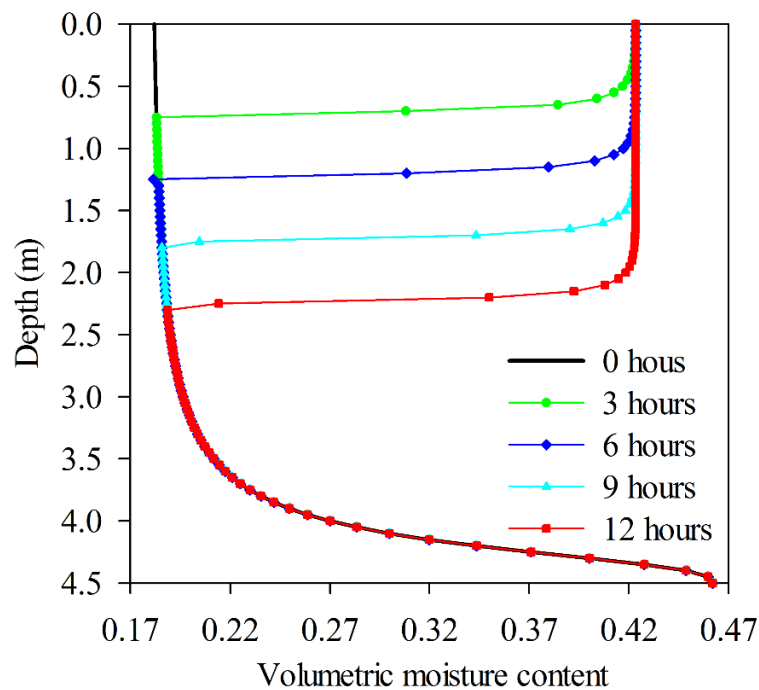
Figure 4.9. Volumetric moisture content profiles of the S-1 slope

In this section, an unsaturated seepage analysis was performed to investigate slope stability during rainfall. The resulting volumetric moisture content determined from SEEP/W was then used with the infinite slope stability model to determine the corresponding factor of safety. Figure 4.9 shows the vertical distribution of volumetric moisture content with the duration of rainfall. The results show that the volumetric moisture content of ground surface rapidly increased at the beginning of rainfall. Then, the volumetric moisture content increased with depth as rainfall infiltrated the soil. When infiltration remained constant after 12 hours, the volumetric moisture content

nearly reached saturation, and there was no generation of positive pore water pressure in the upper layer.

4.4. Stability analysis of slope S-1

4.4.1. Infinite slope stability model

As mentioned in section 4.2.1, the failure surface of slope S-1 was parallel to the original plane and the depth of failure was less than 2.0 m. This implies that S-1 slope failure is normally categorized as a shallow failure, in which the infinite slope assumption can be reasonably used to analyze the stability of slope S-1. Therefore, the infinite slope stability model was adopted in this case study, as shown in Figure 4.10. The factor of safety of the infinite slope can be expressed as:

Figure 4.10. Stability analysis of an infinite slope model

$$FS = \frac{\tau_f}{\tau_m} = \frac{\tau_f}{W sin\beta cos\beta}$$

(4.1)

where τ_f is the shear strength of soil which was defined as equation (2.2), τ_m is the shear stress at any point along the potential failure surface, W is the weight of the soil slice per unit base area, and β is the slope angle.

According to research by Fredlund et al. (2012) the shear strength of soil can be simplified as:

$$\tau_f = C + (\sigma_n - u_a)tan\phi'$$

(4.2)

where $C = c' + (u_a - u_w)tan\phi^b$ is the total cohesion under unsaturated soil condition.

The shear strength parameters from the direct shear tests conducted by Matsushi et al. (2006) were adopted in this study. During the test, a single-staged direct shear was performed under different normal stresses. The moisture conditions of soil specimens varied from an oven-dried condition to a capillary saturated condition. The results indicate that the total cohesion can be expressed using an exponential decay function of the apparent soil cohesion at dry condition (c), reduction coefficient (μ), and volumetric moisture content (θ) as:

$$C = ce^{-\mu\theta}$$

(4.3)

However, observations found that the frictional angle is rather constant, so in this study the friction angle is assumed to be constant (i.e., $\phi = \phi'$).

The unit weight of the soil slice increases with the moisture content from rainfall infiltration. The weight of a vertical soil column per unit cross-sectional area (W) from the slope surface to the potential failure surface can be expressed as:

$$W = \sum_{i=1}^{m} (\gamma_d + \theta_i\gamma_w)\Delta z$$

(4.4)

where m is the total number of elements, Δz is the thickness of the soil, γ_d is the dry unit weight of soil, and θ_i is the volumetric moisture content of each soil element.

In addition, the unstable slope is still affected by the increase in pore water pressure (Figure 4.10) causing decrease in effective stress. If $u_a = 0$ at atmospheric pressure, the safety factor of the slope can be expressed as:

$$FS = \frac{ce^{-\mu\theta}}{\sum\limits_{i=1}^{m}(\gamma_d + \theta_i\gamma_w)\Delta z \sin\beta\cos\beta} + \frac{\tan\phi}{\tan\beta} - \frac{\max(u_w,0)\tan\phi}{\sum\limits_{i=1}^{m}(\gamma_d + \theta_i\gamma_w)\Delta z \sin\beta\cos\beta} \qquad (4.5)$$

4.4.2. Factor of safety of S-1 slope

In this section, the resulting volumetric moisture content determined from SEEP/W (Figure 4.9) was used with the infinite slope stability model to determine the corresponding factor of safety. Figure 4.11 shows the factor of safety varied with depth for the different rainfall durations. It can been seen that by increasing volumetric moisture content with depth, the factor of safety first decreased dramatically, increased slightly, and then decreased again. For the case of the 6 hours rainfall, the factor of safety decreased due to soil shear strength deceases and the unit weight of the soil slice increased with increasing depth. The minimum factor of safety, close to 1.21, occurred at the depth of 1.05 m. However, as shown in Figure 4.9, the volumetric moisture content decreased at a depth of approximately 1.1-1.3 m; therefore, the factor of safety began to increase slightly. Subsequently, the unit weight of the soil slice increased with increasing depth, and the factor of safety began to decrease. This is because the main factor controlling the factor of safety is the reduction in soil shear strength at the early stage of rainfall. A similar phenomenon can be observed at 3 and 9 hours of rainfall. The factor of safety only continuously decreases with depth after 12 hours of rainfall because the increase in volumetric moisture content is almost constant in the upper layer (the top 2 m) (Figure 4.9). A factor of safety of less than one can be observed from a depth below 1.7 m. The slope stability analysis demonstrates that failure of the S-1 slope occurred during the 1989 rainstorm with failure surfaces below 1.6 m in the upper layer. Results indicate that the simulation of the failure surface agrees well with the observation of actual slip surface.
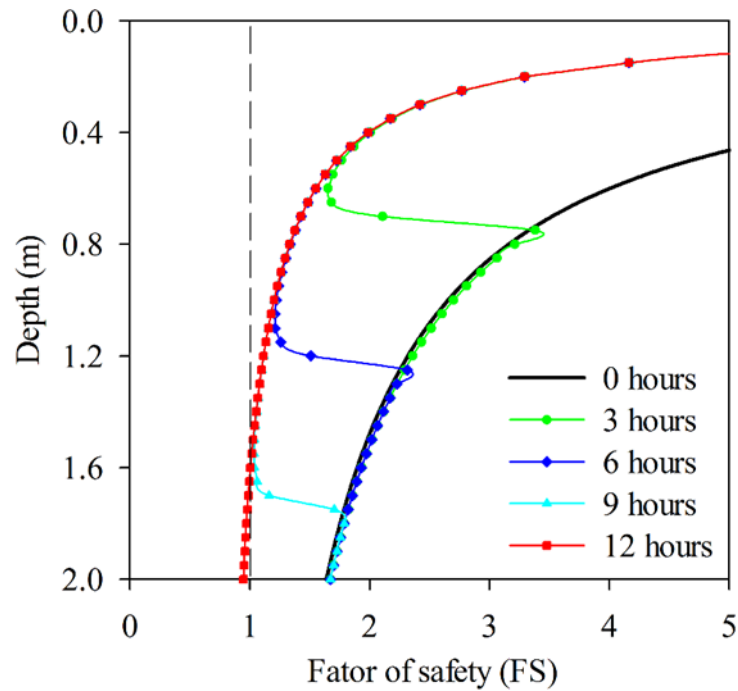
Figure 4.11. Distribution of the factor of safety with time

4.5. Random field of shear strength parameters

A series of random field of C and the tanϕ were carried out using equation (3.8). In this case, the distance between data points of $\tau = 0.05$ m was chosen. Figure 4.12 shows distribution of shear strength parameters with and without the typical random field at 6 hours rainfall. The results in Figure 4.12 (a) indicate that soil cohesion changed about 6.5 kPa along the first depth of 1.0 m, while soil cohesion changed about 14.5 kPa below a depth of 1.0 m. This is because rainfall infiltration only reached a depth of 1.0 m, which increased volumetric moisture content (as seen in Figure 4.9) and decreased soil cohesion. However, the results in Figure 4.12 (b) show that tanϕ just fluctuates about 0.54 along the whole depth since tanϕ was not affected by an increase in volumetric moisture content due to rainfall infiltration (Matsushi, 2006).

a) Typical random field of cohesion.

b) Typical random field of tanϕ
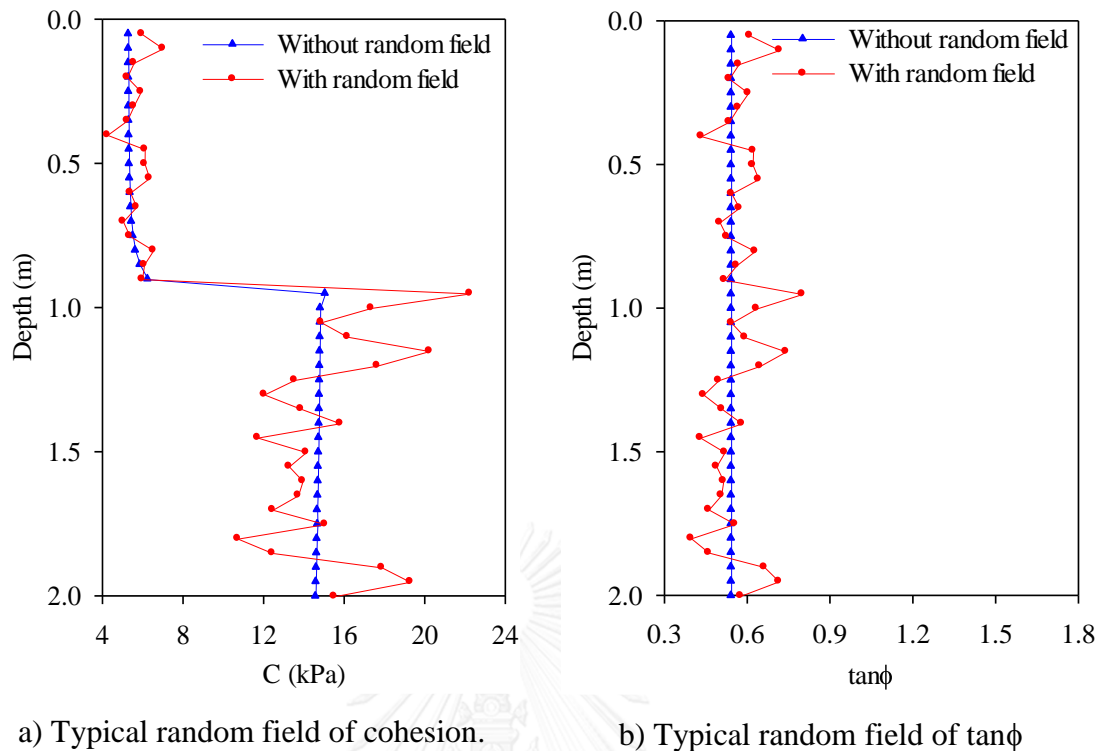
Figure 4.12. Typical random field of shear strength parameters

The input statistical parameters, such as the mean, and standard deviation are assumed to be defined at the point level. In the context of random field theory, the point variance was reduced due to the local averaging process and the reduction was indicated by a variance function, as mentioned in chapters 2 and 3. A generated random field of shear strength depends on the given autocorrelation length if the element size has a constant value of $\tau = 0.05$ m. If smaller autocorrelation length is set, the variance reduction will approximate 0, the more the fluctuation of shear strength is given. On the other hand, if a lager autocorrelation length is set, the variance of reduction will reach 1.0, the more the stabilization of shear strength is given.

Figure 4.13 shows the different distributions of shear strength parameters corresponding to different autocorrelation lengths in the random field model. Clearly, shear strength parameters became stable when the larger autocorrelation length was given, and they returned to deterministic analysis if the autocorrelation length reached a finite value.
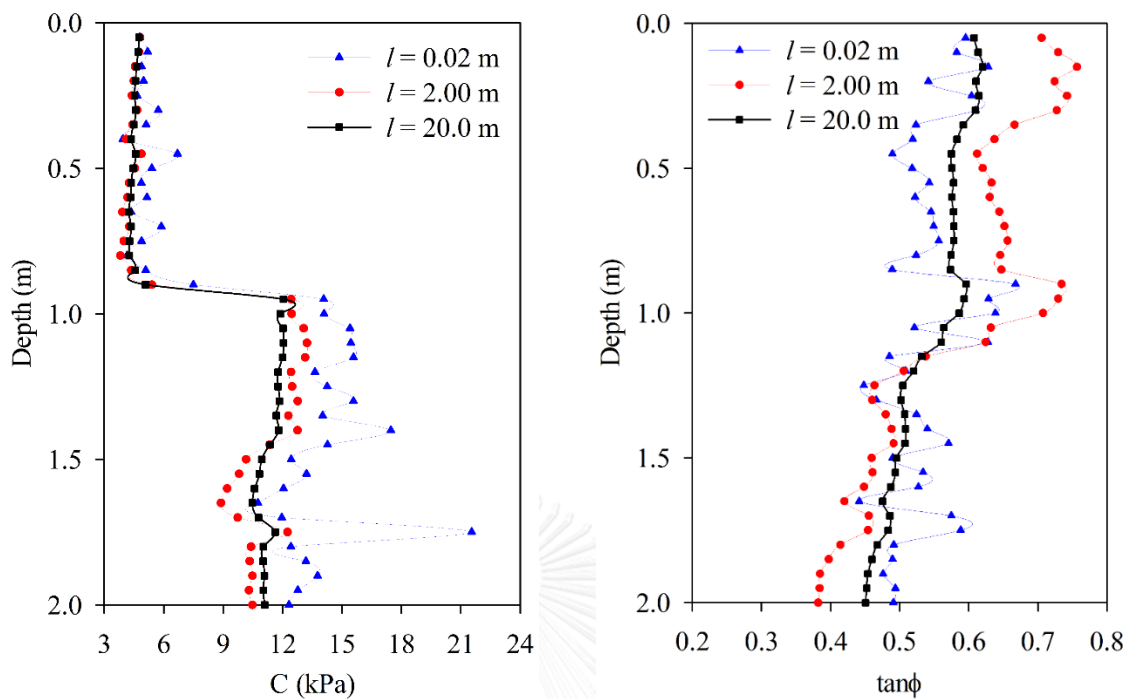
a) Effect of *l* on random field of C. b) Effect of *l* on random field of tanϕ

Figure 4.13. Effect of autocorrelation length *l* on a typical random field of shear strength parameters

4.6. Probabilistic analysis of slope S-1

4.6.1. Procedure of estimation of failure probability

A procedure for the estimation of failure probability considering the effect of spatial variability of shear strength parameters is proposed in this section, as shown in Figure 4.14. This procedure includes of the following steps:

(1) Identification of the spatial variability of shear strength parameters such as mean, coefficient of variance (cov), and autocorrelation length (*l*). Generation of *n* random fields of shear strength parameters using equation (3.8) and the Monte Carlo Simulation

(2) Repetition of the mean value of all elements in the factor of safety function (equation (4.5)) by *n* generated random fields of shear strength parameters; thus, *n* new FS functions are generated corresponding to *n* random field.

 (3) Obtaining *n* different factors of safety and then FSs which are less than 1.0 will be extracted. The failure probability is approximated by equation (3.10).

(4) Assessment of the effect of spatial variability of shear strength parameters on slope failure probability.

Identify statistical charateristic of shear strength parameters:
- Mean value (μ)
- Coefficient of variance (cov)
- Autocorrelation length (*l*)

Generate n random field
of shear strength parameters

Replace mean values
corresponding to n random field
of shear strength parameters

Obtain n factor of safety for all
random field of shear strength parameters

Extract factor of safety less than 1.0

Calculate failure probability

Assess the effect of spatial variability
of shear strength parameters on failure probability

Figure 4.14. Procedure of failure probability calculation

To analyze the probability of rainfall-induced slope failure, the total soil cohesion under unsaturated condition (C) and the frictional resistance (tanϕ) were considered as the random fields. The values of *C* and tanϕ were determined from the direct shear test results (Figure 4.7). It is noted that the value of *C* was not constant, but it tends to decrease with increasing volumetric moisture content due to rainfall infiltration. According to Retheti (1988), the covariance coefficient of the effective cohesion ($cov_{c'}$) for sandy soils and clayish soils were usually greater than 0.2. Since the effective cohesion is the same as the total soil cohesion in the saturated condition, the covariance

coefficient of the total soil cohesion (cov_C) can be set as the same value of $cov_{c'}$ (Fenton and Griffiths, 2008). The covariance coefficient of the frictional resistance ($cov_{tan\phi}$) was between 0.02 and 0.22 (Phoon and Kulhawy, 1999). In order to verify slope failure during the rainstorm and evaluate the effect of each shear strength parameter, the slope failure probability was calculated using the same value of covariance coefficient corresponding to $cov_C = cov_{tan\phi} = 0.2$. In addition, to simulate the effect of heterogeneous soil characteristics on the probabilistic calculation, the autocorrelation length l was varied from 0.02 to 2.0 m for the description of the spatial autocorrelation length of random fields C and $tan\phi$. Table 4.5 summarizes the statistical characteristics of soil shear strength parameters used for probabilistic analysis.

Table 4.5. Statistical characteristic of soil shear strength used for probabilistic analysis

Parameters	Mean value	cov	autocorrelation length (m)
C (kPa)	$35.8e^{-4.81\theta}$	0.2	$0.02 \leq l \leq 2.0$
$tan\phi$	0.5384		
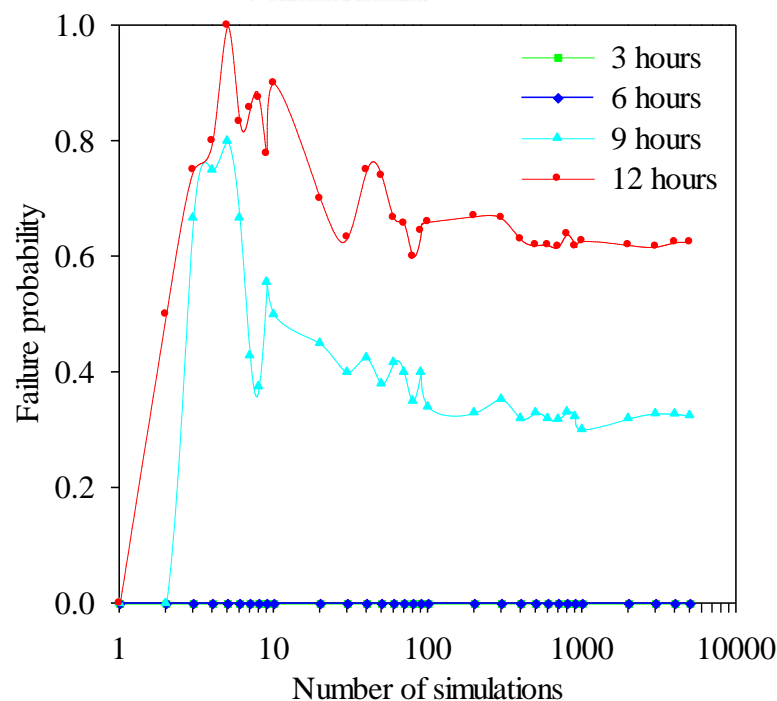
Figure 4.15. Convergence of the failure probability at different time

A series of random fields of C and tanϕ were carried out using the random model and Monte Carlo Simulation. Figure 4.15 shows the convergence of the estimated probability of failure for the slope, which indicate that the failure probability can be converged when the generated samples exceed 2,000. In this study, 5,000 sets of the random fields C and tanϕ were used as input shear strength parameters for probabilistic stability analysis. Then, the factor of safety and critical depth were recorded for each generated random field C and tanϕ; failure probability was approximated based on equation (3.10).

4.6.2. Effect of autocorrelation length

In this section, probabilistic analysis of rainfall-induced slope failure is illustrated. The autocorrelation lengths between 0.02 to 2.0 m were implemented for both random fields of C and tanϕ in this study. Figure 4.16 shows the histogram of frequency of each critical failure surface which occurred at different depths for the autocorrelation lengths of 0.02 and 2.0 m at 9 and 12 hours of rainfall duration. In Figure 4.16 (a) and (b) indicate that the critical failure surface most likely occurred at a depth of approximately 1.0 - 1.7 m after 9 hours of rainfall. This finding means that the wetting front due to rainfall infiltration only decreases the shear strength of soil at the slope's upper portion in the early stages of infiltration. As infiltration progresses and the wetting front moves down, the critical surface continuously increases in depth until the wetting front reaches the base of the upper layer. Finally, the highest frequency of critical surface failure occurred at the base of the upper layer, as shown in Figure 4.16 (c) and (d). Since the highest frequency of critical surface failure took place between 1.5 to 2.0 m depth of the upper layer after 9 hours of rainfall, as seen in Figure 4.16, the failure mechanism can be characterized as a shallow failure, where the critical failure surfaces were located above the interface between the weathered soil and bedrock. Comparing the previous studies of Cho (2014) and Dou et al. (2015), the failure mechanism always occurs at the interface between the weathered soil and bedrock during rainfall infiltration. Figure 4.16 also indicated that the frequency of the critical surface failure was affected by the autocorrelation length. In the histogram shown in Figure 4.16 (a) and (c) at $l = 0.02$ m display smaller frequencies at the critical failure surface than the histogram in Figure 4.16 (b) and (d) for $l = 2.0$ m. This is

because the lower autocorrelation length, which exhibits highly non-homogeneous soil, has the critical surface moving upward. Conversely, the higher autocorrelation length provided an increased frequency probability that the critical failure surface would be located at the weakest part of the upper layer as the random field becomes more spatially uniform.
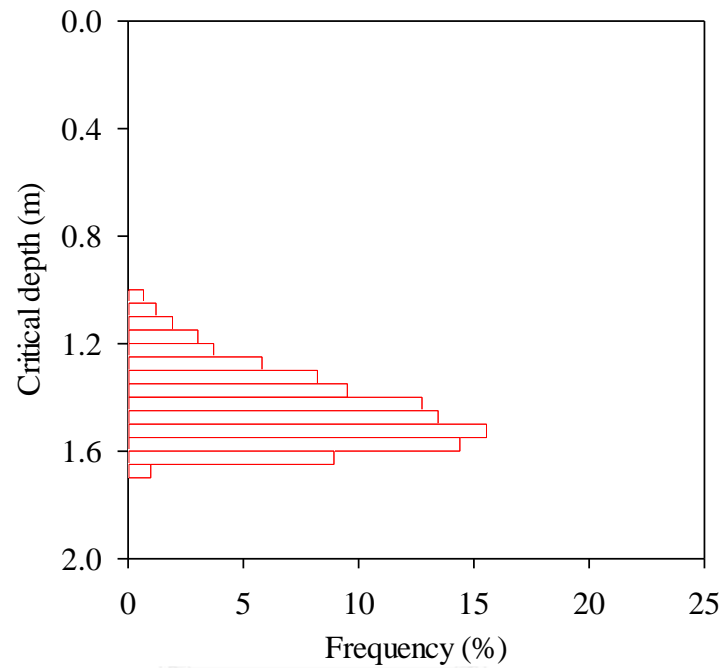
a) After 9 hours, $l = 0.02$ m
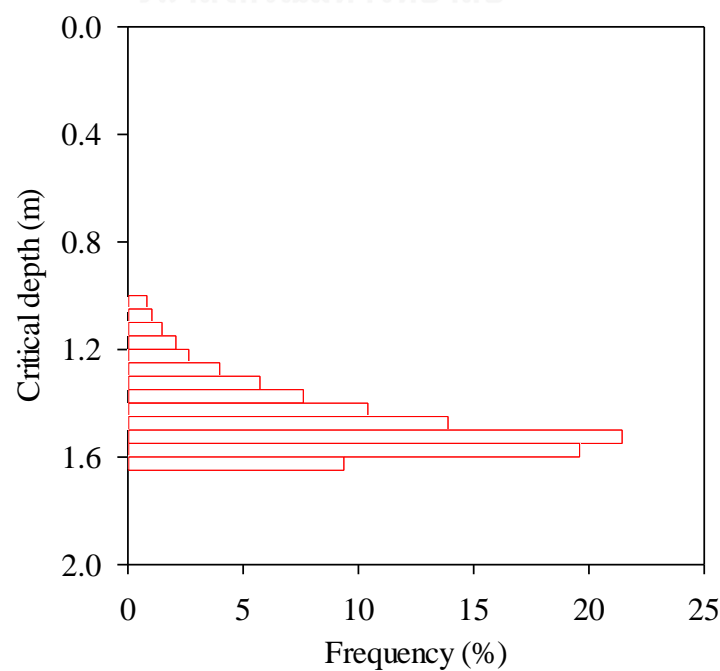
b) After 9 hours, $l = 2.0$ m
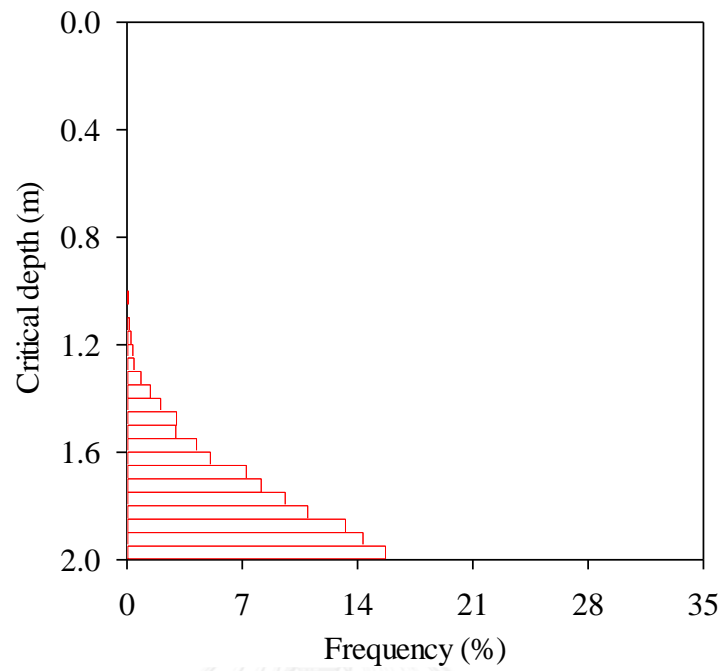
c) After 12 hours, $l = 0.02$ m
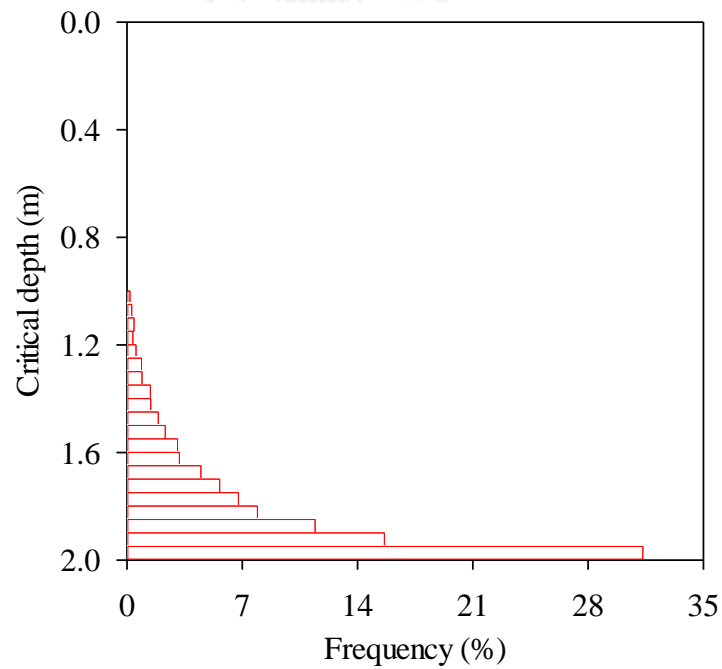
d) After 12 hours, $l = 2.0$ m

Figure 4.16. Histogram of the critical depth at two different times from random field analysis $\text{cov}_C = 0.2$; $\text{cov}_{\tan\phi} = 0.2$)

Figure 4.17 shows the influence of autocorrelation length l in the range of $0.02 \leq l \leq 2.0$ m on the failure probability at different points in rainfall duration. The failure probability was calculated at the critical failure surface corresponding to the minimum factor of safety of the deterministic analysis. The results indicate that the failure probability increases dramatically as infiltration progresses, and soil slopes with smaller values of autocorrelation length have a smaller failure probability at the early stages of infiltration. However, the failure probability for cases with smaller values of correlation length was greater than those with larger values of autocorrelation length after the rainfall duration exceeded approximately 9.5 hours. This can be referred to as a critical rainfall duration causing slope failure. It should be emphasized that all curves cross over at the failure probability of $P_f = 0.5$ occurring at the critical rainfall duration. This is because the cumulative probability of FS for all autocorrelation lengths is equal to 0.5 at the corresponding safety factor of FS = 1.0, as shown in Figure 4.18. Therefore, the location of the failure surface can be derived from probabilistic analysis, in which $P_f = 0.5$.
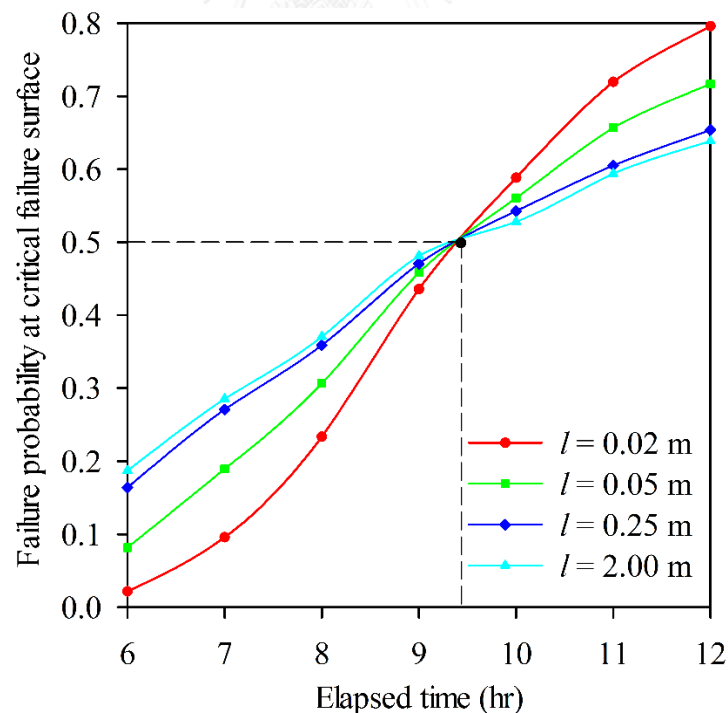
Figure 4.17. Effect of l on the failure probability calculation at different times from random field analysis ($\text{cov}_C = 0.2$; $\text{cov}_{\tan\phi} = 0.2$)
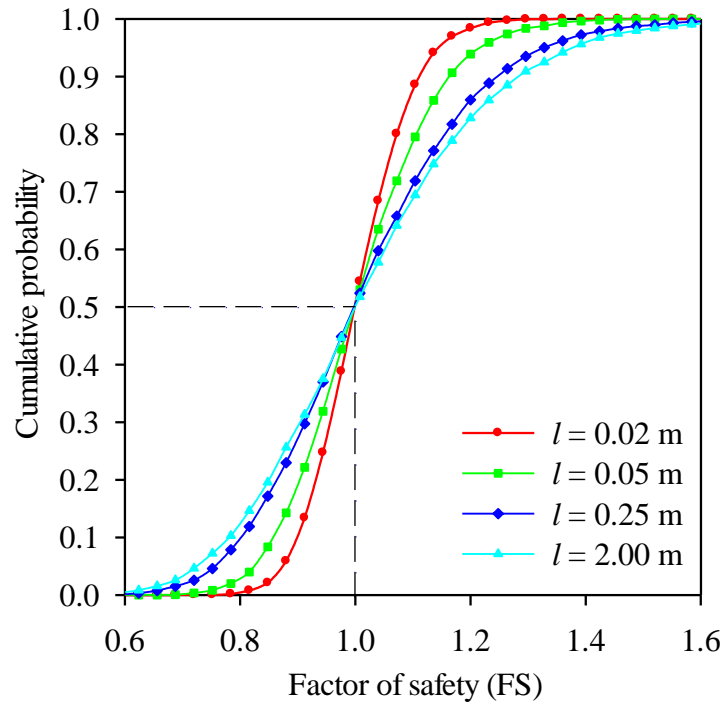
Figure 4.18. The cumulative probability of the FS at the critical rainfall duration of 9.5 hours from random field analysis ($cov_C = 0.2$; $cov_{tan\phi} = 0.2$)
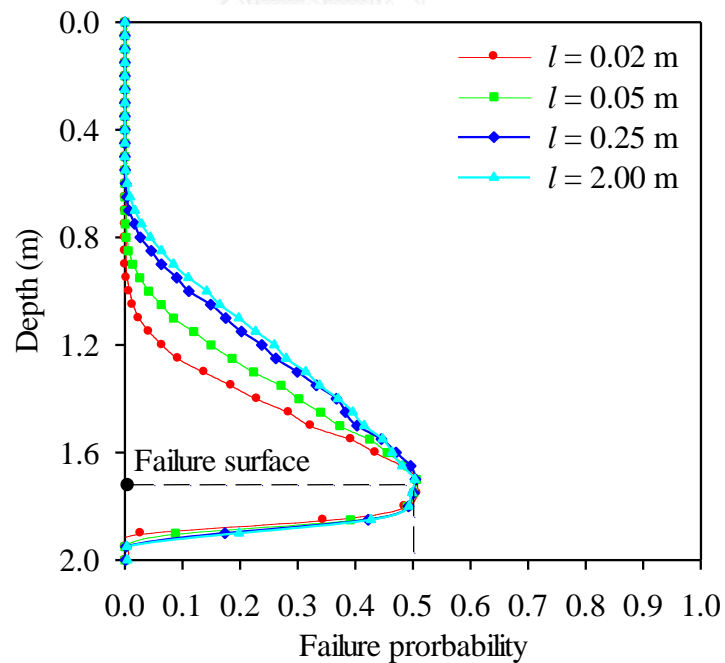
Figure 4.19. Failure probability distribution and the corresponding failure surface at the critical rainfall duration of 9.5 hours from random field analysis ($cov_C = 0.2$; $cov_{tan\phi} = 0.2$)

In order to obtain the failure surface, the failure probability distributions were calculated at the point of critical rainfall duration. Figure 4.19 shows the distribution of failure probability with depth for all autocorrelation lengths. The corresponding failure surface was also obtained at the failure probability of $P_f = 0.5$, with the failure surface located at the depth of 1.7 m of slope while the actual failure surface during the 1989 storm occurred at the depth of 1.6 m, which approximated the analysis result indicating the probabilistic analysis with random fields was an effective predictor to locate critical failure surfaces and determine critical rainfall durations.

4.6.3. Effects of random fields of shear strength parameters

In the previous assessment, two random fields of C (total soil cohesion under unsaturated condition) and tanϕ (frictional resistance) were considered for the failure probability calculation. One might want to identify which random field has a greater effect on the slope failure. In order to evaluate the influence of each random field, a series of FS for each random filed alone and both random fields were calculated at the failure surface which occurred at the critical rainfall duration, and the cumulative probability curves of FS for these cases were obtained at the different autocorrelation lengths. Figure 4.20 compares the cumulative probability curve of FS considering two random fields together with the curve obtained by ignoring one random field at a different autocorrelation length. The difference between the curves considering two random fields and the curve neglecting one random field reflects the importance of that random field for failure probability calculation. As shown in Figure 4.20, when random field tanϕ was ignored, the difference of probability was more than the difference by neglecting random field C. It turns out that shallow failure is mainly caused by reduction in soil cohesion during rainfall infiltration. In addition, this difference trend to increase with the increase of autocorrelation length. This finding indicates that the influence of each random field for non-homogeneous soil is somewhat important.
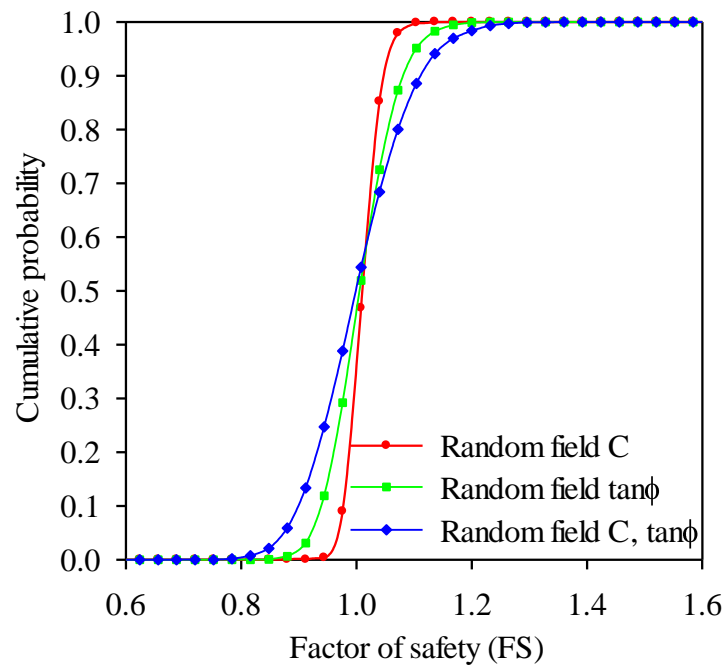
a) $l = 0.02$ m.
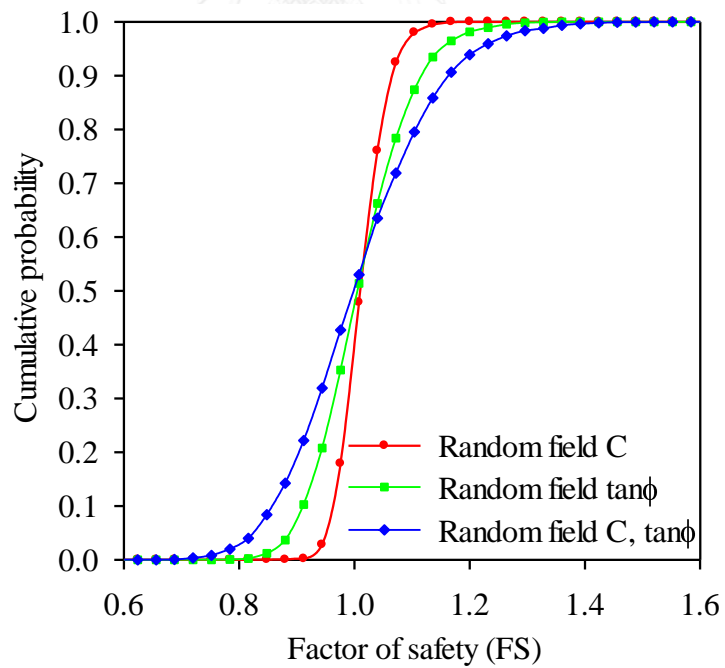
b) $l = 0.05$ m.
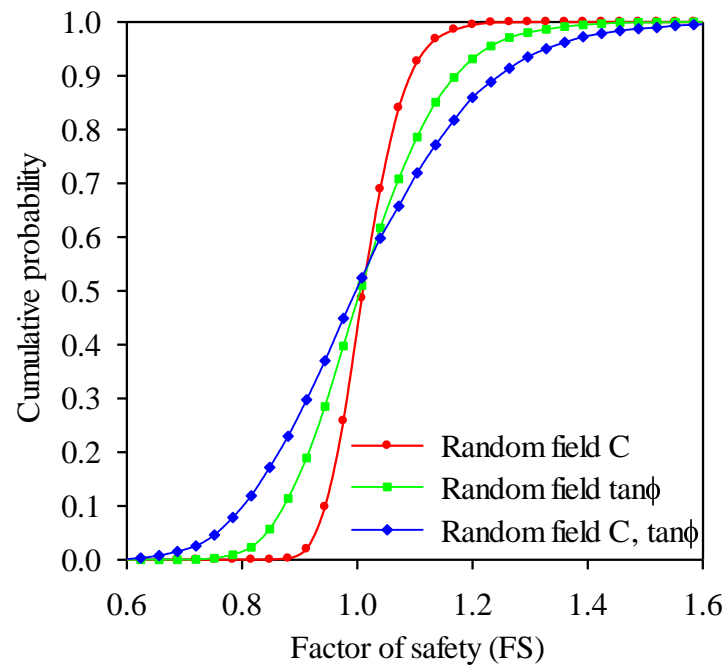
c) $l = 0.25$ m.
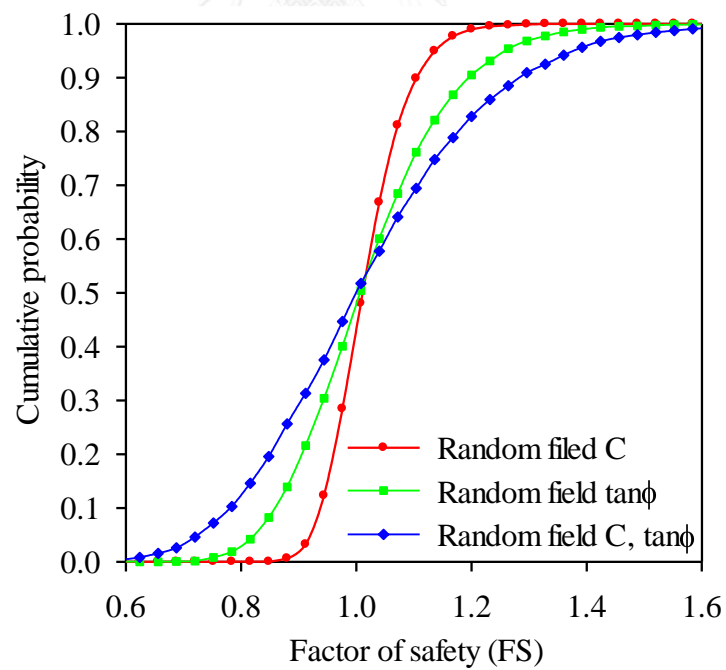
d) $l = 2.0$ m.

Figure 4.20. Effect of random field C and tanϕ on the slope failure at the critical rainfall duration of 9.5 hours from random field analysis ($cov_C = 0.2$; $cov_{tanϕ} = 0.2$)

4.7. Summary

This chapter examined the spatial variability of shear strength parameters on rainfall-induced landslides. A case study of a sandstone slope with deep impermeable bedrock in a site in Japan was selected for comparison. An unsaturated seepage and infinite slope stability analysis were applied using a probabilistic method. To simulate shallow failure, the reduction in soil shear strength due to the increase in volumetric moisture content was considered. A series of Monte Carlo simulations were conducted to investigate the effect of a random field on C and $\tan\phi$ parameters. The analysis results were then compared to an actual occurrence of slope failure during a storm in 1989. The results indicate that the proposed random field was essential to predict failure surfaces and critical rainfall duration (The time period of rainfall which triggers slope failure).

CHAPTER 5: THE INFLUENCE OF SPATIAL VARIABILITY OF ROOT COHESION ON RAINFALL INDUCED SLOPE STABILITY ANALYSIS: A CASE STUDY OF A RESIDUAL SOIL SLOPE IN THAILAND

5.1. Introduction

As discussed in Chapter 2, it is well known that vegetation has an effect on slope stability analysis. This is effected through various processes, including modification of volumetric moisture content; root reinforcement; surcharging; arching; and wind loading. Many studies have been conducted to quantify the effects of vegetation on slope stability with both the limit equilibrium method and the finite element method (Lin et al., 2010; Chirico et al., 2013; Wu, 2013; Tiwari et al., 2013; Leung et al., 2015). However, slope stability analysis considering the effect of vegetation under heavy rainfall has not been investigated. In addition, previous studies only mentioned in their hypothesis artificial rainfall or lacked monitoring data (soil suction or moisture content) to verify the proposed model. Thus, their analyses could not respond to natural conditions slope stability.

In this chapter, a full-scaled field monitoring test was implemented on an unsaturated soil slope in Nakorn Nayok Province, Thailand (Jotisankasa et al., 2009) to model the effect of heavy rainfall and the spatial variability of root cohesion on slope stability analysis. Therefore, the objectives of this chapter can be stated as follows:

1. To simulate saturated-unsaturated seepage analysis in two dimensions and verify the proposed model.

2. To incorporate the effects of typical root distribution into the limit equilibrium method for the vegetated slope stability model.

3. To generate random fields of root cohesion in order to assess the influence of spatial variability of root cohesion on failure probability of a vegetated slope.

5.2. Characteristics of study the slope (Thadan slope)

The study site is located near Thadan dam in Nakorn Nayok Province, Thailand (hereafter, referred to as Thadan slope) about 200 km northeast of Bangkok. A shallow failure in 2004 was triggered by a heavy rainfall spanning over three days which

amounted to a total rainfall of about 300 mm, or an average of about 100 mm/day (Figure 5.1 (a)). After failure, the slope was redesigned and constructed with compacted residual soil available on-site. The slope was also populated with vetiver grass, as seen in Figure 5.1 (b). The repaired soil slope was investigated with a lightweight dynamic penetrometer (Jotisankasa et al., 2009) which indicated the thickness of the residual soil layer was 2.0 to 3.0 m. Below the residual soil lies the slightly weathered volcanic rock which can be defined as impermeable bedrock.

Figure 5.1. Thadan slope (a) after failure in 2004 and (b) current state
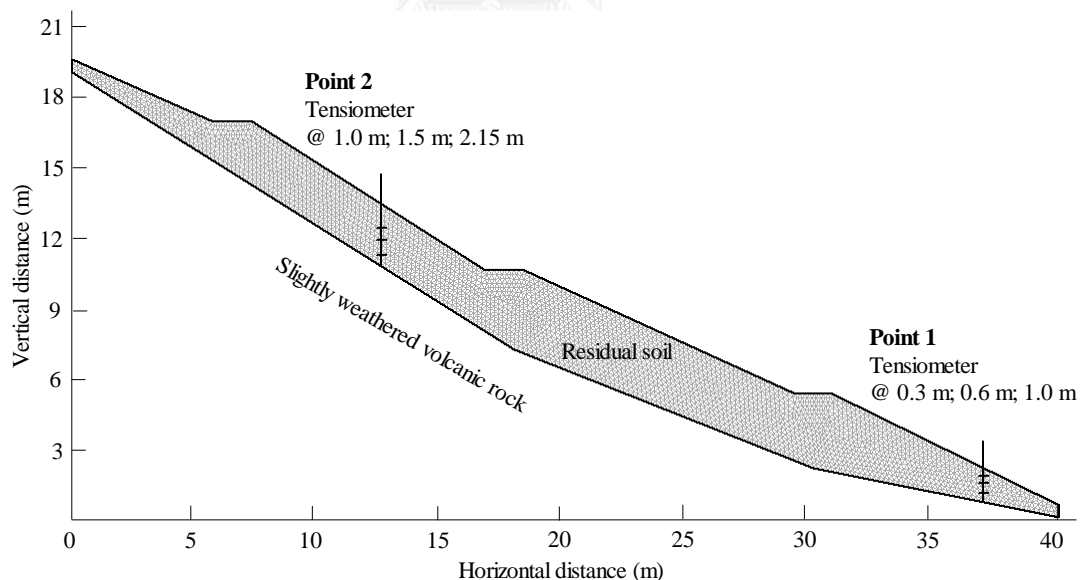
Figure 5.2. Field instruments on the Thadan slope (after Jotisankasa et al., 2009)

Figure 5.2 displays the cross-section of the study site considering the residual soil layer. The slope angle of 26^0 with respect to the horizontal plane was averaged along the ground surface. Field instrumentation was deployed on the slope using tensiometers, which were installed at Point 1 (lower station) and Point 2 (upper station) to monitor

pore water pressure at depths varying from 0.3 to 2.15 m during rainfall, as depicted in Figure 5.2.

The geology in the area of the slope consists of undifferentiated Permo-triassic volcanic rock, including rhyolite, andesite, tuffs, and agglomerate (Royal Irrigation Deparment, 2004). The undisturbed samples were collected using a thin-walled tube sampler with a diameter of 63 mm from depths of 0.5 - 1.0 m. The basic properties of the residual soil are summarised in Table 5.1. According to the Unified Soil Classification System (USCS), the residual soil can be classified as silty soil with medium plasticity (MH/ML).

Table 5.1. Physical soil properties

Soil type	Saturated unit weight (kN/m^3)	Liquid Limit (%)	Plasticity Index (%)	Grain-size distribution (%)			
				Clay	Silt	Sand	Gravel
MH/ML	17.61	46-51	6-18	31.9-36.7	38.9-53.9	13.7-18.9	0.5-5.5

5.3. Seepage analysis of the Thadan slope

For the seepage analysis in an unsaturated soil layer of the Thadan slope, a transient state nonlinear partial differential equation (2.35) was employed using an iterative finite element scheme in Geo-studio software. To obtain a reliable result, the time step and element size should also be defined in advance (Van Dam and Feddes, 2000; Smith and Griffiths, 2004; Caviedes-Voullième et al., 2013). In this analysis, a small time step increment of 300 seconds, and a global element size of 0.2 m were employed.

5.3.1. Collection of SWCC parameters and field test of hydraulic conductivity

The relationship between soil suction and volumetric moisture content (soil-water characteristic curve, SWCC) of the residual soil was determined with a KU-tensiometer for samples in both dry and wet conditions (Jotisankasa and Vathananukij, 2008). The SWCC and its curve-fitting van Genuchten model are presented in Figure 5.3. The saturated permeability was determined from a constant head borehole permeability test at different depths at the study site, using the method described in Garga and Blight (2012). The results indicate a permeability of 2×10^{-4} m/s near the surface falling

abruptly to 4×10^{-8} m/s at a depth of about 1.8 m, as shown in Figure 5.4. The higher value of permeability near the surface may be due to the effect of root holes as well as a lower overburden stress level. Since the residual soil layer of the slope is rather homogeneous, the average saturated permeability of 2.9×10^{-5} m/s was used to define the hydraulic conductivity function. Table 5.2 summarizes the fitting parameters of the soil water characteristic curve and the average saturated permeability of residual soil as input parameters for seepage analysis.
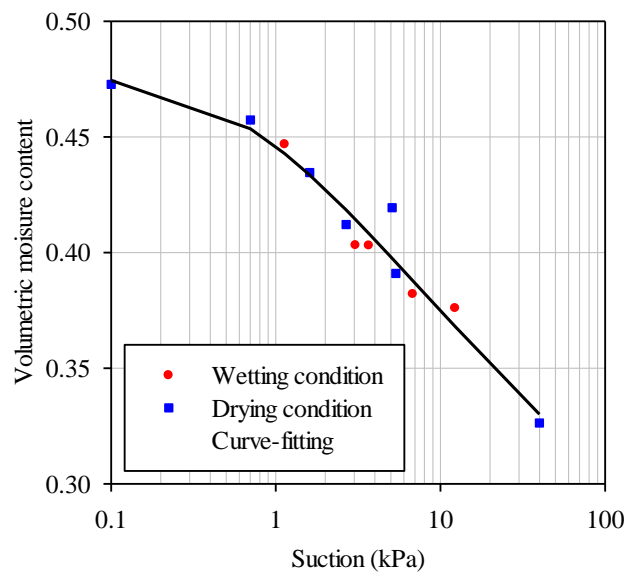
Figure 5.3. SWCC of residual soils (data from Jotisankasa and Vathananukij, 2008)
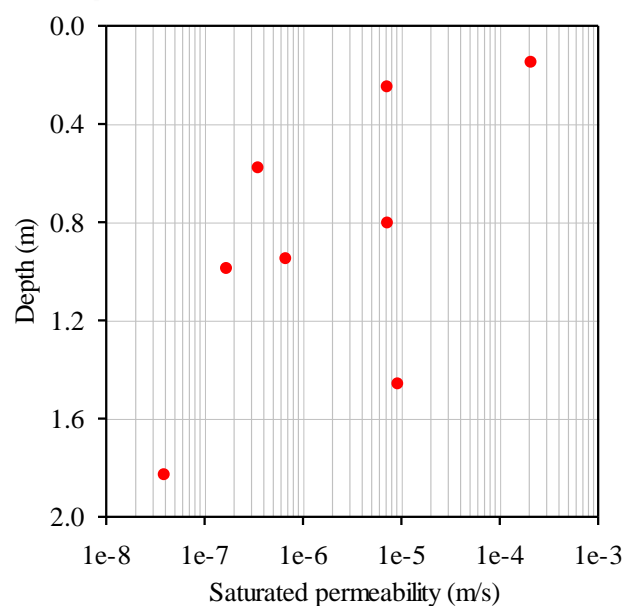
Figure 5.4. Saturated permeability varied with depth from field permeability tests

Table 5.2. SWCC parameters and saturated permeability

Type	Parameters	Value
Residual volumetric moisture content	θ_r	2.1×10^{-4}
Saturated volumetric moisture content	θ_s	0.473
Fitting	α (1/kPa)	0.902
parameters	n	1.101
Saturated permeability	k_s (m/s)	2.9×10^{-5}

5.3.2. Rainfall intensity record

In order to simulate the effect of heavy rainfall that can lead to slope failure, the rainfall intensity in the period 03-Sept-2008 to 24-Sept-2008 was chosen in this study, as shown in Figure 5.5. This was the period with maximum pore pressure readings observed during the monitoring program starting from 2007. The maximum rainfall intensity of this period was observed on 12-Sept-2008 and found to be over 120 mm/day. The rainfall record was classed into 21 periods with an interval of 1 day for the proposed model. In the finite element model, the rainfall intensity was assigned on the ground surface as the transient flux boundary. The pore water pressure and volumetric moisture content of the residual soils in response to this imposed flux boundary were then calculated.
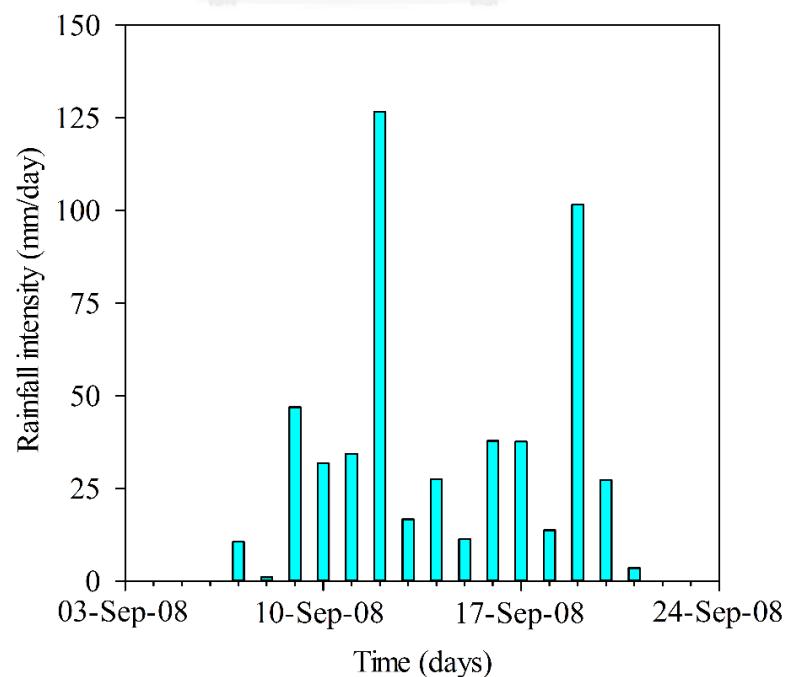
Figure 5.5. Recorded rainfall intensity

5.3.3. Initial and boundary condition

In this section, an unsaturated-saturated flow model was simulated for both steady state analysis and transient state analysis. The SWCC parameters and the saturated permeability values from laboratory and field tests were used as input parameters in the seepage model to calculate pore water pressure and volumetric moisture content during the period of rainfall under investigation. In the initial condition, a steady state infiltration rate, equal to an average rainfall intensity of 7.54 mm/day from 01-Jan-2008 to 31-Dec-2008, was assigned on the ground surface of the slope. This was meant to simulate the long-term precipitation which gave rise to a steady state initial condition before the simulated major heavy rainfall event. A zero flux boundary was imposed at the bottom of the domain where slightly weathered volcanic rock was located. For the transient infiltration analysis, the top boundary of the model was equivalent to the rainfall intensity recorded during the period of 03-Sept-2008 to 24-Sept-2008. Since the ground surface was close enough to interact with the bottom of the residual soil at the crest and toe of the slope, a zero flux condition was set for the left and right boundary condition. The model ignored the effect of evapotranspiration, which did not have a major contribution to slope stability in the rainy season (Greenway, 1987; Coppin and Richards, 1990). No ponding on the top surface of the soil slope could be reasonably assumed due to the fact that when the rainwater exceeds the infiltration capacity of the soil, the excess water drains away as surface runoff. Figure 5.6 shows the initial total pressure head distribution before the transient state seepage analysis for a steady state using an average rainfall intensity of 7.54 mm/day. The initial total pressure head was then used to calculate transient pore water pressure during heavy rainfall.

5.3.4. Monitoring and simulating pore water pressure

The pore water pressures were monitored at two different locations along the slope (i.e., upper and lower stations) using miniature tensiometers developed by Jotisankasa et al. (2007). This device is based on MEMs pressure sensor technology capable of measuring both positive and negative pore water pressure with a range from -80 to 600 kPa. Each tensiometer was installed at depths of 0.3, 0.6 and 1.0 m at Point 1 and at depths of 1.0, 1.5, 2.15 m at Point 2 as shown in Figure 5.2. The pore water

pressure corresponding to the rainfall intensity record during the period of 03-Sept-2008 to 24-Sept-2008 was also obtained as presented in Figure 5.7. The monitored pore water pressures were used for comparison with those of the seepage analysis to verify the proposed seepage model.
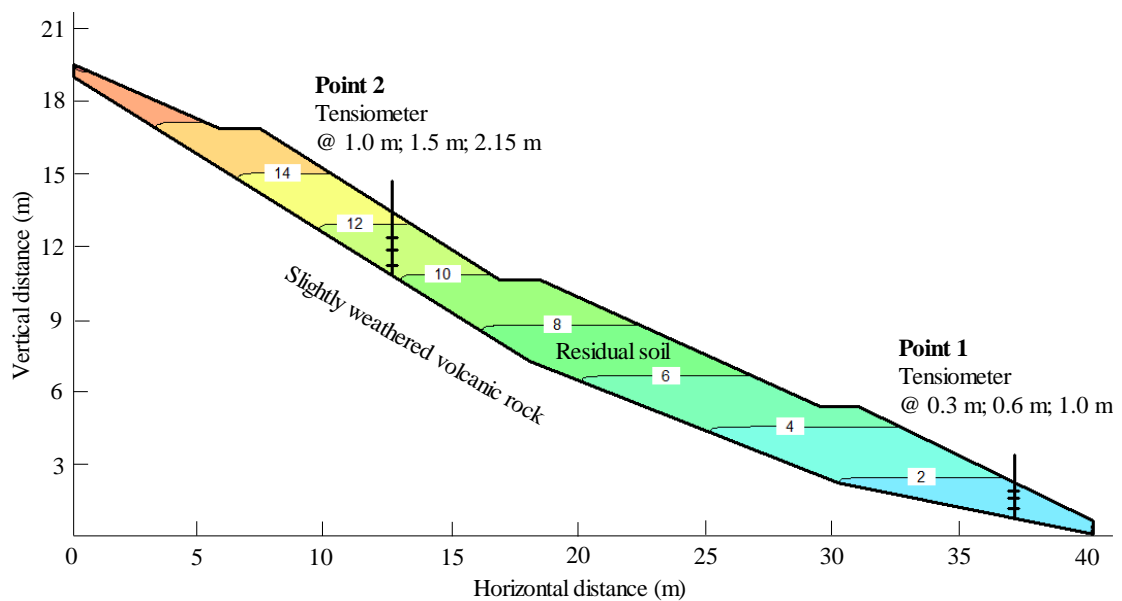
Figure 5.6. Initial total pressure head (m)

5.3.4.1. Effect of rainfall intensity

Figure 5.7 (a) and (b) present the results of the transient seepage analysis at various depths at Point 1 and Point 2, respectively. The pore water pressure in the lower area (Point 1) gradually changed in response to rainfall entering at shallow depths, while the change appeared more sudden in the upper area (Point 2) at deeper depths when rainfall intensity exceeded 100 mm/day. At Point 1, positive pore water pressure appeared at different depths one day before the highest rainfall intensity and almost remained constant until the period of rainfall ended. This was expected as the free-draining saturated surface was located near the toe of the slope. At Point 2 however, the positive pore water pressure could only be observed at different depths one day after the highest rainfall intensity and reappeared at deeper depths (1.5 and 2.15 m) after 19-Sept-2008. This demonstrated a kind of delayed infiltration behaviour at the deeper depth. The pore water pressures measured at different depths were also drawn on these figures to demonstrate the accuracy of the proposed seepage model. As shown in Figure 5.7 (a), the pore water pressures obtained from simulation were higher than those

measured at shallower depths (0.3 and 0.6 m) in the first period of rainfall (no rainfall). This is because the assumed initial flux boundary condition of 7.54 mm/day, based on long-term rainfall measurement, was set to ground surface and therefore may not represent the short-term distribution of the pore water pressure that would be affected by some daily climate effects (e.g. evapotranspiration) especially at a shallow depth. Subsequently, the simulation curves and the measurement curves become more consistent from the beginning of rainfall to the end of the period of rainfall. At 1.0 m depth of the lower station (Figure 5.7 (a)), the pore water pressure from simulation was slightly greater than those actually measure after a few days rainfall (09-Sept-2008). This slight difference can be explained by the fact that in the analysis, the undrained flux boundary was at the bottom of the domain and consequently a small part of rainwater would still remain in soil slope. In reality, however, a small amount of seepage may occur out of the bottom domain.
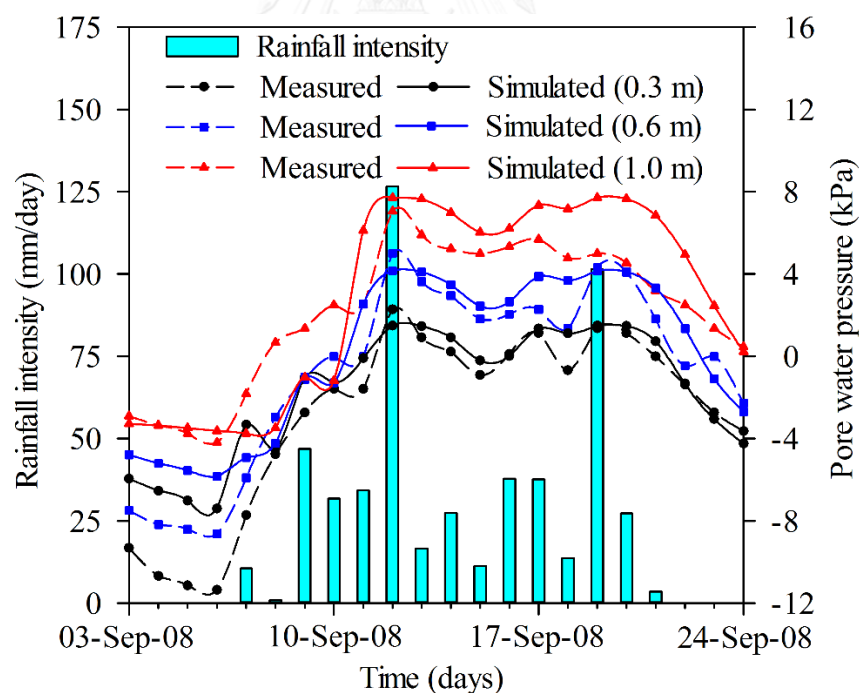
a) Point 1 (Lower station)
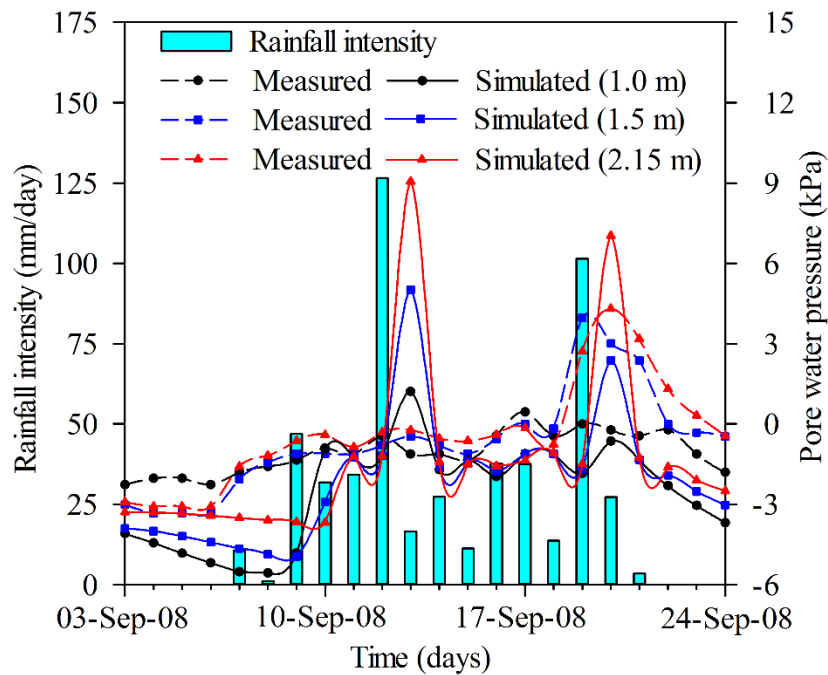
b) Point 2 (Upper station)

Figure 5.7. Comparisons between measured and simulated pore water pressures

Unlike the results in Figure 5.7 (a), the pore water pressure response in the upper area in Figure 5.7 (b) indicates that the loss of soil suction in the first period of rainfall affected not only the initial infiltration but also the downslope seepage from the crest to the toe slope. In the same way, the modelled downslope seepage can occur more easily than the actual response because the modelled soil was assumed to be homogeneous in this analysis. This would explain why the measured pore water pressure was greater than the simulated value. However, one day after the highest rainfall record (13-Sept-2008), the results at different depths showed a better consistency between the modelled and actually measured pore water pressure. In addition, the pore water pressure response characteristics were also expected to be strongly affected by other factors, such as geomorphological and geological conditions.

5.3.4.2. Predicted pore water pressure

Figure 5.8 (a) and (b) show predictions of pore water pressure distribution with depths at Point 1 and Point 2, respectively during the period of rainfall. As seen in Figure 5.8 (a), at the beginning of rainfall (before 05-Sept-2008), a decrease in pore water pressure occurred at shallow depths which tended to increase because of water

redistribution during periods of no rain, while in contrast, the pore water pressure remains virtually unchanged at the greater depth. On 07-Sept-2008, pore water pressure only exceeded the initial condition at depths above 0.4 m as a consequence of limited rainfall infiltration. Below 0.4 m depth, the pore water pressure curve tended to be similar to the pore water pressure curve on 05-Sept-2008. Since rainfall had continuously increased on 10-Sept-2008, the pore water pressure reached a positive value at a depth below 1.1 m. On the other hand, the ground above 1.1 m depth remained unsaturated. After the highest rainfall intensity occurred (13-Sept-2008), the saturated zone reached the bedrock (1.4 m depth) while the pore water pressure increased linearly with depth. The rainfall intensity declined rapidly on 16-Sept-2008 as pore water pressure decreased with the same range value with depth and this tendency remained until there was no record of rainfall on 24-Sept-2008. In addition, it was noted that the pore water pressure distributions on 13-Sept-2008 and 20-Sept-2008 were nearly identical even though rainfall intensity on these days were different. This can be explained as when rainfall intensity exceeded the quantity of 100 mm/day, the rainwater in excess of infiltration capacity could not infiltrate through the ground surface and thus was converted to runoff. This suggests that rainfall at that particular time reached flow rate exceeding the infiltration capacity of the soil. A similar explanation can be provided for the pore water pressure measurements at the upper station (before 07-Sept-2008), as shown in Figure 5.8 (b). However, on 10-Sept-2008, as the pore water pressure increased to approximately -1.5 kPa, the soil slope only became saturated near the bedrock because the amount and duration of rainfall were insufficient to induce the pore water pressure to rise to the higher area. When the highest rainfall intensity occurred (125 mm/day), the soil profile was completely saturated below a depth of 0.8 m, and almost saturated above this level on 13-Sept-2008. Rainfall intensity dropped to 37 mm/day on 16-Sep-2008 which caused an obvious decrease of pore water pressure at a greater depth since seepage occurred down slope due to gravity. Unlike the case of the lower station, pore water pressure on 20-Sept-2008 was less than the value on 13-Sept-2008 below 0.8 m depth and the soil slope had not been completely saturated above 0.8 m. This is explained by the fact that soil thickness at the upper station was greater than at the lower station. It can be demonstrated that even with the highest rainfall intensity assumed in this analysis, the whole soil profile would still not be

completely saturated at the upper station. Therefore, runoff might not appear at the upper location as the infiltration and seepage continued.
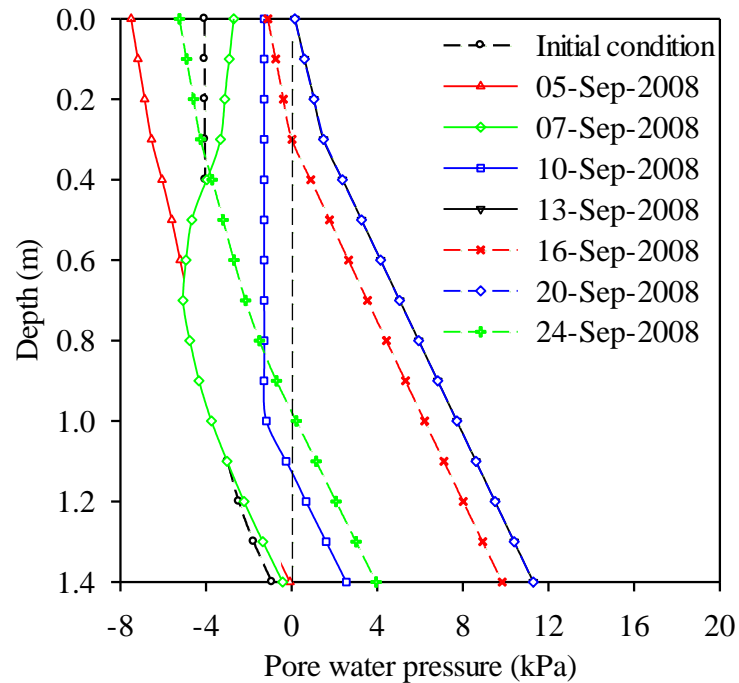
a) Point 1 (Lower station)
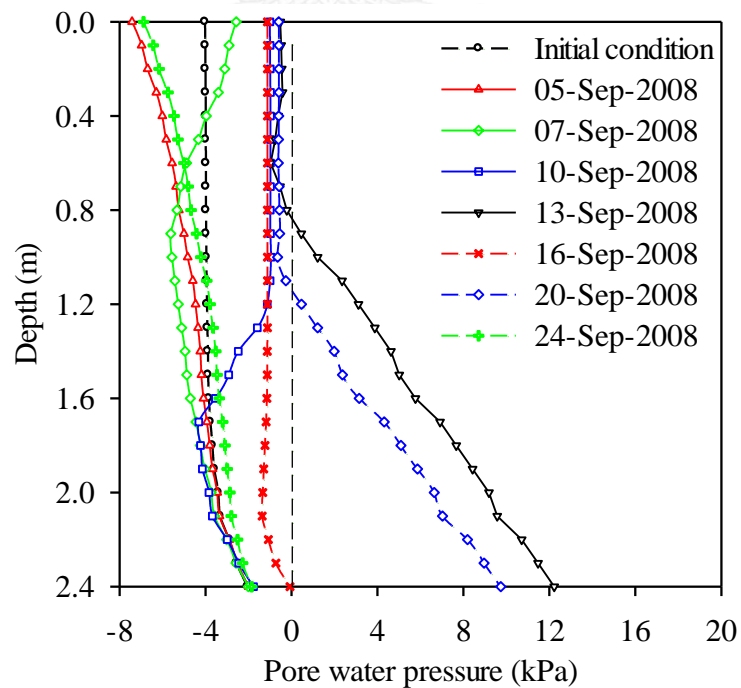
b) Point 2 (Upper station)

Figure 5.8. Prediction of pore water pressure distribution with depth

5.4. Stability analysis of the Thadan slope including vegetation

For a vegetated slope under unsaturated-saturated conditions, the shear strength can be expressed by the primary influence of root reinforcement, as suggested by Wu et al. (1979) in combination with the Mohr-Coulomb failure criterion (Fredlund et al., 1978). Thus, the shear strength is represented as:

$$\tau_f = c' + c_r + \sigma' tan\phi'$$
(5.1)

where c' is the effective soil cohesion, c_r is the root cohesion, σ' is the effective stress, and ϕ' is the effective friction angle. The effective stress can be computed by the suction stress-based equation (Lu and Likos, 2006).

$$\sigma' = \sigma - u_a - \sigma^s$$
(5.2)

where σ is the total stress due to the self-weight of the soil, u_a is the pore air pressure which is zero at the atmospheric condition, and σ^s is the suction stress which can be expressed as a function of matric suction ($u_a - u_w$) (Lu et al., 2010; Fredlund et al., 2012) thus:

$$\sigma^s = -\frac{\theta - \theta_r}{\theta_s - \theta_r}(u_a - u_w)$$
(5.3)

With the incorporation of equations (5.1), (5.2), and (5.3) the shear strength of a vegetated slope can be defined under soil-root composite for saturated-unsaturated conditions as follow:

$$\tau_f = c' + c_r + \left[(\sigma - u_a) + \frac{\theta - \theta_r}{\theta_s - \theta_r}(u_a - u_w) \right] tan\phi'$$
(5.4)

Since the weight of grass was considered negligible and there was no traffic load on the slope, the weight of each slice per unit base area (W_i) from the slope surface to the potential failure surface was only contributed by soil, which can be expressed as:

$$W_i = \sum_{i=1}^{n} \gamma A_{si}$$
(5.5)

where γ is the unit weight of the soil. To simplify the calculation in the transient slope stability analysis, γ can be approximated as the saturated unit weight for both saturated and unsaturated conditions during the rainy season. In equation (5.5), A_{si} is the cross-sessional area of each slice.

Finally, the factor of safety with consideration of the effect of vegetation on slope stability during rainfall infiltration based on equation (3.3) can be written as:

$$FS = \frac{\sum_{i}^{n}(c'+c_r)l_i + W_i cos\beta_i tan\phi' - \left(\frac{\theta-\theta_r}{\theta_s-\theta_r}\right)u_w l_i tan\phi'}{\sum_{i}^{n}W_i sin\beta_i} \tag{5.6}$$

The computed field of volumetric moisture content and pore water pressure from transient seepage analysis are then used to calculate the factor of safety. The results are verified whether or not slope failure occurs in the periods of heavy rainfall.

5.4.1. Slopes without root cohesion

In this section, limit equilibrium analysis was performed to investigate slope stability during periods of rainfall. The resulting pore water pressure and volumetric moisture content calculated from SEEP/W was then used as input in SLOPE/W to determine the corresponding factor of safety. The effective shear strength parameters were calculated on the undisturbed specimens using the drained direct shear test under a saturated condition. The effective soil cohesion c' and the effective friction angle ϕ' are 12.8 kPa and 33.1° respectively. In this study, the effective soil cohesion $c' = 12.8$ kPa was applied in the case of a well-compacted soil slope while $c' = 0$ was assumed for the worst case scenario as a non-compacted soil condition. Table 5.3 presents the value of shear strength for both cases as the input parameters in the stability analysis during rainfall infiltration.

Table 5.3. Soil shear strength parameters

Type	Parameters	Value	Remark
Effective soil cohesion	c' (kPa)	12.8	Well-compacted soil
		0	Non-compacted soil
Effective friction angle	ϕ' (°)	33.1	-

Factors of safety (FS) were determined for both well-compacted soil condition and non-compacted soil conditions. Figure 5.9 illustrates variation in the FS during the rainfall period of 03-Sept-2008 to 24-Sept-2008. In the well-compacted soil condition, the slope remained stable according to the factor of safety (FS >1.0). For the non-compacted soil condition, slope instability appeared to develop after rainfall intensity exceeded 100 mm/day, in which case the factor of safety was less than 1.0 after 13-Sept-2008. At the beginning of the period of rainfall (before 07-Sept-2008), the factor of safety was almost constant for both conditions which indicated the minor effect of suction to slope stability. From 07-Sept-2008 to 12-Sept-2008, the FS of well-compacted soil gradually decreased, while the FS of non-compacted soil fluctuated. This suggests that factor of safety variability was not affected in the case of greater soil cohesion in the first period of rainfall. However, the distribution of FS with time for well-compacted and the non-compacted soil conditions (Figure 5.9) showed some discrepancy after the highest rainfall intensity which occurred on 12-Sept-2008.

In order to illustrate the influence of heavy rainfall and the failure mechanism of a slope for non-compacted soil, Figure 5.10 presents the distribution of pore water pressure in the soil of the slope and the corresponding failure surface on 13-Sept-2008, as shown in Figure 5.11. As seen in Figure 5.10, the water table (where pore water pressure was zero) reached the upper half of the slope, and pore water pressure increased linearly from the ground surface to the interface between the residual soil and bedrock. The failure surface developed in the region of the lower half of the slope, where the residual soil slope was fully saturated (Figure 5.11). The simulated failure surface implied that the failure mechanism of the slope was a shallow failure which could only occur at the lower depth of 1.0 m in residual soil. The slope would fail as a result of the decrease in the effective stress due to the increase in pore water pressure, while the slope failure might not be affected by a great reduction in soil shear strength (an assumption of $c' = 0$ for non-compacted soil).
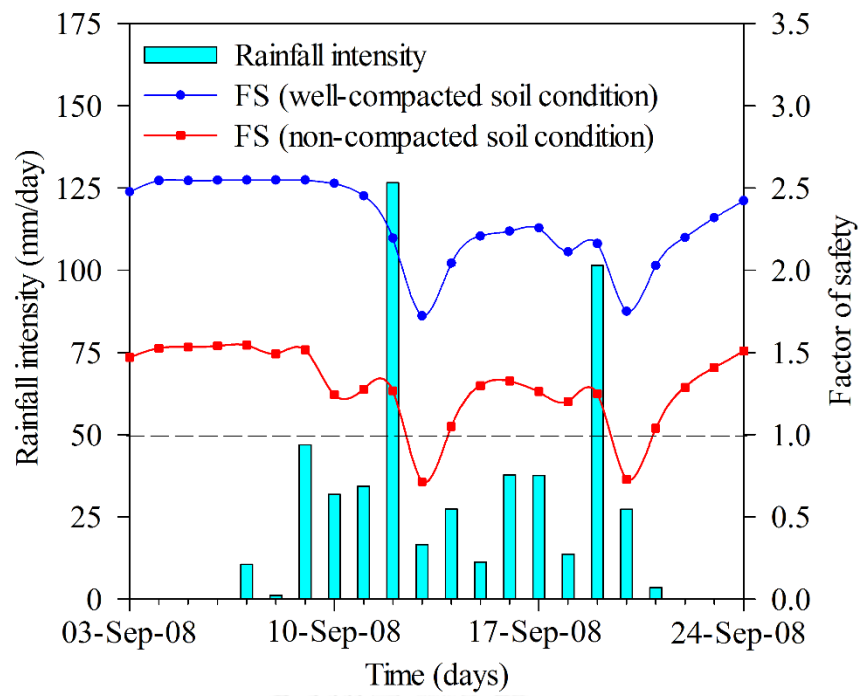
Figure 5.9. Factor of safety variation with time for a soil slope without roots

(unit in kPa)
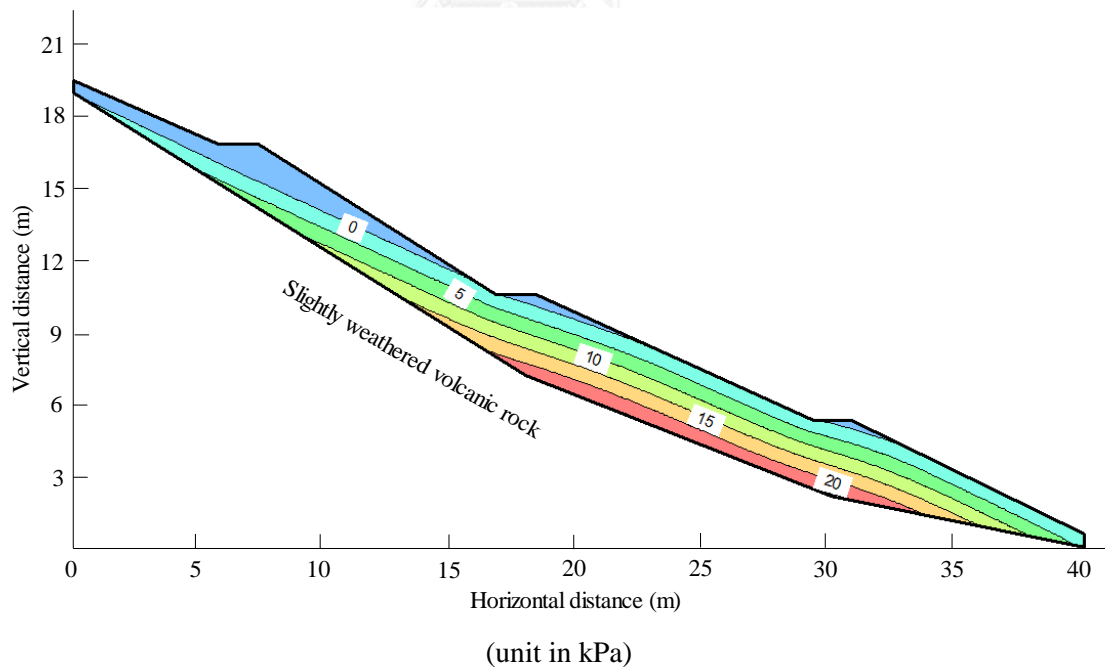
Figure 5.10. The pore water pressure distribution on 13-Sept-2008
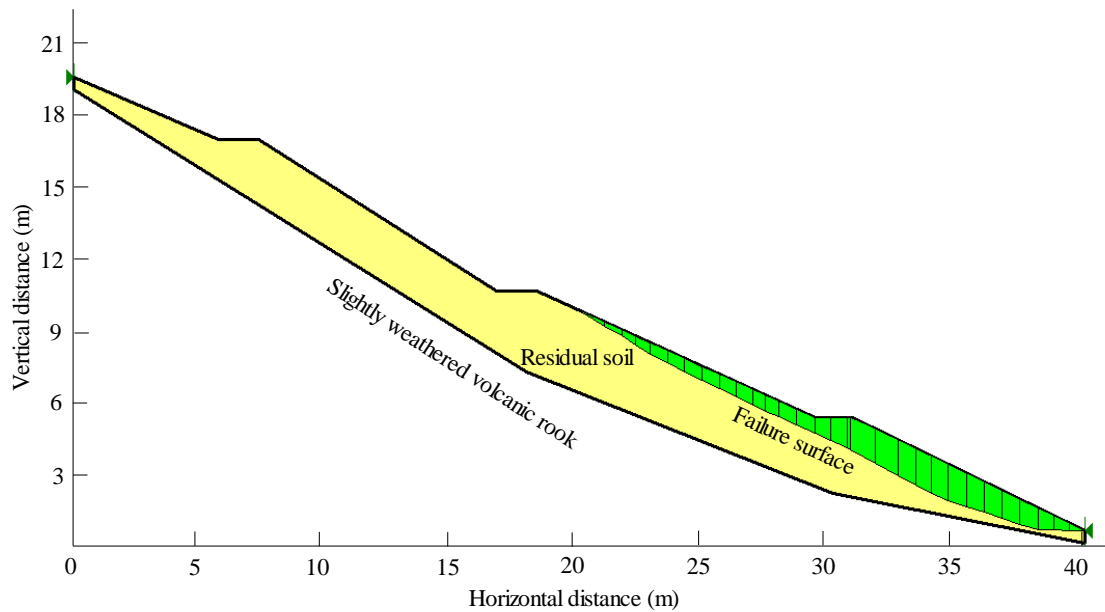
Figure 5.11. Corresponding failure surface for non-compacted soil slope without root cohesion on 13-Sept-2008 (worst case scenario)

5.4.2. Slope with root cohesion

To assess the influence of vegetation on slope stability, the worst case scenario (non-compacted soil condition) was only performed to calculate the factor of safety using equation (5.6) from 03-Sept-2008 to 24-Sept-2008. Vegetation consisting of typical vetiver grass in Thailand was employed as a special case at the Thadan slope. In the literature, the majority of root cohesion vegetation species fall within the range of 1.0-20.0 kPa depending on different environments (O'loughlin, 1974; Kazutoki and Iwamoto, 1986; Abernethy and Rutherfurd, 2001; Simon and Collison, 2002). Furthermore, according to Lynch (1995), the root distribution of some grasses was observed and can be approximately uniform at the shallow depths, while Ji et al. (2012); Leung et al. (2015) have presented evidence that root distribution tends to decrease with depth in deeper zone. In this section, root cohesion was assumed based on the research of Eab et al. (2015) which represented conditions near the ground surface. The average value of root cohesion corresponded to $c_r = 3.0$ kPa and the root cohesion value of $c_r = 6.0$ kPa were used to simulate the effect of variability of root vegetation on slope stability, as shown in Table 5.4. As seen in Figure 5.2, the thickness of the residual soil changed from 0.3 m at the crest and toe of the slope to 2.5 m at the middle of the slope, leading to the assumption of the extended depth of roots which reached the bedrock to

be applied for the whole soil slope in this study. This is because the depth of root systems varies significantly with vegetation species and their growing environments. For trees and shrubs, the root depth was reported in the range of 1.0-3.0 m (Kozlowski, 1971). In North America, the root depth is usually constrained by the bedrock (less than 2.0 m) in many slopes (Schmidt et al., 2001).

Table 5.4. Characteristics of vetiver grass

Type	Parameters	Value
Root cohesion	c_r (kPa)	3.0 and 6.0
Depth of root	l_r (m)	1.8
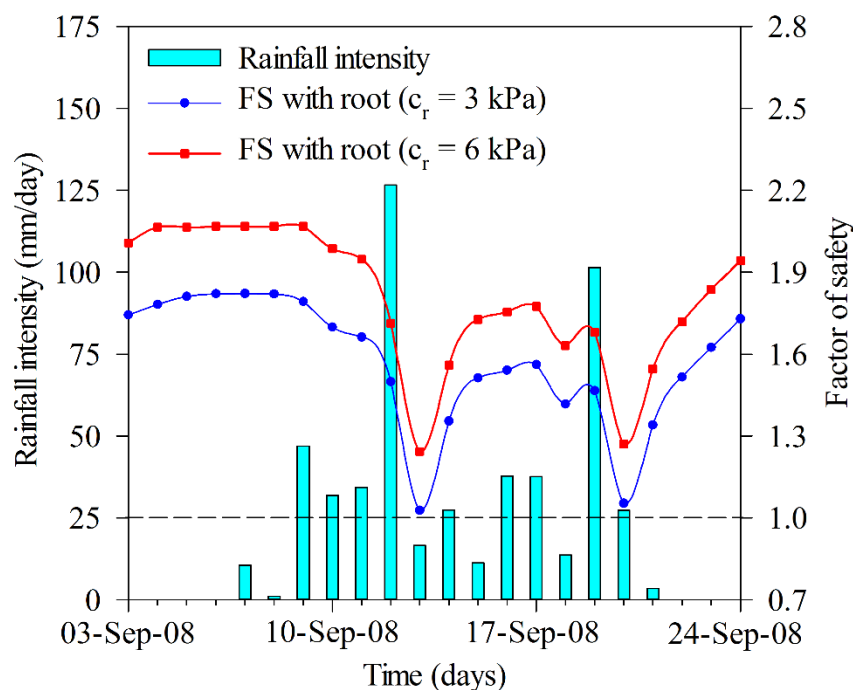
Figure 5.12. Factor of safety varied with time for vegetated slope

Figure 5.12 shows the factor of safety during the rainfall period of 03-Sept-2008 to 24-Sept-2008 considering the contribution of vegetation on both the root cohesion c_r = 3.0 kPa and c_r = 6.0 kPa. It can be seen that the factor of safety of a vegetated slope is higher than that of the worst case scenario without root cohesion (Figure 5.9). In all cases, the factor of safety is always more than 1.0 despite the highest rainfall intensity occurring at 12-Sept-2008. The results in Figure 5.12 also indicate the discrepancy of the distribution of FS considering the smaller value of root cohesion and that of FS considering the greater value of root cohesion. In the case of root cohesion c_r = 3.0 kPa,

the lowest FS is 1.03 (45% increment from the case without root cohesion) while the lowest FS is 1.24 (75% increment from the case without root cohesion) for case of root cohesion $c_r = 6.0$ kPa. This finding suggests that the uniform distribution of roots can effectively increase the stability of a slope during heavy rainfall. Thus, the contribution of vegetation to stabilise slopes can be readily seen as the slope would not fail even under the worst case scenario if it was rebuilt and grown with vegetation.

5.5. Probabilistic method for analysis of slope stability of the Thadan slope

5.5.1. Domain of spatial variability root cohesion

In order to simulate the effect of the spatial variability of root cohesion on a probabilistic analysis, a typical finite element model of the Thadan slope was constructed, as shown in Figure 5.13. The majority of elements are square and the elements adjacent to the bottom model are generated into triangles. In this study, element size is mainly 0.5 m in length for both the distance in a horizontal direction and the distance in a vertical direction. However, the length of a few elements can be less than or more than 0.5 m in length because of the complex geometry of the slope. In Figure 5.13, the finite element mesh consists of 380 elements, each element being then assigned a value of generated root cohesion from a random field model which is carried out in the following section.
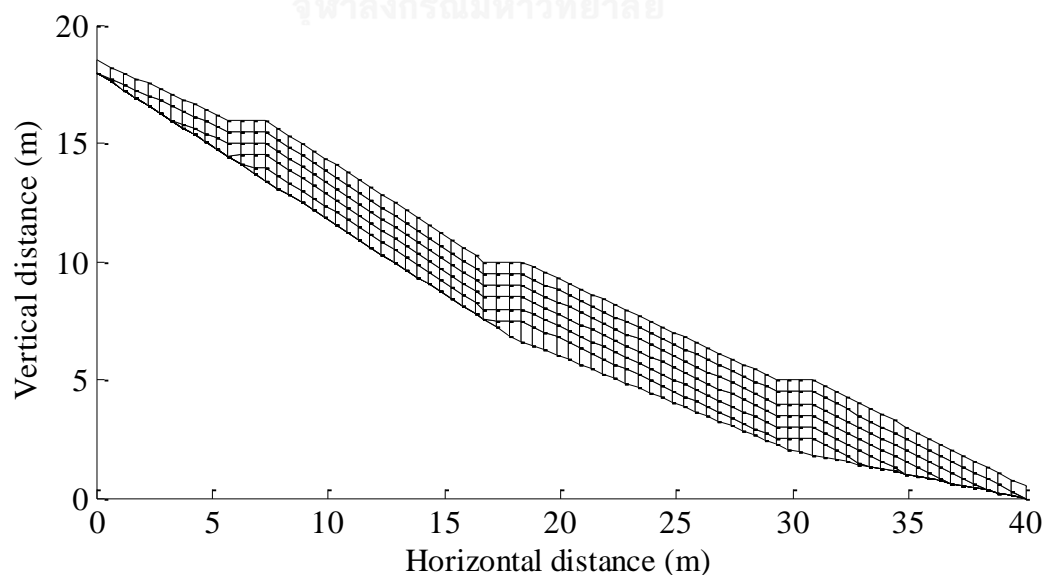
Figure 5.13. A typical finite element model of the Thadan slope considering the effect of spatial variability of root cohesion

5.5.2. Random field generation of root cohesion

Before the random field of root cohesion is generated, a two sided spectral density function should be defined in a chosen domain of root cohesion, as presented in equation (5.7). A numerical integration is applied to solve equation (5.7) at every point with an interval frequency (f_i, f_j) in the horizontal and vertical dimension, respectively.

$$G(f_i, f_j) = \frac{4}{\pi} \int_0^x \int_0^y \beta(\tau_x, \tau_y) \cos(2\pi f_i \tau_x + 2\pi f_j \tau_y) dx dy \qquad (5.7)$$

where x, y are horizontal and vertical distance, respectively; τ_x and τ_y are the distance any two points in horizontal and vertical dimensions, $\beta(\tau_x, \tau_y)$ is the correlation function as seen in equation (2.23).

A two-dimensional random field of standard normal distribution can also be simulated using a two sided spectral density function in two dimensions, as given:

$$X(x_i, y_j) = \sum_{i=1}^n \sum_{j=1}^m R_{ij} \left[A_{ij} \sin(2\pi f_i \tau_x + 2\pi f_j \tau_y) + B_{ij} \cos(2\pi f_i \tau_x + 2\pi f_j \tau_y) \right] \qquad (5.8)$$

in which $R_{ij} = \sqrt{G(f_i, f_j)\tau_x \tau_y}$ and $f_i = (2i-1)\tau_x / 2$, $f_j = (2j-1)\tau_y / 2$, where $G(f_i, f_j)$ must be taken in the manner of the positive τ_x, τ_y in order to R_{ij} which is always the meaning. This is done because the spectral density function is symmetrical about the original point.

In a random field model, the value of root cohesion assigned to each element is itself a random variable which can be correlated to one another by controlling the autocorrelation coefficient. Because the size of each element might be different within the domain, the mean value assigned for each element is affected by local averaging. For a finite element of side length T_x and T_y, the variance reduction factor due to local averaging using numerical integral solution to solve equation (2.24) (Fenton and Griffiths, 2008) is given by:

$$\gamma(T_x, T_y) = \frac{l_x^2 l_y^2}{4T_x^2 T_y^2} \left[\frac{2T_x}{l_x} + exp\left(-\frac{2T_x}{l_x} \right) - 1 \right] \left[\frac{2T_y}{l_y} + exp\left(-\frac{2T_y}{l_y} \right) - 1 \right] \qquad (5.9)$$

where *x,* and *y* denote the coordinates of the centroid of each element. It is clear that variance reduction significantly decreases when element size increases. Therefore, the influence of spatial variability of root cohesion might not respond to the manner of a larger size element known as traditional probability analysis. In this study, the root cohesion can be modeled as a lognormal distribution due to the value of root cohesion always being positive. The random field of root cohesion is given by:

$$c_r(x_i, y_i) = exp\left[\mu_{c_r} + \sigma_{c_r} \gamma(T_x, T_y) X(x_i, y_i) \right] \qquad (5.10)$$

A typical random field of root cohesion for the Thadan slope considering the effect of vegetation is shown in Figure 5.14. Because the slope has 380 elements, it contains 380 random variables. The random variables can be correlated to one another by controlling the spatial autocorrelation length, as described in equation (2.23). Figure 5.14 (a) and (c) show random fields of root cohesion at mean values $c_r = 3$ kPa and $c_r = 6$ kPa, respectively corresponding to the same correlation length $l_x = l_y = 0.25$ m. For small autocorrelation lengths, variability of uniform distribution of root cohesion appeared at almost all elements. With a high correlation length, strong root reinforcement only occurred at specific regions, while weak root reinforcement existed at others, as depicted in Figure 5.14 (b) and (d). It is clear that the spatial variability of root cohesion can lead to uniform variability of root soil for the whole slope, the strong root soil occurring specific regions, and weak root soil occurring at other regions causing a conservative estimate of failure probability. Thus, vegetated slope stability should be accounted for in reliability analysis.
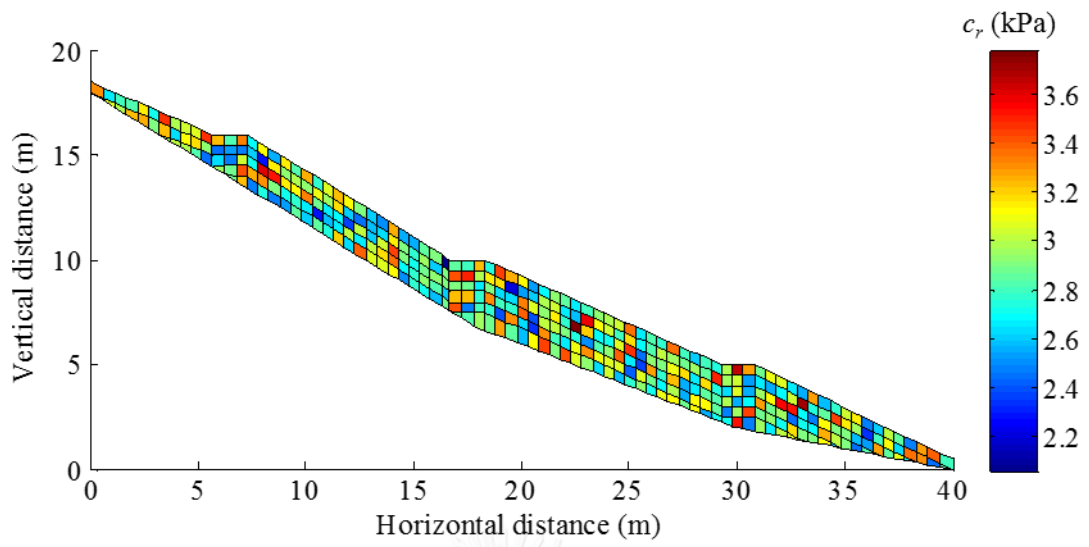
a) $l_x = l_y = 0.25$ m, cov $= 0.25$, mean $= 3.0$ kPa
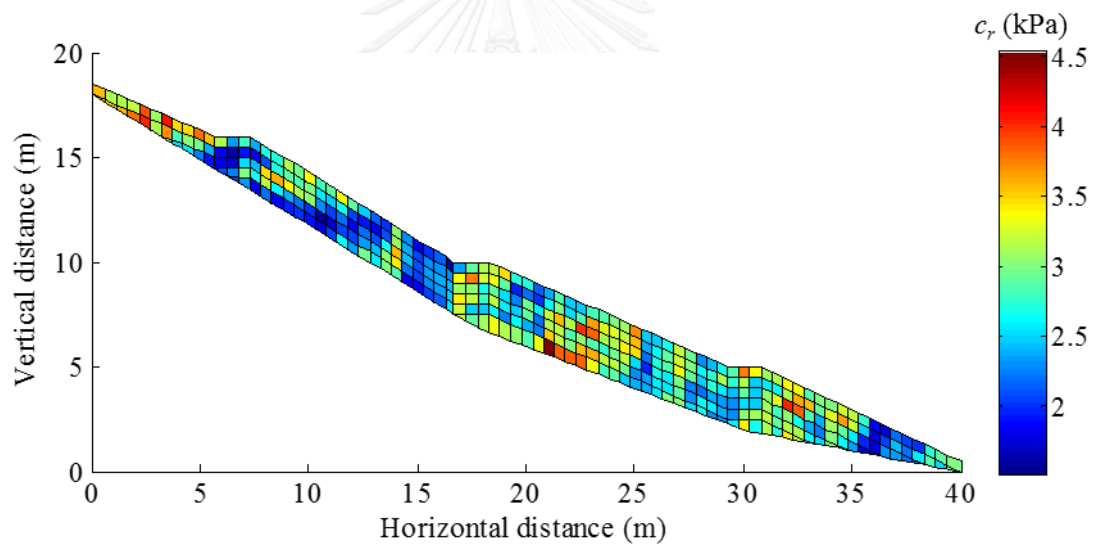
b) $l_x = l_y = 2.0$ m, cov $= 0.25$, mean $= 3.0$ kPa
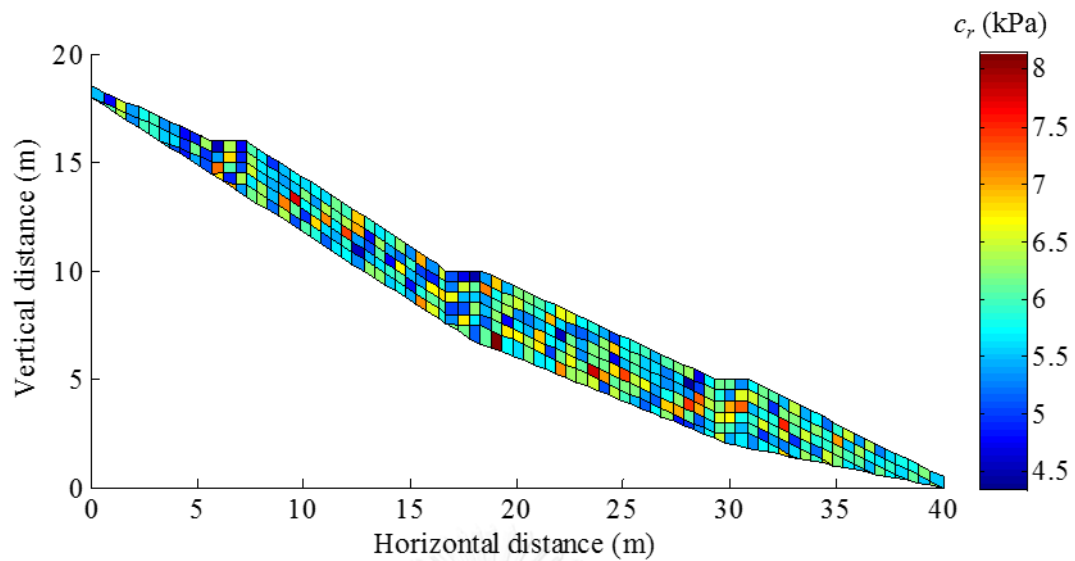
c) $l_x = l_y = 0.25$ m, cov = 0.5, mean = 6.0 kPa
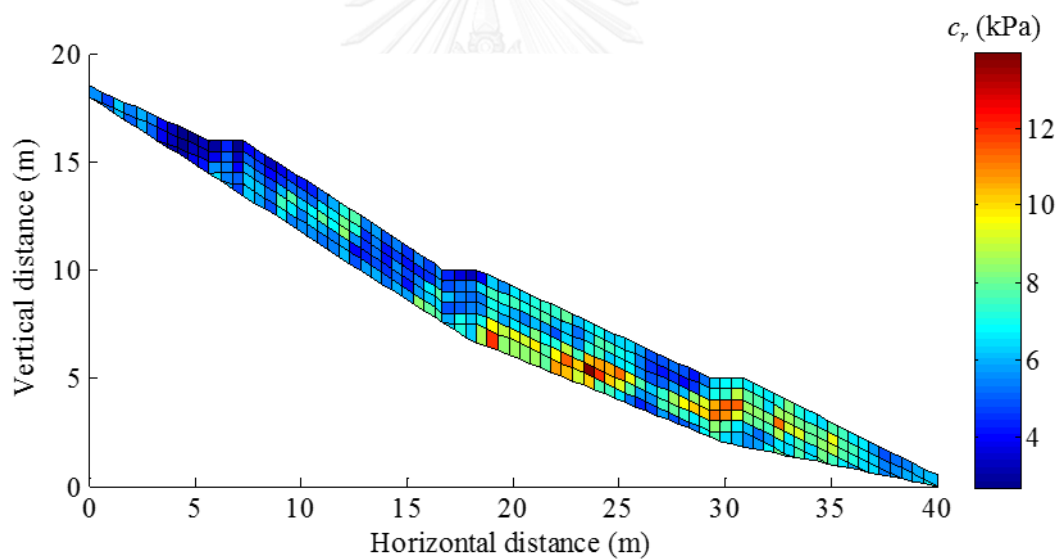
d) $l_x = l_y = 2.0$ m, cov = 0.5, mean = 6.0 kPa

Figure 5.14. Typical random field of root cohesion

Figure 5.15 shows tow typical critical surface at the two different autocorrelation lengths corresponding to random fields of root cohesion in Figure 5.14 (c) and (d). A few parts of critical surface in Figure 5.14 (c) did not occur on bed rock while critical surface in Figure 5.14 (d) almost located on bed rock. In addition, the FS was calculated using Bishop's simplified method indicated that the FS considering a smaller autocorrelation length (FS=1.013) was less than that considering a greater

autocorrelation length (FS=1.131). It is clear that the spatial variability of root cohesion significantly effects on slope stability and distribution of failure mechanism as well.
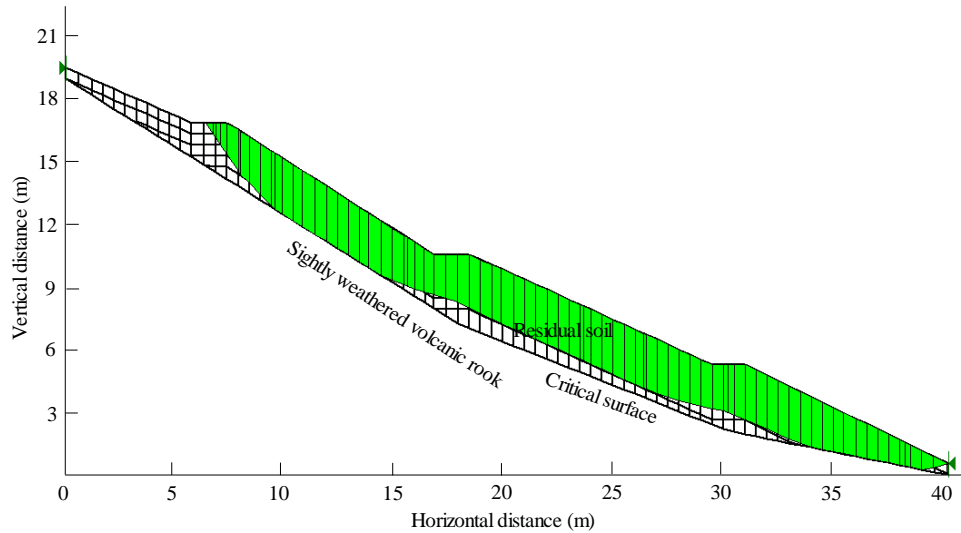
a) $l_x = l_y = 0.25$ m, cov = 0.5, mean = 6.0 kPa; FS = 1.013
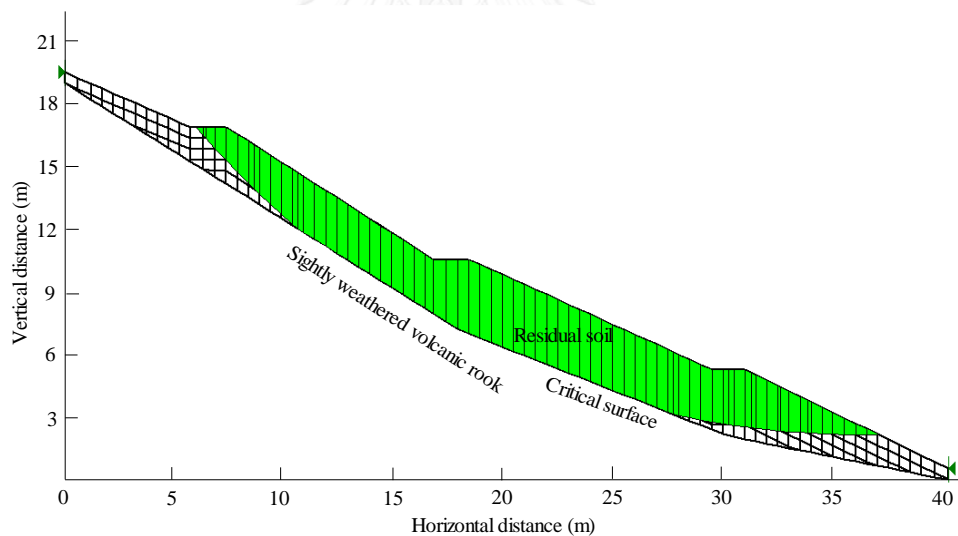
b) $l_x = l_y = 2.0$ m, cov = 0.5, mean = 6.0 kPa; FS = 1.131

Figure 5.15. Typical critical surface at two different autocorrelation lengths ($l_x = l_y = 0.25$ m and $l_x = l_y = 2.0$ m)

5.5.3. Procedure of approximated failure probability

A procedure to approximate failure probability considering the effect of spatial variability of root cohesion is proposed in this section, as shown in Figure 5.16. This procedure includes the following steps:

(1) Creation of a finite element model of probabilistic analysis of the vegetated slope with the same hydrological parameters of seepage analysis for all elements using the SEEP/W module. Soil suction (pore water pressure) and volumetric moisture content are calculated according to the corresponding model in order to estimate slope stability. Then, a vegetated slope model which has the same structure is assigned the mean value of root cohesion for all elements using the SLOPE/W module. Next, the SLOPE/W module runs to define the factor of safety (FS) and create an "FS" input file. The "FS" input file contains all the necessary information of the SEEP/W and SLOPE/W modules (Appendix B1) which can be modified according to the requirements of this study.

(2) Identification of the statistical characteristics of root cohesion such as the mean (μ), coefficient of variance (cov), and autocorrelation length (l_x and l_y). After determination of the T_x and T_y for each element, n random fields of root cohesion are generated in two dimensions using equation (5.10). It is noted that n is a number in the Monte Carlo simulation and each random field includes all elements of the domain that must have different values of root cohesion.

(3) A matlab program is used to replace the mean value of root cohesion in step (1) with the corresponding value of root cohesion which is generated in step (2). Because the Monte Carlo simulation of n realizations was performed n new "FS" input files are also generated in this step. All new "FS" input files have the same structure except the value of root cohesion at each element.

(4) Running the SLOPE/W module with each new "FS" input file generated in step (3) to calculate the factor of safety. Such a process is executed automatically by a generated "Run_MCS" file, as shown in Appendix B2, and the result is also automatically saved under "FS" output files, as shown in Appendix B3. This process will produce n different "FS" output files which contain n different factors of safety, respectively.

(5) n different factors of safety are extracted from n corresponding "FS" output files and the failure probability is approximated by equation (3.11).

```
                              ( START )
                                  │
                                  ▼
              ┌──────────────────────────────────────┐
              │  Create a finite element model using  │
              │              SEEP/W                    │
              └──────────────────────────────────────┘
                                  │
                                  ▼
              ┌──────────────────────────────────────┐
              │     Create the "FS" input file from    │
              │   deterministic analysis using SLOPE/W │
              └──────────────────────────────────────┘
                                  │
                                  ▼
```

Identify statistical charateristic of c_r

Input:
i) Mean value (μ)
ii) Coefficients of variance (cov)
iii) Autocorrelation length (l_x and l_y)

$i = 0$
n = sample size

Simulate spatial variability of c_r using random field model and MCS

$i = i+1$

$i < n$

Generate new "FS" input file for each realization of random field of c_r

Run SLOPE/W with new "FS" input file

Extract factor of safety from calculated result of new "FS" input file

NO

$i = n$

YES

Approximate failure probability using equation (3.11)

(END)

Figure 5.16. Flowchart of approximated failure probability

5.5.4. Failure probability considering the effect of spatial variability of root cohesion

For a given set of input root cohesion data (mean, coefficient of covariance, and autocorrelation length), a Monte Carlo simulation is performed. This means that the slope stability analysis is repeated many times until the calculated failure probability reaches a point of convergence. Each realization of the Monte Carlo simulation process differs in the location at which the strong and weak zones are situated. For example, in the first realization, the critical surface may be situated in the weak zone which causes slope failure, whereas in another realization, the critical surface may be located at the strong zone where the slope remains stable. In this section, probabilistic analysis is only approximated for non-compacted soil conditions (worst case scenario) to dominate the effect of vegetation. Because root cohesion displays strong variability in distance or space, as mentioned in Chapters 1 and 2, an assumption of range cov of 0.5 - 4.0 is specified for root cohesion. The mean value of root cohesion which was measured near ground surface (Eab et al., 2015) is implemented in this case, while the autocorrelation length varies from 0.25 to 2.0 m, as presented in Table 5.5. The failure probability of a vegetated slope is calculated at the critical failure surface corresponding to the minimum FS of the deterministic analysis (13-Sept-2008).

Table 5.5. Statistical characteristic of root cohesion

Root cohesion	Mean value (kPa)	cov	l_x and l_y (m)
c_r	6.0	0.5 - 4.0	0.25 - 2.0

Since calculation of a complex problem (i.e. Thadan slope) will consume time, the number of realizations of the Monte Carlo simulation should be accurately defined as approximated failure probability. Figure 5.17 shows the convergence of the estimated probability of failure at the different cov of root cohesion and autocorrelation length which indicate that the failure probability can be converged when n realizations of MCS exceed 200. In this study, 500 sets of the random fields of c_r were used as input root cohesion data for probabilistic analysis on vegetated slope stability.
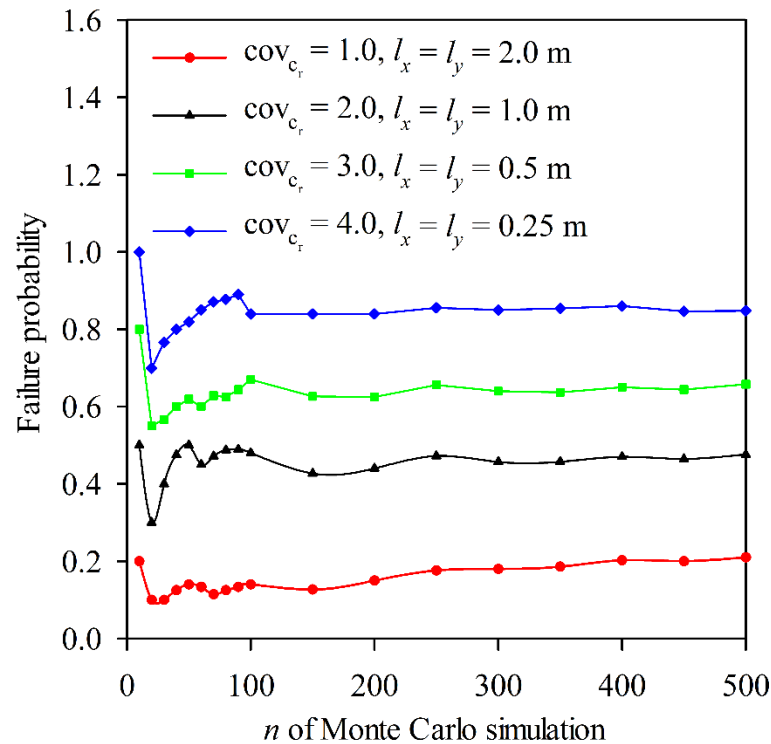
Figure 5.17. Influence of the MCS on convergent failure probability

5.5.4.1. Effect of autocorrelation length (l_x, l_y) and coefficient of variance (cov)

Figure 5.18 shows the failure probability as a function of autocorrelation length (l_x, l_y) for a range of input coefficients of variance (cov), with the mean of root cohesion $c_r = 6.0$ kPa. The results indicate that the failure probability increased with increasing cov of root cohesion. The slope considering lesser values of autocorrelation length had a smaller failure probability in which the cov of root cohesion was less than 2.0 while the failure probability for cases with the smaller values of autocorrelation length was greater than that with the larger values of autocorrelation length, in which the cov of root cohesion exceeded 2.0. This figure clearly shows the full influence of spatial variability of root cohesion in the range of autocorrelation length $0.25 \leq l_x$, $l_y \leq 2.0$ m. It should be emphasized that all curves cross over at the failure probability of approximately 0.47 occurring at cov = 2.0. This is because the cumulative probability of FS for all autocorrelation lengths is equal to 0.47 at the corresponding safety factor of FS = 1.0, as shown in Figure 5.19. Therefore, a cov = 2.0 can be seen as a critical cov of root cohesion causing complete slope failure in this analysis. This can be compared with previous research of Fenton and Griffiths (2008), in which the failure

probability was always 0.5 since they only focused on a hypothetical slope with the same element size within the entire slope.
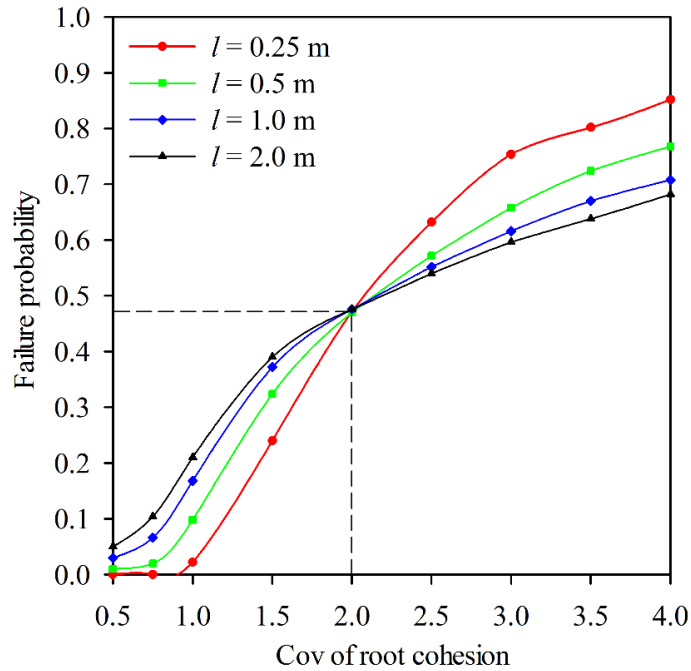
Figure 5.18. The effect of spatial variability of root cohesion on failure probability
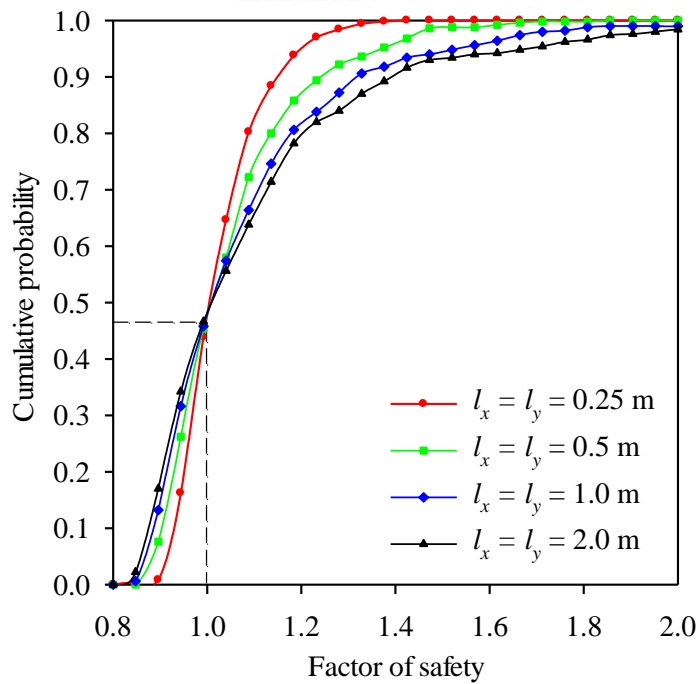
Figure 5.19. Cumulative probability of FS at $\text{cov}_{c_r} = 2.0$

In the previous assessment, failure probability was approximated only focusing on an isotropic random field of root cohesion ($l_x = l_y$). One might want to identify which anisotropic random field of root cohesion ($l_x \neq l_y$) contributes the effect of calculated failure probability. Figure 5.20 illustrates the failure probability considering the difference between the horizontal autocorrelation length and vertical autocorrelation length. These results indicate that failure probability with an anisotropic random field was larger than that with an isotropic random field in which the cov of root cohesion is less than the critical value. On the other hand, the cov of root cohesion is more than critical value failure probability with an anisotropic random field was smaller than that with an isotropic random field. In addition, the anisotropic random field did not have the greatest influence on failure probability for both ratios of l_x / l_y and l_y / l_x. It is clear that the spatial variability of root cohesion in horizontal and vertical directions had significant effect leading to likelihood of overestimating or underestimating failure probability in slope stability analysis.
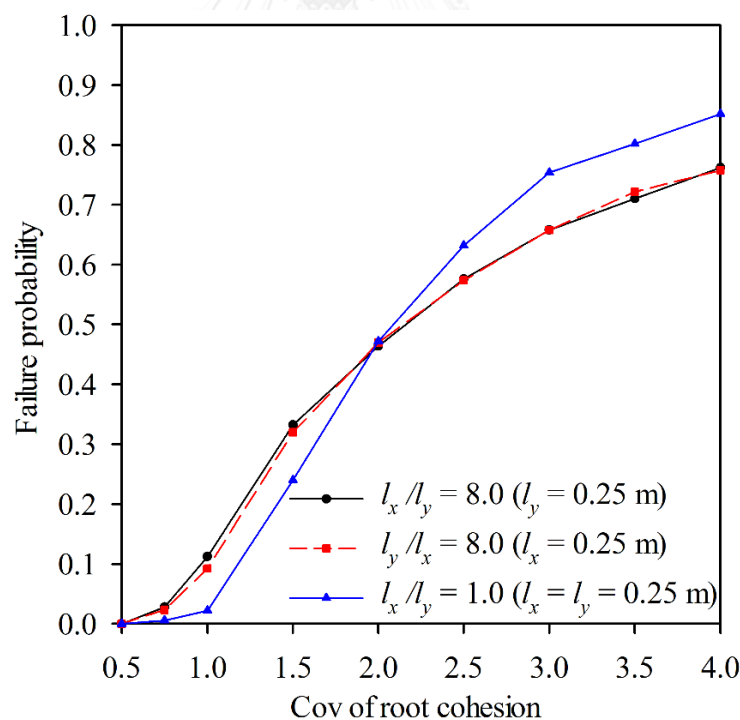
Figure 5.20. Effect of anisotropic random field on failure probability

5.5.4.2. Effect of a finite element mesh on failure probability

In order to simulate the effect of finite element mesh on failure probability the major length of elements in the horizontal dimension was maintained with no change ($\tau_x = 0.5$ m), while the major length of elements in the vertical dimension of $\tau_y = 0.25$ m was specified which could have emphasized the contribution of root cohesion with depth. 962 elements were generated in this case. Figure 5.21 (a) shows the variation of failure probability with the coefficient of variation of c_r for the two differences of typical finite elements at the autocorrelation length $l_x = l_y = 0.5$ m. The failure probability, ignoring spatial variability of root cohesion (random variable l_x, $l_y \to \infty$), is also drawn in this figure to evaluate the effect of a finite element mesh. With an increase of cov, the results indicated that there were two crossover points between the curves associated with the random field ($T_x = T_y = 0.5$ m and $T_x = 0.5$ m, $T_y = 0.25$ m) and random variable (l_x, $l_y \to \infty$), which gave a critical value of cov_{c_r}. When the cov_{c_r} exceeded the critical values, considering the random variable in c_r would lead to an underestimate of the failure probability. Otherwise, it would be an overestimate of the failure probability if the corresponding cov_{c_r} was less than the critical values. Such findings are consistent with the observations reported in Fenton and Griffiths (2008). It is clear that the critical value of $\text{cov}_{c_r} = 1.75$; 2.4 and the failure probability $P_f = 0.47$; 0.56 increases with increasing finite element mesh, respectively. Figure 5.21 (b) shows the failure probability which was approximated using a random field and random variable at two critical values of $\text{cov}_{c_r} = 1.75$ and 2.4 corresponding to an element size of $T_x = T_y = 0.5$ m and $T_x = 0.5$ m, $T_y = 0.25$ m, respectively. It is clear that a conservative estimation of failure probability fully depended on the covariance coefficient and autocorrelation length. With a smaller element size, failure probability was overestimated when autocorrelation length increased. Otherwise, failure probability was underestimated with the larger element size. The critical values of cov_{c_r} also increased with increasing element size. In addition, to compare the effect of two differences of typical finite element on distribution of FS, a series of factors of safety were calculated at $\text{cov}_{c_r} = 2.0$ with an autocorrelation length $l_x = l_y = 0.5$ m, as shown in Figure 5.22. Figure 5.22 (a) shows that the probability distribution curve of the FS considering a finite element mesh with $T_x = T_y = 0.5$ was narrower than that curve of

the FS considering a finite element mesh with $T_x = 0.5$ m, $T_y = 0.25$ m. This can be explained by the fact that the smaller sized element had a greater influence by variance reduction (equation (5.9)) which caused an increase in the range of FS. Figure 5.22 (b) shows the cumulative probability of FS for two typical finite element meshes which indicate that the failure probability of the slope increases with decreasing finite element mesh, equal to 0.47 and 0.53 corresponding to $T_x = T_y = 0.5$ m and $T_x = 0.5$ m, $T_y = 0.25$, respectively. It can be observed that ignoring the finite element mesh (considering only the random variable for the whole slope) would lead to an un-conservative estimate of the failure probability of the slope if factor of safety was below 1.0. These results are in fair agreement with the research of Cho (2007) and Griffiths et al. (2011).
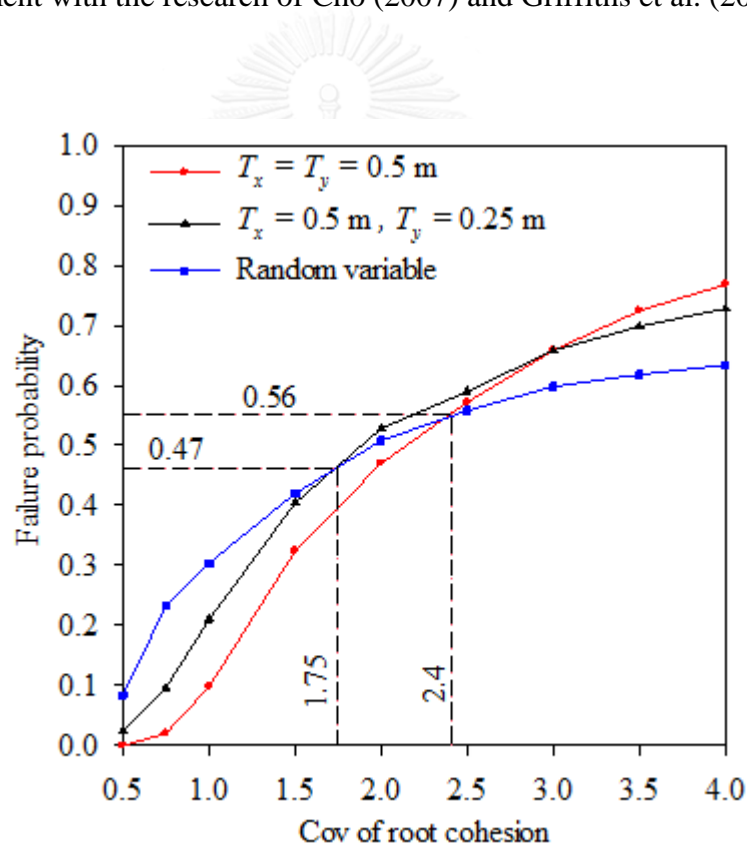
a) Effect of variation of cov of root cohesion at $l_x = l_y = 0.5$ m
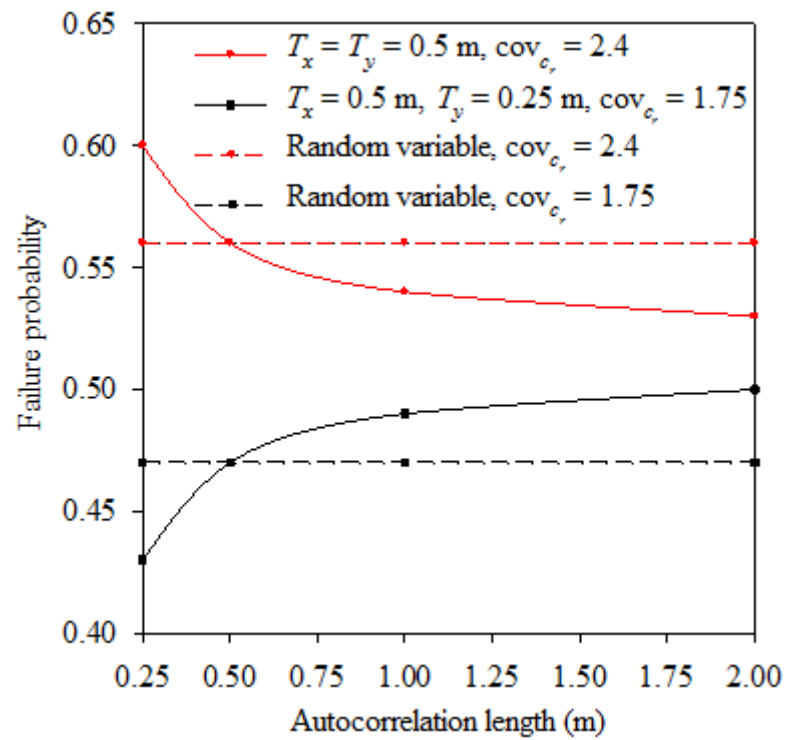
b) Effect of variation of autocorrelation length at critical values of cov_{c_r}

Figure 5.21. Effect of finite element mesh on failure probability
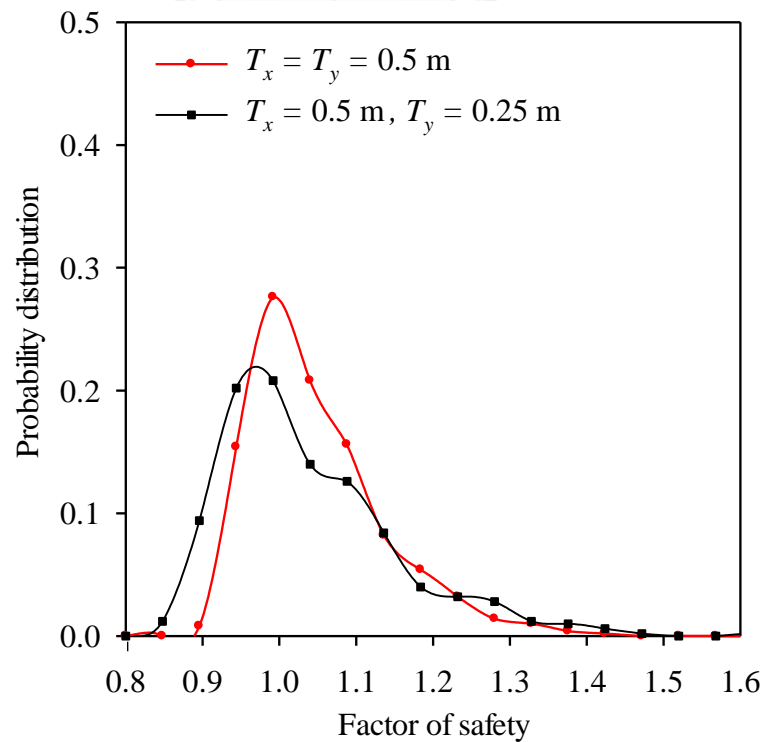
a) Probability distribution of FS
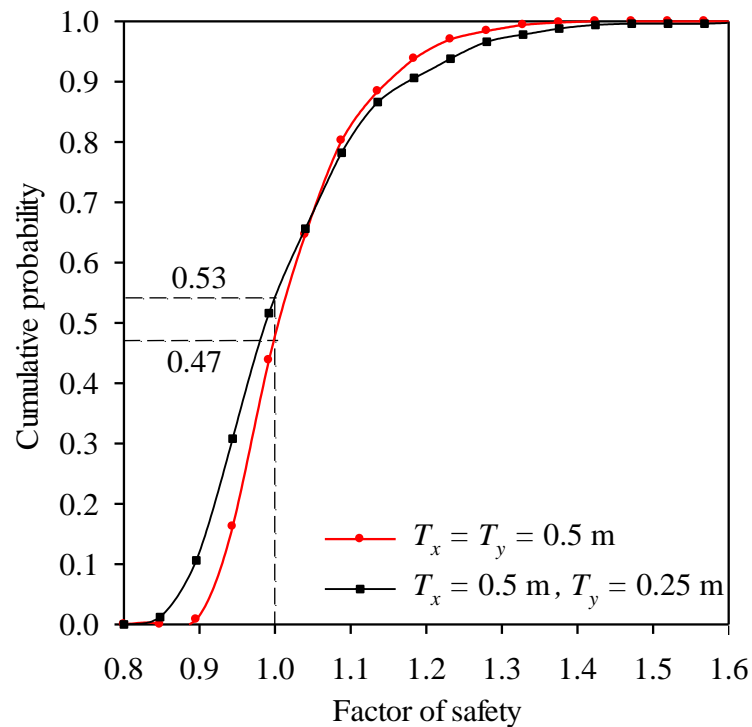
b) Cumulative probability of FS

Figure 5.22. Comparison of distribution of FS at two different typical finite elements
($\mathrm{cov}_{c_r} = 2.0$ and $l_x = l_y = 0.5$ m)

5.5.5. Effects of root distribution on failure probability

In order to simulate the effect of root distribution on failure probability, a stationary random field with the mean value corresponding to the average value of root cohesion was used for the uniform distribution of roots (Figure 5.23 (a)). While a non-stationary random field with the mean values corresponding to values calculated by the linear function of root cohesion (decrease with depth) was used for the triangular distribution of roots (Figure 5.23 (b)). According to Vergani et al. (2012), cov of root tensile strength of seven tree species (spruce fir, European larch, European beech, sweet chestnut, maple, ash, and hornbeam) was between 0.25 and 1.22. In addition, root cohesion was a linear function of root tensile strength; thus, cov of root cohesion can be set as the similar value of cov of root tensile strength (Fenton and Griffiths, 2008). The statistical characteristics of root cohesion are presented in
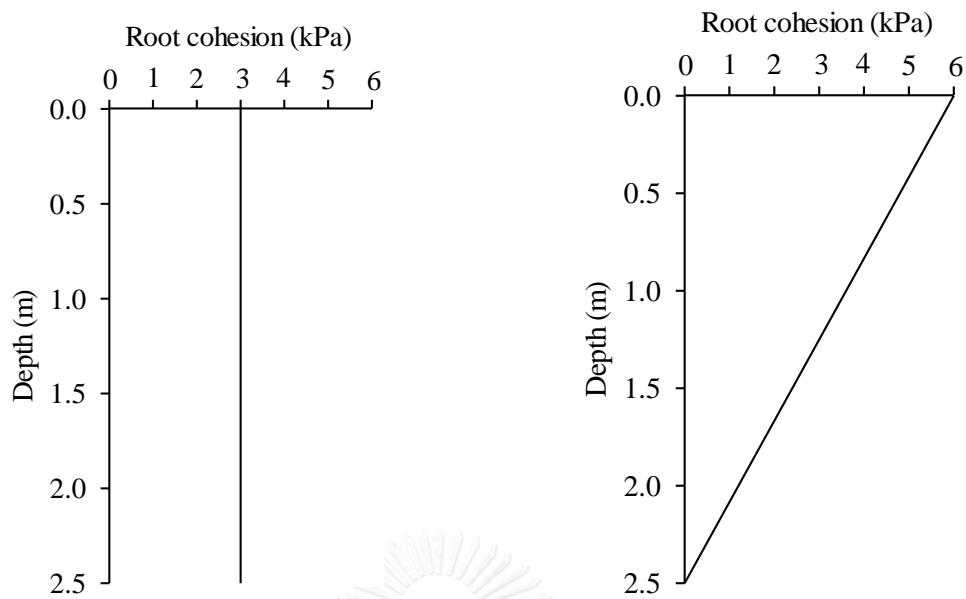
a) Case 1 (Uniform distribution of roots)   b) Case 2 (Triangular distribution of roots)

Figure 5.23. Distribution model assumption of root cohesion

Table 5.6. Statistical characteristic of root cohesion in the two different distribution

Type	Parameters	Statistical characteristic			Root distribution
		Mean	cov	l_x and l_y (m)	
Root cohesion	c_r (kPa)	3.0 $6(1-z/z_r)$	0.1 - 1.0	0.25 - 2.0	Uniform Triangular

Figure 5.24 (a) and (b) indicate that the critical cov of root cohesion considering the uniform distribution of roots and triangular distribution of roots were 0.45 and 0.32, respectively. This is because the cumulative probability of FS for all autocorrelation lengths and cov = 0.45, 0.32 is also equal to 0.46 at the corresponding safety factor of FS = 1.0, as shown in Figure 5.25 causing complete slope failure in this analysis.
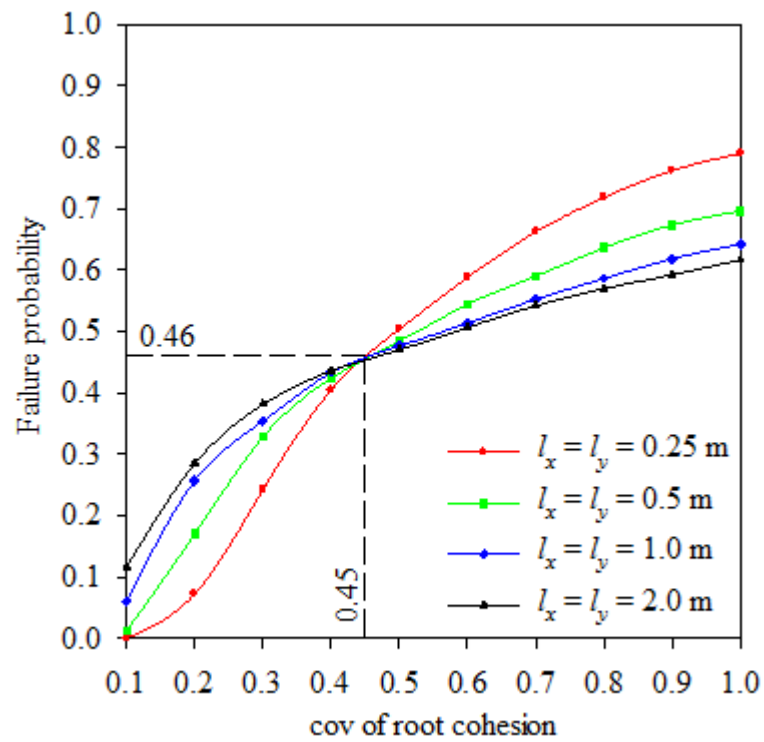
a) Uniform distribution of root
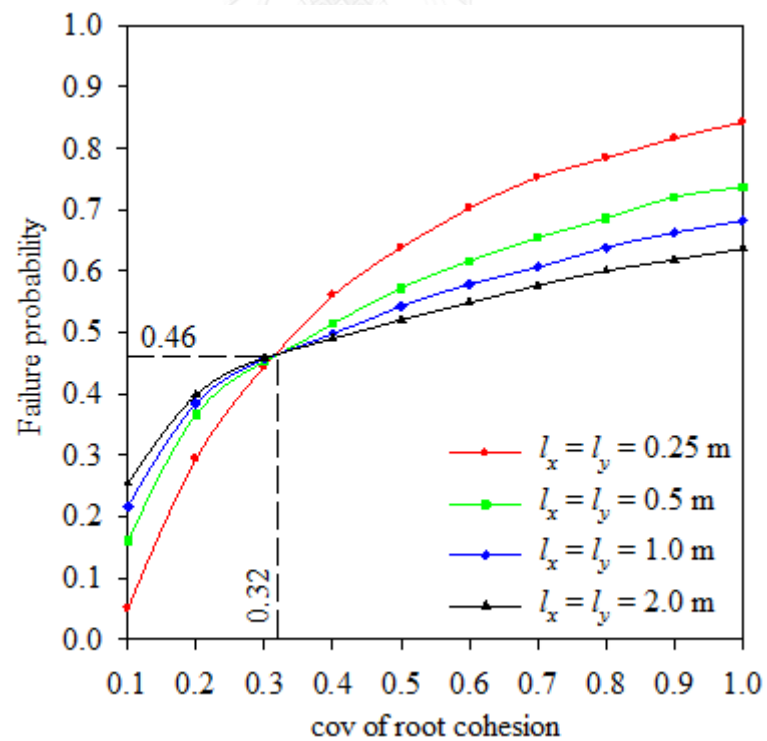
b) Triangular distribution of root

Figure 5.24. The effect of root distribution respond to critical cov
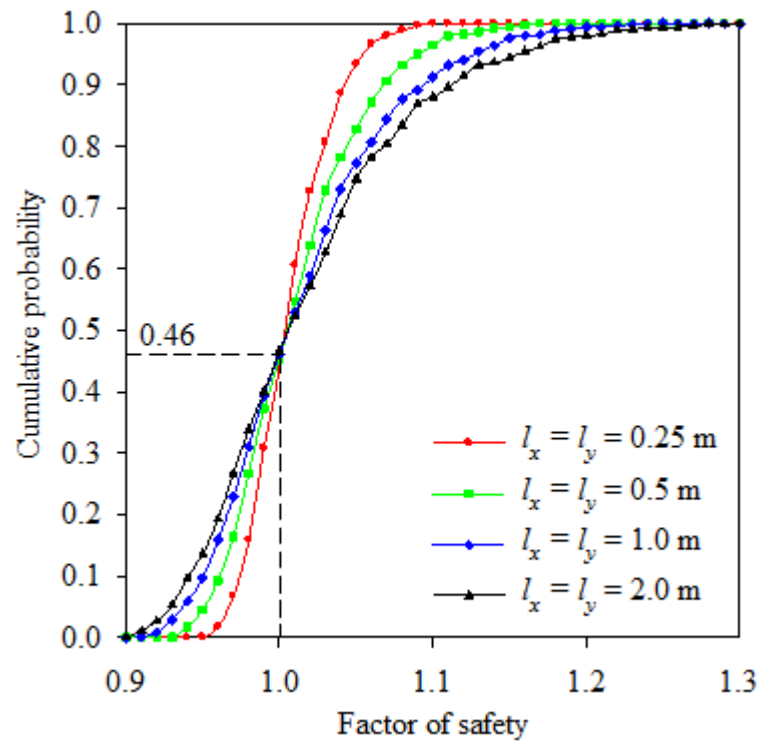
a) Uniform distribution of root ($\text{cov}_{c_r} = 0.45$)
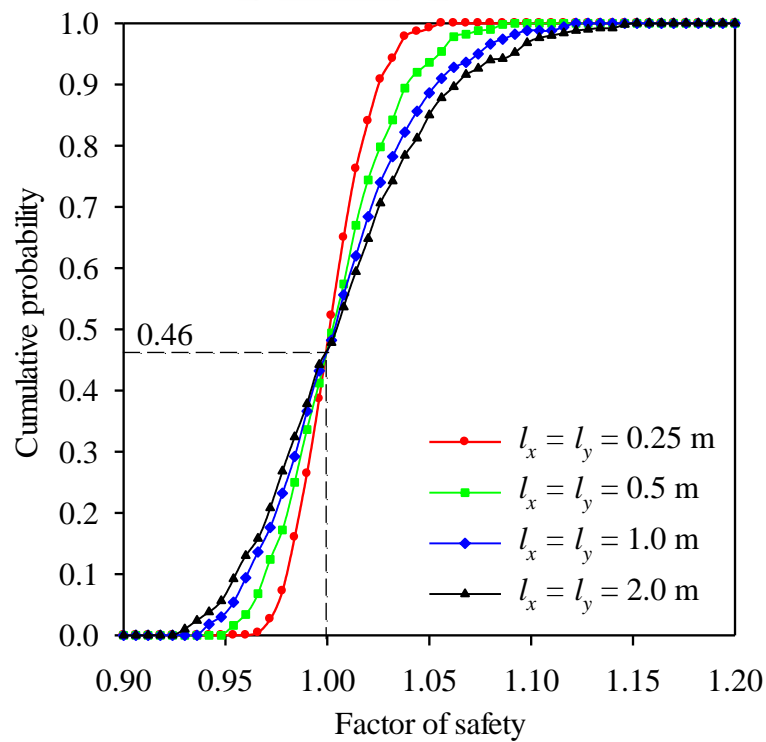
b) Triangular distribution of root ($\text{cov}_{c_r} = 0.32$)

Figure 5.25. Cumulative probability of FS at critical cov of root cohesion

Figure 5.26 the typical random field of root cohesions corresponding to the autocorrelation length $l_x = l_y = 0.25$ m and the critical cov were specified. For the uniform distribution of roots, the higher value of root cohesion could appear at a shallow and greater depth (Figure 5.26 (a)). This observation is explained by the assumption that mean value of root cohesion was calculated from the average value of root cohesion, which seem to be not realistic. With the triangular distribution of roots, variability of the stronger root reinforcement only occurred at upper depths while variability of the weaker root reinforcement existed at lower depths (Figure 5.26 (b)). This is because a phenomena of the triangular distribution of roots made root cohesion increasing with depth, which was known as a more actual condition. Thus, the effect of spatial variability on root distribution may cause a conservative calculation of the FS or the failure probability. As seen in Figure 5.27, the corresponding FS considering the uniform distribution of roots (Figure 5.27 (a)) was more than that considering the triangular distribution of roots (Figure 5.27 (b)). This can explain that some parts of the critical surface crossed the higher value of root cohesion in the uniform distribution of roots. On the contrary most of the critical surface located on the smaller value of root cohesion in the triangular distribution of roots causing decrease in FS.
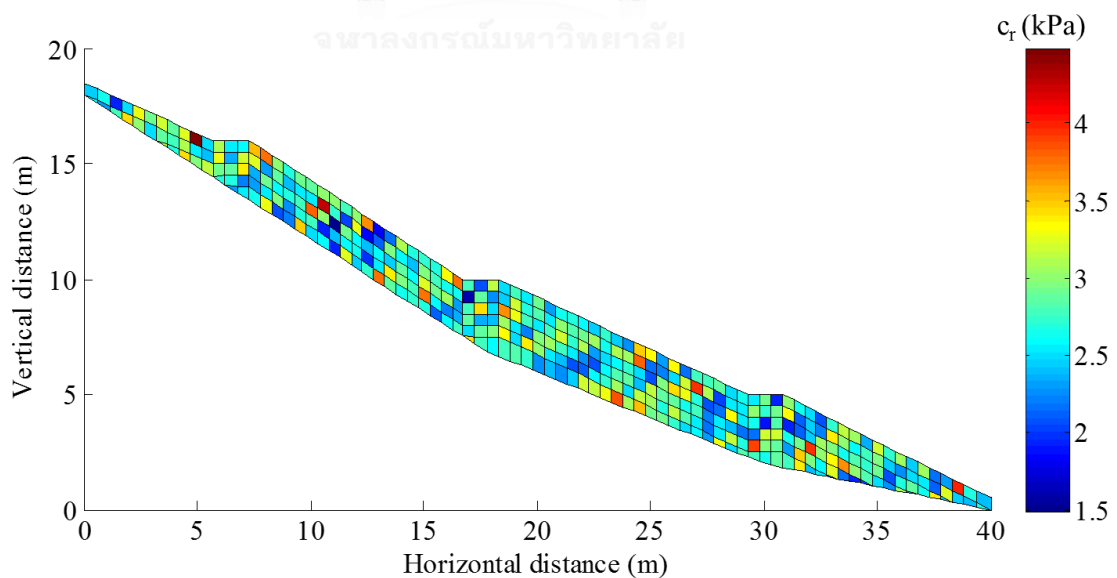
a) Uniform distribution of root ($l_x = l_y = 0.25$ m; $\text{cov}_{c_r} = 0.45$)
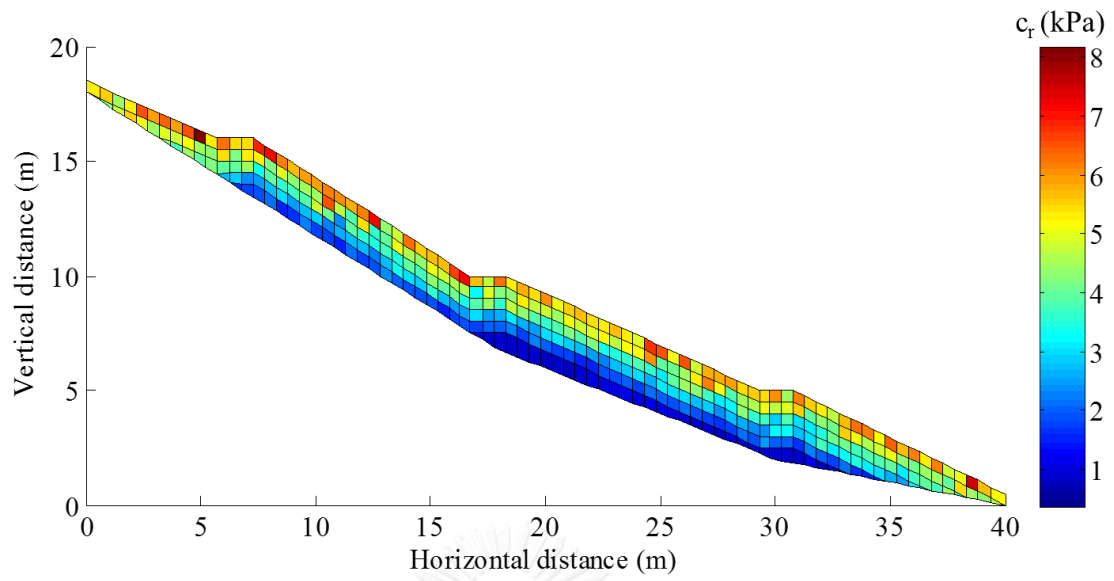
a) Triangular distribution of root ($l_x = l_y = 0.25$ m; $\text{cov}_{c_r} = 0.32$)

Figure 5.26. Typical random field of root cohesion at critical cov_{c_r}
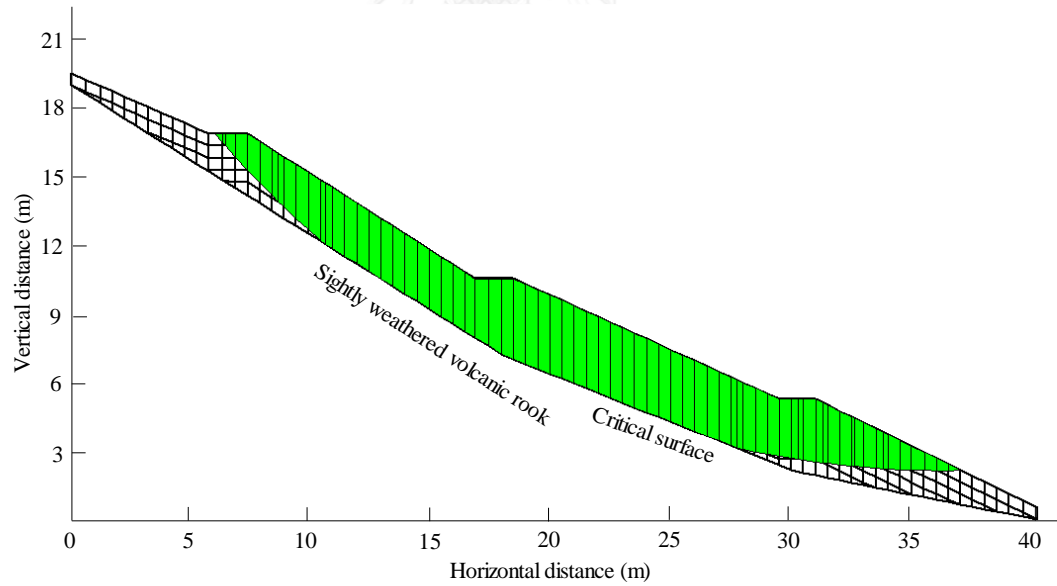
a) Uniform distribution of root (FS = 1.044)
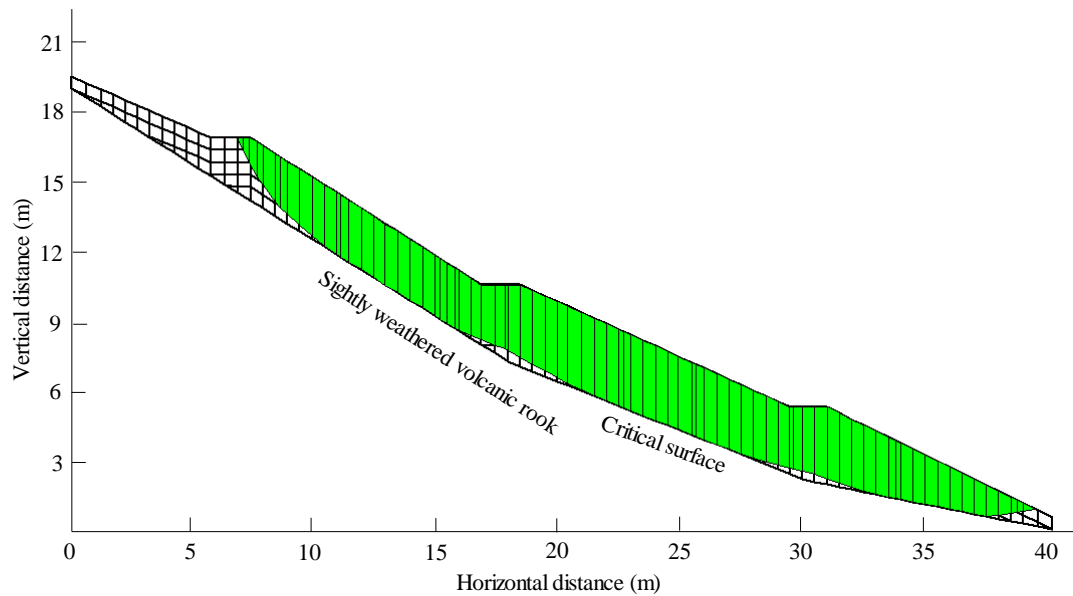
b) Triangular distribution of root (FS = 1.019)

Figure 5.27. The corresponding critical surface at typical random field of root cohesion

5.6. Summary

This chapter presented a case study of a seepage model for slopes subjected to rainfall in Thailand and the influence of vegetation on slope stability. One advantage of the finite element scheme is that it was performed using a two dimensional unsaturated-saturated seepage analysis to obtain the pore water pressure results during the period of rainfall. The conventional limit equilibrium method was expanded for an unsaturated soil slope using generalised soil suction. The extended Mohr-Coulomb failure criterion was applied to consider the root effect on soil slope stability under rainfall conditions. The rainfall intensity, the soil-water characteristics and the saturated permeability measured from the field were used to calculate pore water pressure response. The calculated results were compared with the measured values from the site to assess the effectiveness of the proposed seepage model. The pore water pressure and volumetric moisture content obtained from the seepage model were then employed in the transient unsaturated-saturated slope stability analysis. The effective soil cohesion of $c' = 12.8$ kPa was obtained from tests on well-compacted soil in the field, while zero effective soil cohesion $c' = 0$ was assumed for non-compacted soil (the worst case scenario). The influence of root cohesion on slope stability was considered by means of the root

cohesion (c_r). Factors of safety in transient seepage slope stability analysis were computed for with and without root cohesion under the worst case scenario. The available programs, SEEP/W and SLOPE/W modules, were modified to consider the effect of spatial variability of root cohesion on failure probability. Two dimensions of random fields of root cohesion were assigned to the slope stability model which was generated using a Monte Carlo simulation. The results demonstrate that the strong variability of root cohesion in space could cause slope failure even when the slope has rooted vegetation.

จุฬาลงกรณ์มหาวิทยาลัย
CHULALONGKORN UNIVERSITY

CHAPTER 6: CONCLUSIONS AND RECOMMENDATIONS

6.1. Conclusions

This research examined the effects spatial variability of parametric studies on probabilistic analysis of slope stability during heavy rainfall events. An analysis of unsaturated seepage was conducted to verify the proposed model. One dimension of random field of shear strength parameters was investigated on a sandstone slope site in Japan, while the available software program was extended to consider the effect of two dimensions of a random fields of root cohesion on residual a soil slope in Thailand.

6.1.1. Sandstone slope without vegetation in Japan

The probabilistic analysis results on the sandstone slope in Japan indicate that the critical failure surface was located at the depth of approximately 1.0 - 2.0 m below ground surface depending on the rainfall duration. The failure surface occurred at 1.7 m depth at the critical rainfall duration of 9.5 hr. The actual soil slope also failed at 1.6 m depth below ground in the period of the 1989 storm. However, the deterministic approach with infinite slope assumption reported the location of the failure surface at the base of the upper layer (i.e., 2.0 m as shown in chapter 4).

The critical failure surface was not necessarily fixed at the base of the upper layer, but changed due to the migration of wetting front as rainfall progressed. The results show that the frequency of the critical failure surface that occurs at the weakest part of the upper layer increases with increased autocorrelation length. This also agrees well with previous studies by Cho (2014) and Dou et al. (2015).

The probability framework can be used to find the critical rainfall duration corresponding to the location of the slip surface occurring at a depth of 1.7 m of the upper layer. In this study, the critical rainfall duration was obtained to indicate the slope failure during the 1989 rainstorm. The results confirm that the random field model is an essential technique to predict the slope failure due to rainfall.

A probabilistic stability analysis of rainfall-induced slope failure depends on the contribution of random fields on the shear strength parameters C and $\tan\phi$. However, it was found that the random field of C was a more important shear strength parameter

for failure probability estimation for shallow landslides. This finding can be used to verify the significance of effects of uncertain shear strength parameters of a shallow failure.

6.1.2. Residual soil slope in Thailand with vegetation

The proposed seepage model indicated that there was a better agreement between the simulated and measured pore water pressure at shallow depths rather than at deeper depths. The positive pore water pressure showed more discrepancy at Point 1 (lower part), while a conversion occurred at Point 2 (upper part). The prediction of pore water pressure demonstrated that the whole soil slope was almost completely saturated in intense storms.

The non-vegetated slope with well-compacted soil was stable during the period of rainfall, while slope instability occurred with non-compacted soil (the worst case scenario) when rainfall intensity exceeded 100 mm/day. The failure mechanism of the slope under the worst case scenario was characterised as a shallow failure in which the failure surface was located at a depth above 1.0 m, in the saturated region.

The slope stabilisation effect of vegetation was assumed to be through additional soil shear strength by root cohesion. Typical characteristics of vetiver grass in Thailand was assumed to be due to the roots in this analysis. The results showed that the factor of safety was more than 1.0 for both root cohesions, $c_r = 3.0$ and $c_r = 6.0$ kPa during the period of rainfall, and the slope with the non-compacted soil condition with vegetation became stable in the assumed heavy rainfall condition. Furthermore, a uniform distribution of root appeared to contribute more to slope stability.

The proposed method of probabilistic analysis on vegetated slope stability was conducted based on a random field model and Monte Carlo simulation. The available computer program was modified to apply both methods. The findings indicate that the vegetated slope would failed completely after the greatest rainfall intensity occurs if the cov of root cohesion was more than the critical values with any autocorrelation length. However, the vegetated slope still remained stabilized in this case which implied that the effect of the rainy season might cause an increase in cov of root cohesion not exceeding critical values. Furthermore, the effect of random fields was more important

than that of random variables on failure probability if the smaller value of cov of root cohesion was given. In addition, the effect of spatial variability of root cohesion also indicated that the smaller critical value of cov was overestimated in cases of failure probability, while greater critical values underestimated cases of failure probability at the larger autocorrelation length.

Considering the same characteristics of spatial variability of root cohesion (cov and autocorrelation length), the failure probability decreased with increasing element size. It can be concluded that the probabilistic analysis of slope stability which was investigated on a finite element model using the limit equilibrium method was more effective for natural slope. This also agrees well with previous studies by Griffiths et al. (2011) and Jiang et al. (2014).

6.2. Recommendations for further research

In this research, slope stability analysis was performed on two case studies which presented real condition of geotechnical engineering problem. This is the highlight point of this research not reported in previous studies. Furthermore, the results of this research were also compared with measured data in order to verify the effectiveness of the proposed method. In probabilistic analysis, spatial variability of parametric studies was considered in cooperation with seepage analysis in heavy rainfall events which can cause an increase in uncertainty. In addition, one strength of this research over the studies of Griffiths et al. (2011), Santoso et al. (2011), Cho (2014), and Dou et al. (2015) is that did not develop finite element codes for complex problems which can possibly lead to incorrect simulations. This research only extended and modified the available software program to perform probabilistic analysis of natural soil slopes. Thus, the contribution of this research is that it can be used in place of cumbersome models and reduce calculation time.

However, the statistical characteristics of spatial variability of shear strength parameters and root cohesion (cov and autocorrelation length) were based on observed or suggested values found in the literature re. Moreover, slope stability and probabilistic analysis only used the limit equilibrium method which may not correspond to actual phenomena of the two case studies in this research. Therefore, recommendations for further research are following:

- Statistical characteristics of spatial variability of parametric studies should be determined in actual cases based on the amount of significant data. This might avoid conservative estimates of slope stability.

- Further study on natural slope stability considering the effect of vegetation during rainfall events should be investigated using the finite element method. The root-soil component in consideration of stress-deformation analysis which can relate to the hydrological effects will be more advantageous since no assumption is given for real conditions. The failure region can occur arbitrary location within the studied problems.

- A slope will become more stable during heavy rainfall if vegetation can effect a decrease in the cov of root cohesion. Therefore, it is recommended that a plant species should be chosen whose roots growth can strongly reduce spatial variability of root cohesion.

REFERENCES

Abernethy, B., Rutherfurd, I.D., 2001. The distribution and strength of riparian tree roots in relation to riverbank reinforcement. Hydrological processes. 15(1), 63-79.

Baecher, G.B., Christian, J.T., 2003, Reliability and statistics in geotechnical engineering. Wiley. New York.

Bishop, A.W., 1955. The use of the slip circle in the stability analysis of slopes. Geotechnique. 5(1), 7-17.

Caviedes-Voullième, D., Garcı, P., Murillo, J., 2013. Verification, conservation, stability and efficiency of a finite volume method for the 1D Richards equation. Journal of Hydrology. 480, 69-84, doi: 10.1016/j.jhydrol.2012.12.008.

Chirico, G.B., Borga, M., Tarolli, P., Rigon, R., Preti, F., 2013. Role of vegetation on slope stability under transient unsaturated conditions. Procedia Environmental Sciences. 19, 932-941.

Cho, S.E., 2007. Effects of spatial variability of soil properties on slope stability. Engineering Geology. 92(3), 97-109.

Cho, S.E., 2014. Probabilistic stability analysis of rainfall-induced landslides considering spatial variability of permeability. Engineering Geology. 171, 11-20, doi: 10.1016/j.enggeo.2013.12.015.

Collison, A., Anderson, M., 1996. Using a combined slope hydrology/stability model to identify suitable conditions for landslide prevention by vegetation in the humid tropics. Earth Surface Processes and Landforms. 21(8), 737-747.

Coppin, N.J., Richards, I.G., 1990, Use of vegetation in civil engineering. Construction Industry Research and Information Association London.

Dou, H.Q., Han, T.C., Gong, X.N., Qiu, Z.Y., Li, Z.N., 2015. Effects of the spatial variability of permeability on rainfall-induced landslides. Engineering Geology. 192, 92-100, doi: 10.1016/j.enggeo.2015.03.014.

Eab, K.H., Likitlersuang, S., Takahashi, A., 2015. Laboratory and modelling investigation of root-reinforced system for slope stabilisation. Soils and Foundations. 55(5), 1270-1281.

Fatahi, B., Khabbaz, H., Indraratna, B., 2014. Modelling of unsaturated ground behaviour influenced by vegetation transpiration. Geomechanics and Geoengineering. 9(3), 187-207.

Fellenius, W., Calculation of the stability of earth dams, *in* Proceedings Transactions of the 2nd congress on large dams, Washington, DC1936, Volume 4, International Commission on Large Dams (ICOLD) Paris, p. 445-463.

Fenton, G.A., Griffiths, D.V., 2008, Risk assessment in geotechnical engineering. Jonh Wiley & Sons. New Jork.

Forsyth, P.A., Wu, Y., Pruess, K., 1995. Robust numerical methods for saturated-unsaturated flow with dry initial conditions in heterogeneous media. Advances in Water Resources. 18(1), 25-38.

Fredlund, D., Morgenstern, N.R., Widger, R., 1978. The shear strength of unsaturated soils. Canadian geotechnical journal. 15(3), 313-321, doi: 10.1139/t78-029.

Fredlund, D.G., Rahardjo, H., Fredlund, M.D., 2012, Unsaturated soil mechanics in engineering practice. John Wiley & Sons. New York.

Garga, V., Blight, G., 2012. Steady and unsteady flow of water and air through soils–permeability of saturated and unsaturated soils. Mechanics of Residual Soils, 119.

Gray, D., Sotir, R., 1996a. Biotechnical and soil bioengineering, Slope stability: A practical Guide for Erosion control. NewYork, John. Wileg&Sons.

Gray, D.H., Leiser, A.T., 1982, Biotechnical slope protection and erosion control. Van Nostrand Reinhold Company Inc.

Gray, D.H., Sotir, R.B., 1996b, Biotechnical and soil bioengineering slope stabilization: a practical guide for erosion control. John Wiley & Sons.

Greenway, D., 1987. Vegetation and slope stability. Slope stability: geotechnical engineering and geomorphology/edited by MG Anderson and KS Richards.

Greenwood, J.R., 2006. SLIP4EX–A program for routine slope stability analysis to include the effects of vegetation, reinforcement and hydrological changes. Geotechnical & Geological Engineering. 24(3), 449-465.

Griffiths, D., Lane, P., 1999. Slope stability analysis by finite elements. Geotechnique. 49(3), 387-403.

Griffiths, D., Marquez, R., 2007. Three-dimensional slope stability analysis by elasto-plastic finite elements. Geotechnique. 57(6), 537-546.

Griffiths, D.V., Huang, J., Fenton, G.A., 2011. Probabilistic infinite slope analysis. Computers and Geotechnics. 38(4), 577-584, doi: 10.1016/j.compgeo.2011.03.006.

Hasofer, A.M., Lind, N.C., 1974. Exact and invariant second-moment code format(for reliability analysis in multivariate problems). American Society of Civil Engineers, Engineering Mechanics Division, Journal. 100, 111-121.

Janbu, N., 1968. Slope stability computations, Soil Mech. and Found. Engrg. Rep., The Technical University of Norway, Trondheim, Norway.

Ji, J., Kokutse, N., Genet, M., Fourcaud, T., Zhang, Z., 2012. Effect of spatial variation of tree root characteristics on slope stability. A case study on Black Locust (Robinia pseudoacacia) and Arborvitae (Platycladus orientalis) stands on the Loess Plateau, China. Catena. 92, 139-154.

Jiang, S.-H., Li, D.-Q., Zhang, L.-M., Zhou, C.-B., 2014. Slope reliability analysis considering spatially variable shear strength parameters using a non-intrusive stochastic finite element method. Engineering Geology. 168, 120-128.

Jotisankasa, A., Mairaing, W., Tansamrit, S., Infiltration and stability of soil slope with vetiver grass subjected to rainfall from numerical modeling, *in* Proceedings Proc. of 6th the International conference on unsaturated soils, UNSAT2014, Citeseer, p. 1241-1247.

Jotisankasa, A., Porlila, W., Soralump, S., Mairiang, W., Development of a low cost miniature tensiometer and its applications, *in* Proceedings Proceedings of the 3rd Asian Conference on Unsaturated Soils (Unsat-Asia 2007), Najing, China2007.

Jotisankasa, A., Sirirattanachat, T., 2017. Effects of grass roots on soil-water retention curve and permeability function. Canadian Geotechnical Journal(ja).

Jotisankasa, A., Takahashi, A., Takeyama, T., Mairaing, W., A study of deformation behaviour of an instrumented slope subject to rainfall near Thadan dam Thailand, *in* Proceedings Proc. 14th National Convention in Civil Engineer-ing, Nakornrachasrima, Thailand2009.

Jotisankasa, A., Vathananukij, H., Investigation of soil moisture characteristics of landslide-prone slopes in Thailand, *in* Proceedings International Conference on Management of Landslide Hazard in the Asia-Pacific Region 11th-15th November2008, p. 12.

Kazutoki, A., Iwamoto, M., 1986. Preliminary Experiment on Shear in Soil Layers with a Large-Direct-Shear Apparatus. Journal of the Japanese Forestry society. 68(2), 61-65.

Kozlowski, T., 1971. Growth and development of trees. Volume II. Cambial growth, root growth, and reproduction growth. Growth and development of trees. Volume II. Cambial growth, root growth, and reproduction growth.

Lane, P., Griffiths, D., 2000. Assessment of stability of slopes under drawdown conditions. Journal of geotechnical and geoenvironmental engineering. 126(5), 443-450.

Leung, F.T., Yan, W., Hau, B.C., Tham, L., 2015. Root systems of native shrubs and trees in Hong Kong and their effects on enhancing slope stability. Catena. 125, 102-110.

Li, W.C., Lee, L.M., Cai, H., Li, H.J., Dai, F.C., Wang, M.L., 2013. Combined roles of saturated permeability and rainfall characteristics on surficial failure of homogeneous soil slope. Engineering Geology. 153, 105-113, doi: 10.1016/j.enggeo.2012.11.017.

Lin, D.-G., Huang, B.-S., Lin, S.-H., 2010. 3-D numerical investigations into the shear strength of the soil–root system of Makino bamboo and its effect on slope stability. Ecological Engineering. 36(8), 992-1006.

Low, B., 2003. Practical probabilistic slope stability analysis. Proceedings, soil and rock America. 2, 2777-2784.

Low, B.K., Tang, W.H., 2004. Reliability analysis using object-oriented constrained optimization. Structural Safety. 26(1), 69-89.

Lowe, J., Karafiath, L., Stability of earth dams upon drawdown, *in* Proceedings Proc. 1st. Pan American Conference on Soil Mechanics and Foundation Engineering, México1960, Volume 2, p. 537-552.

Lu, N., Godt, J., 2008. Infinite slope stability under steady unsaturated seepage conditions. Water Resources Research. 44(11), W11404, doi: 10.1029/2008WR006976.

Lu, N., Godt, J.W., 2013, Hillslope hydrology and stability. Cambridge University Press. New York.

Lu, N., Godt, J.W., Wu, D.T., 2010. A closed-form equation for effective stress in unsaturated soil. Water Resources Research. 46(5).

Lu, N., Likos, W.J., 2006. Suction stress characteristic curve for unsaturated soil. Journal of geotechnical and geoenvironmental engineering. 132(2), 131-142.

Lynch, J., 1995. Root architecture and plant productivity. Plant physiology. 109(1), 7.

Matsushi, Y., 2006, Triggering mechanisms and rainfall thresholds of shallow landslides on soil-mantled hillslopes with permeable and impermeable bedrocks. Dissertation: University of Tsukuba, 120 p.

Matsushi, Y., Hattanji, T., Matsukura, Y., 2006. Mechanisms of shallow landslides on soil-mantled hillslopes with permeable and impermeable bedrocks in the Boso Peninsula, Japan. Geomorphology. 76(1), 92-108, doi: 10.1016/j.geomorph.2005.10.003.

Morgenstern, N., Price, V.E., 1965. The analysis of the stability of general slip surfaces. Geotechnique. 15(1), 79-93.

O'loughlin, C., 1974. The effect of timber removal on the stability of forest soils. Journal of Hydrology (NZ). 13(2), 121-134.

Pan, L., Warrick, A., Wierenga, P.J., 1996. Finite element methods for modeling water flow in variably saturated porous media: Numerical oscillation and mass-distributed schemes. Water Resources Research. 32(6), 1883-1889, doi: 10.1029/96WR00753.

Panday, S., Huyakorn, P.S., Therrien, R., Nichols, R.L., 1993. Improved three-dimensional finite-element techniques for field simulation of variably saturated flow and transport. Journal of contaminant hydrology. 12(1-2), 3-33.

Phoon, K.K., 2008, Reliability-based design in geotechnical engineering: computations and applications. Taylor & Francis. London & New York.

Phoon, K.K., Kulhawy, F.H., 1999. Characterization of geotechnical variability. Canadian Geotechnical Journal. 36(4), 612-624, doi: 10.1139/t99-038.

Rahardjo, H., Satyanaga, A., Leong, E.C., 2012. Unsaturated soil mechanics for slope stabilization. Southeast Asian Geotechnical Journal. 43(1), 48-58.

Ray, R.L., Jacobs, J.M., Pedro, d.A., 2010. Impacts of unsaturated zone soil moisture and groundwater table on slope instability. Journal of geotechnical and geoenvironmental engineering. 136(10), 1448-1458, doi: 10.1061/(ASCE)GT.1943-5606.0000357.

Retheti, L., 1988, Probabilistic solutions in geotechnics. Pub. Co. Elsevier Science.

Richards, L.A., 1931. Capillary conduction of liquids through porous mediums. Journal of Applied Physics. 1(5), 318-333, doi: 10.1063/1.1745010.

Royal Irrigation Deparment, 2004, Report on source areas for rock and aggregates in Klong Thadan Dam construction project.

Sainak, A., JARDINE, R., POTTS, D., HIGGINS, K., SAINAK, A., Application of three-dimensional finite element method in parametric and geometric studies of slope stability analysis, *in* Proceedings ADVANCES IN GEOTECHNICAL ENGINEERING-THE SKEMPTON CONFERENCE. A THREE DAY CONFERENCE ON ADVANCES IN ENGINEERING, ORGANISED BY THE INSTITUTION OF CIVIL ENGINEERS, HELD AT THE ROYAL GEOGRAPHICAL SOCIETY, LONDON, 29-31 MARCH 20042004, Volume 39.

Santoso, A.M., Phoon, K.-K., Quek, S.-T., 2011. Effects of soil spatial variability on rainfall-induced landslides. Computers & Structures. 89(11), 893-900, doi: 10.1016/j.compstruc.2011.02.016.

Schmid, A., Dordick, J., Hauer, B., Kiener, A., Wubbolts, M., Witholt, B., 2001. Industrial biocatalysis today and tomorrow. Nature. 409(6817), 258-268.

Schmidt, K., Roering, J., Stock, J., Dietrich, W., Montgomery, D., Schaub, T., 2001. The variability of root cohesion as an influence on shallow landslide susceptibility in the Oregon Coast Range. Canadian Geotechnical Journal. 38(5), 995-1024.

Seki, K., 2007. SWRC fit-a nonlinear fitting program with a water retention curve for soils having unimodal and bimodal pore structure. Hydrology and Earth System Sciences Discussions Discussions. 4(1), 407-437, doi: 10.5194/hessd-4-407-2007.

Simon, A., Collison, A.J., 2002. Quantifying the mechanical and hydrologic effects of riparian vegetation on streambank stability. Earth Surface Processes and Landforms. 27(5), 527-546.

Smith, I., Griffiths, D., 2004. Programming the finite element method.

Smith, I., Hobbs, R., 1974. Finite element analysis of centrifuged and built-up slopes. Geotechnique. 24(4), 531-559.

Society, 1995. Geological Society Engineering Group Working Party Report: The description and classification of weathered rocks for engineering purposes. Quarterly Journal of Engineering Geology. 28, 207-242, doi: 10.1144/GSL.QJEG.1970.003.01.01.

Spencer, E., 1967. A method of analysis of the stability of embankments assuming parallel inter-slice forces. Geotechnique. 17(1), 11-26.

Srivastava, A., Babu, G.S., Haldar, S., 2010. Influence of spatial variability of permeability property on steady state seepage flow and slope stability analysis. Engineering Geology. 110(3), 93-101, doi: 10.1016/j.enggeo.2009.11.006.

Takeuchi, J., Kawachi, T., Imagawa, C., Buma, N., Unami, K., Maeda, S., 2010. A physically based FVM watershed model fully coupling surface and subsurface water flows. Paddy and Water Environment. 8(2), 145-156.

Terwilliger, V.J., Waldron, L.J., 1991. Effects of root reinforcement on soil-slip patterns in the Transverse Ranges of southern California. Geological Society of America Bulletin. 103(6), 775-785.

Tiwari, R., Bhandary, N., Yatabe, R., Bhat, D., 2013. New numerical scheme in the finite-element method for evaluating the root-reinforcement effect on soil slope stability. Geotechnique. 63(2), 129.

Van Dam, J.C., Feddes, R.A., 2000. Numerical simulation of infiltration, evaporation and shallow groundwater levels with the Richards equation. Journal of Hydrology. 233(1), 72-85, doi: 10.1016/s0022-1694(00)00227-4.

van Genuchten, M.T., 1980. A closed-form equation for predicting the hydraulic conductivity of unsaturated soils. Soil science society of America journal. 44(5), 892-898, doi: 10.2136/sssaj1980.03615995004400050002x.

Vanmarcke, E., 1983, Random fields: Analysis and synthesis. The MIT Press. Cambridge.

Vanmarke, E., 1977. Random vibration approach to soil dynamics. The use of probability in Annexes.

Vergani, C., Chiaradia, E., Bischetti, G., 2012. Variability in the tensile resistance of roots in Alpine forest tree species. Ecological engineering. 46, 43-56.

Wakatsuki, T., Tanaka, Y., Matsukura, Y., 2005. Soil slips on weathering-limited slopes underlain by coarse-grained granite or fine-grained gneiss near Seoul, Republic of Korea. Catena. 60(2), 181-203, doi: 10.1016/j.catena.2004.11.003.

Waldron, L., 1977. The shear resistance of root-permeated homogeneous and stratified soil. Soil Science Society of America Journal. 41(5), 843-849.

Wu, T.H., 2013. Root reinforcement of soil: review of analytical models, test results, and applications to design. Canadian Geotechnical Journal. 50(3), 259-274.

Wu, T.H., Beal, P.E., Lan, C., 1988. In-situ shear test of soil-root systems. Journal of Geotechnical Engineering. 114(12), 1376-1394.

Wu, T.H., McKinnell III, W.P., Swanston, D.N., 1979. Strength of tree roots and landslides on Prince of Wales Island, Alaska. Canadian Geotechnical Journal. 16(1), 19-33.

Wu, T.H., Watson, A., 1998. In situ shear tests of soil blocks with roots. Canadian Geotechnical Journal. 35(4), 579-590.

Zambra, C., Dumbser, M., Toro, E., Moraga, N., 2012. A novel numerical method of high-order accuracy for flow in unsaturated porous media. International Journal for Numerical Methods in Engineering. 89(2), 227-240.

Zarba, R.L., Bouloutas, E., Celia, M., 1990. General mass-conservative numerical solution for the unsaturated flow equation. Water Resources Research WRERAQ. 26(7), 1483-1496.

Zhu, H., Zhang, L.M., Xiao, T., Li, X., 2017. Enhancement of slope stability by vegetation considering uncertainties in root distribution. Computers and Geotechnics. 85, 84-89.

Zienkiewicz, O.C., 1975. Methode der finiten Elemente. Muenchen: Hanser, 1975.

APPENDIX

A1. Program for spectral density function

```
% Simulation of normal random process using the two-sided power spectral density
function, S(f)
function [sigma,A,B,wax,way,x,y,nfx,nfy] =
two_dimension_spectral(nex,ney,dx,dy,lx,ly,n_MCS)
% Frequency interval, delfx,delfy
delfx = 1/nex/dx;
delfy = 1/ney/dy;
% Discretization of autocorrelation function, R(taux,tauy)
taux = zeros(1,nex);
tauy = zeros(1,ney);
taux = -(nex/2-1)*dx:dx:(nex/2)*dx;
tauy = -(ney/2-1)*dy:dy:(ney/2)*dy;
R = zeros(ney,nex);
for k=1:ney
    for m=1:nex
        R(k,m)=exp(-2*abs(taux(m))/lx)*exp(-2*abs(tauy(k))/ly);
    end
end
% Numerical calculation of S(f) using FFT
H = zeros(ney,nex);
H = fft2(R);
fx=zeros(1,nex);
fy=zeros(ney,1);
S=zeros(ney,nex);
% Shuffle f to correspond with frequencies ordering implied in H
fx(1,1)=0;
fy(1,1)=0;
for m=2:nex/2+1;
    fx(1,m)=fx(1,m-1)+delfx;
end;
fx(1,nex/2+2) = -fx(1,nex/2+1)+delfx;
for m = nex/2+3:nex;
    fx(1,m) = fx(1,m-1)+delfx;
end;
for k=2:ney/2+1;
    fy(k,1)=fy(k-1,1)+delfy;
end;
fy(ney/2+2,1) = -fy(ney/2+1,1)+delfy;
for k = ney/2+3:ney;
    fy(k,1) = fy(k-1,1)+delfy;
end;
tau0x = (nex/2-1)*dx;
tau0y = (ney/2-1)*dy;
for k=1:ney
```

```
    for m=1:nex
        S(k,m)=H(k,m)*exp(2*pi*i*(fx(1,m)*tau0x+fy(k,1)*tau0y))*dx*dy;
    end
end
S = real(S); % remove possible imaginary parts due to roundoff errors
% Shuffle S to correspond with f in increasing order
fx = -(nex/2-1)*delfx:delfx:(nex/2)*delfx;
fy = transpose(-(ney/2-1)*delfy:delfy:(ney/2)*delfy);
tempx = zeros(ney,nex);

for m=1:nex/2-1;
    tempx(:,m)=S(:,m+nex/2+1);
end;
for m=nex/2:nex;
    tempx(:,m)=S(:,m-nex/2+1);
end;
tempy = zeros(ney,nex);
for k=1:ney/2;
    tempy(k,:)=tempx(k+ney/2,:);
end;
for k=ney/2+1:ney;
    tempy(k,:)=tempx(k-ney/2,:);
end;
S=tempy;
clear tempx;
clear tempy;
% Simulation of normal process using spectral representation with mean of process =
0 and variance of process = 1
Lxmax = 1/delfx;
Lymax = 1/delfy;
Lx = 0.5*Lxmax;
Ly = 0.5*Lymax;
% Number of simulated data points, nx,ny
% Depth sampling interval, dx,dy
% Coordinates in x direction, x(1), x(2) ... x(nx)
% Coordinates in x direction, y(1), y(2) ... y(ny)
nx = round(Lx/dx);
ny = round(Ly/dy);
delx = Lx/nx;
dely = Ly/ny;
x = delx:delx:Lx;
y = dely:dely:Ly;
% Number of positive frequencies in the spectral expansion, nf = N/2
nfx = nex/2;
nfy = ney/2;
% Simulate uncorrelated standard normal random variables sigma = zeros(nfy,nfx);
% Calculate energy at each frequency using trapezoidal rule, 4*S(f)
```

```
for k = 1:nfy
   for m = 1:nfx;
      sigma1 = S(nfy-k+2,m+nfx-1);
      sigma2 = S(nfy-k+2,m+nfx);
      sigma3 = S(nfy-k+1,m+nfx-1);
      sigma4 = S(nfy-k+1,m+nfx);
      sigma(k,m) = 4*(sigma1+sigma2+sigma3+sigma4)*0.25*delfx*delfy;
   end
end
sigma = sigma.^0.5;
wax = zeros(1,nfx);
for m = 1:nfx
   wax(m) = 0.5*2*pi*(fx(m+nfx-1)+fx(m+nfx));
end
way = zeros(1,nfy);
for k = 1:nfy
   way(k) = 0.5*2*pi*(fy(k+nfy-1)+fy(k+nfy));
end
randn('state',1);
Z = random('Normal',0,1,2*nfy,2*nfx,n_MCS);
A = Z(1:nfy,1:nfx,:);
B = Z(nfy+1:2*nfy,nfx+1:2*nfx,:);
```

A2. Program for standard normal distribution

```
function [X] = normal_X(lx,ly,dx,dy,n_MCS,nx,ny)
% Number of data points based on power of 2, N
nex=158;
ney=34;
 [sigma,A,B,wax,way,x,y,nfx,nfy] =
two_dimension_spectral(nex,ney,dx,dy,lx,ly,n_MCS);
for l = 1:n_MCS
   for k = 1:nfy
      for m = 1:nfx
         xi = x(m);
         yj = y(k);
         [Xij] = random_Xij(nfx,nfy,sigma,A,B,wax,way,xi,yj,l);
         X(k,m,l)=Xij;
      end
   end
end
X=X(1:ny,1:nx,:);
function [Xij] = random_Xij(nfx,nfy,sigma,A,B,wax,way,xi,yj,l)
Xij = 0;
for j = 1:nfy
   for i = 1:nfx
      Xij =
Xij+sigma(j,i)*(A(j,i,l)*cos(wax(i)*xi+way(j)*yj)+B(j,i,l)*sin(wax(i)*xi+way(j)*yj));
```

```
      end
end
```

A3. Program for random field

```
function [cr] = randomfield(lx,ly,mean_cr,cov_cr,n_MCS,matrix_e,size_e)
% Sampling interval,dx,dy
dx=0.5;
dy=0.5;
nx=79;
ny=17;
[X] = normal_X(lx,ly,dx,dy,n_MCS,nx,ny);
% Lognormal x (consider variance reduction)
x_lncr = sqrt(log(1+cov_cr^2));
m_lncr = log(mean_cr)-0.5*x_lncr^2;
% Simulation of random field
k=0;
for i=1:nx
    for j=1:ny
        if matrix_e(j,i)>0
        k=k+1;
        % Variance reduction
        gT=(lx^2*ly^2)/(4*size_e(k,1)^2*size_e(k,2)^2)*(2*size_e(k,1)/lx+exp(-
        2*size_e(k,1)/lx)-1)*(2*size_e(k,2)/ly+exp(-2*size_e(k,2)/ly)-1);
        m_crT = exp(m_lncr+0.5*x_lncr^2*gT);
        x_crT = m_crT*sqrt(exp(x_lncr^2*gT)-1);
        cov_crT = x_crT/m_crT;
        x_lncrT = sqrt(log(1+cov_crT^2));
        m_lncrT = log(m_crT)-0.5*x_lncrT^2;
        Rad_crT(k,:)= m_lncrT + X(j,i,:)*x_lncrT;
          end
    end
end
cr=exp(Rad_crT);
```

A4. Program for modifying "FS" input file

```
ct = transpose(cr);
for j=1:500
    R = ct(j,:);
    xmlfile = fullfile('Slope_cr.xml');
    DOMnode = xmlread(xmlfile);
    d = DOMnode.getElementsByTagName('Analysis');
    e = d.item(0).getElementsByTagName('Name');
    e.item(0).setTextContent(genvarname(num2str(j)));
    for i=1:380
        a = DOMnode.getElementsByTagName('Material');
        b = a.item(i).getElementsByTagName('StressStrain');
```

```
      c = b.item(0).getElementsByTagName('SlopeCohesion');
      c.item(0).setTextContent(num2str(R(1,i)));
   end
   xmlwrite([genvarname(num2str(j)),'.xml'],DOMnode);
end
```

A5. Program for "FS" output file

```
delimiterIn = 'S';
headerlinesIn = 2017;
for i=1:500
  A = importdata([genvarname(num2str(i)),'.fac'],delimiterIn,headerlinesIn);
  B = cell2mat(A(2017,1));
  C = str2num(B(1,58:65));
  FS(i,:) = C;
end
```

B1. "FS" input file for slope stability analysis.

```xml
            </Regions>
        </GeometryItems>
        <Materials Len="962">
            <Material>
                <ID>1</ID>
                <Color>RGB=(255,255,128)</Color>
                <Name>(1)</Name>
                <SlopeModel>MohrCoulomb</SlopeModel>
                <StressStrain>
                    <SlopeSuctionModel>Function</SlopeSuctionModel>
                    <UnitWeight>17.61</UnitWeight>
                    <SlopeCohesion>3</SlopeCohesion>
                    <SlopePhi>33.1</SlopePhi>
                </StressStrain>
                <Hydraulic VolWCFnNum="1" />
            </Material>
            <Material>
                <ID>2</ID>
                <Color>RGB=(191,255,128)</Color>
                <Name>(2)</Name>
                <SlopeModel>MohrCoulomb</SlopeModel>
                <StressStrain>
                    <SlopeSuctionModel>Function</SlopeSuctionModel>
                    <UnitWeight>17.61</UnitWeight>
                    <SlopeCohesion>3</SlopeCohesion>
                    <SlopePhi>33.1</SlopePhi>
                </StressStrain>
                <Hydraulic VolWCFnNum="1" />
            </Material>
            <Material>
                <ID>3</ID>
                <Color>RGB=(128,255,128)</Color>
                <Name>(3)</Name>
                <SlopeModel>MohrCoulomb</SlopeModel>
                <StressStrain>
                    <SlopeSuctionModel>Function</SlopeSuctionModel>
                    <UnitWeight>17.61</UnitWeight>
                    <SlopeCohesion>3</SlopeCohesion>
                    <SlopePhi>33.1</SlopePhi>
                </StressStrain>
                <Hydraulic VolWCFnNum="1" />
            </Material>
            <Material>
                <ID>4</ID>
                <Color>RGB=(128,255,191)</Color>
                <Name>(4)</Name>
                <SlopeModel>MohrCoulomb</SlopeModel>
                <StressStrain>
                    <SlopeSuctionModel>Function</SlopeSuctionModel>
                    <UnitWeight>17.61</UnitWeight>
                    <SlopeCohesion>3</SlopeCohesion>
```

B2. "Run_MCS" file for *n* simulation of slope stability analysis.

```
Run_MCS.bat - Notepad
File  Edit  Format  View  Help
"C:\Program Files (x86)\GEO-SLOPE\GeoStudio2007\Bin\GeoStudio.exe" "D:\Slope_Thadan
(Journal)\Probabilistic analysis\x1.xml" "x1" /solve
"C:\Program Files (x86)\GEO-SLOPE\GeoStudio2007\Bin\GeoStudio.exe" "D:\Slope_Thadan
(Journal)\Probabilistic analysis\x2.xml" "x2" /solve
"C:\Program Files (x86)\GEO-SLOPE\GeoStudio2007\Bin\GeoStudio.exe" "D:\Slope_Thadan
(Journal)\Probabilistic analysis\x3.xml" "x3" /solve
"C:\Program Files (x86)\GEO-SLOPE\GeoStudio2007\Bin\GeoStudio.exe" "D:\Slope_Thadan
(Journal)\Probabilistic analysis\x4.xml" "x4" /solve
"C:\Program Files (x86)\GEO-SLOPE\GeoStudio2007\Bin\GeoStudio.exe" "D:\Slope_Thadan
(Journal)\Probabilistic analysis\x5.xml" "x5" /solve
"C:\Program Files (x86)\GEO-SLOPE\GeoStudio2007\Bin\GeoStudio.exe" "D:\Slope_Thadan
(Journal)\Probabilistic analysis\x6.xml" "x6" /solve
"C:\Program Files (x86)\GEO-SLOPE\GeoStudio2007\Bin\GeoStudio.exe" "D:\Slope_Thadan
(Journal)\Probabilistic analysis\x7.xml" "x7" /solve
"C:\Program Files (x86)\GEO-SLOPE\GeoStudio2007\Bin\GeoStudio.exe" "D:\Slope_Thadan
(Journal)\Probabilistic analysis\x8.xml" "x8" /solve
"C:\Program Files (x86)\GEO-SLOPE\GeoStudio2007\Bin\GeoStudio.exe" "D:\Slope_Thadan
(Journal)\Probabilistic analysis\x9.xml" "x9" /solve
"C:\Program Files (x86)\GEO-SLOPE\GeoStudio2007\Bin\GeoStudio.exe" "D:\Slope_Thadan
(Journal)\Probabilistic analysis\x10.xml" "x10" /solve
"C:\Program Files (x86)\GEO-SLOPE\GeoStudio2007\Bin\GeoStudio.exe" "D:\Slope_Thadan
(Journal)\Probabilistic analysis\x11.xml" "x11" /solve
"C:\Program Files (x86)\GEO-SLOPE\GeoStudio2007\Bin\GeoStudio.exe" "D:\Slope_Thadan
(Journal)\Probabilistic analysis\x12.xml" "x12" /solve
"C:\Program Files (x86)\GEO-SLOPE\GeoStudio2007\Bin\GeoStudio.exe" "D:\Slope_Thadan
(Journal)\Probabilistic analysis\x13.xml" "x13" /solve
"C:\Program Files (x86)\GEO-SLOPE\GeoStudio2007\Bin\GeoStudio.exe" "D:\Slope_Thadan
(Journal)\Probabilistic analysis\x14.xml" "x14" /solve
"C:\Program Files (x86)\GEO-SLOPE\GeoStudio2007\Bin\GeoStudio.exe" "D:\Slope_Thadan
(Journal)\Probabilistic analysis\x15.xml" "x15" /solve
"C:\Program Files (x86)\GEO-SLOPE\GeoStudio2007\Bin\GeoStudio.exe" "D:\Slope_Thadan
(Journal)\Probabilistic analysis\x16.xml" "x16" /solve
"C:\Program Files (x86)\GEO-SLOPE\GeoStudio2007\Bin\GeoStudio.exe" "D:\Slope_Thadan
(Journal)\Probabilistic analysis\x17.xml" "x17" /solve
"C:\Program Files (x86)\GEO-SLOPE\GeoStudio2007\Bin\GeoStudio.exe" "D:\Slope_Thadan
(Journal)\Probabilistic analysis\x18.xml" "x18" /solve
"C:\Program Files (x86)\GEO-SLOPE\GeoStudio2007\Bin\GeoStudio.exe" "D:\Slope_Thadan
(Journal)\Probabilistic analysis\x19.xml" "x19" /solve
"C:\Program Files (x86)\GEO-SLOPE\GeoStudio2007\Bin\GeoStudio.exe" "D:\Slope_Thadan
(Journal)\Probabilistic analysis\x20.xml" "x20" /solve
"C:\Program Files (x86)\GEO-SLOPE\GeoStudio2007\Bin\GeoStudio.exe" "D:\Slope_Thadan
(Journal)\Probabilistic analysis\x21.xml" "x21" /solve
"C:\Program Files (x86)\GEO-SLOPE\GeoStudio2007\Bin\GeoStudio.exe" "D:\Slope_Thadan
(Journal)\Probabilistic analysis\x22.xml" "x22" /solve
"C:\Program Files (x86)\GEO-SLOPE\GeoStudio2007\Bin\GeoStudio.exe" "D:\Slope_Thadan
(Journal)\Probabilistic analysis\x23.xml" "x23" /solve
"C:\Program Files (x86)\GEO-SLOPE\GeoStudio2007\Bin\GeoStudio.exe" "D:\Slope_Thadan
(Journal)\Probabilistic analysis\x24.xml" "x24" /solve
"C:\Program Files (x86)\GEO-SLOPE\GeoStudio2007\Bin\GeoStudio.exe" "D:\Slope_Thadan
(Journal)\Probabilistic analysis\x25.xml" "x25" /solve
"C:\Program Files (x86)\GEO-SLOPE\GeoStudio2007\Bin\GeoStudio.exe" "D:\Slope_Thadan
```

B3. "FS" output file.

```
FS.fac - Notepad

File  Edit  Format  View  Help

 985     33.060     20.147     18.183     3     0.0000     1.1749585     1.0856724
 986     31.757     17.043     15.481     1     0.0000     1.0859457     1.1981837
 986     31.757     17.043     15.481     3     0.0000     1.2589537     1.1372764
 987     30.815     14.800     13.712     1     0.0000     1.1089444     1.2236678
 987     30.815     14.800     13.712     4     0.0000     1.3155252     1.1648648
 988     30.090     13.073     12.503     1     0.0000     1.1081970     1.2206544
 988     30.090     13.073     12.503     4     0.0000     1.3464573     1.1732678
 989     29.506     11.681     11.657     1     0.0000     1.0867987     1.2108753
 989     29.506     11.681     11.657     4     0.0000     1.3792532     1.1643998
 990     29.017     10.517     11.059     1     0.0000     1.0885950     1.2123392
 990     29.017     10.517     11.059     4     0.0000     1.4322637     1.1750568
 991     94.079    160.136    168.325     0     0.0000 993.0000000 993.0000000
 991     94.079    160.136    168.325     0     0.0000 993.0000000 993.0000000
 992     49.960     56.690     56.598     1     0.0000     1.4493867     1.4508596
 992     49.960     56.690     56.598     4     0.0000     1.4542217     1.4519134
 993     41.021     35.731     34.546     1     0.0000     1.1869982     1.2137701
 993     41.021     35.731     34.546     4     0.0000     1.2284217     1.2006940
 994     37.108     26.555     25.305     1     0.0000     1.0820659     1.1333230
 994     37.108     26.555     25.305     4     0.0000     1.1599046     1.1082905
 995     34.870     21.308     20.334     1     0.0000     1.0772116     1.1619116
 995     34.870     21.308     20.334     3     0.0000     1.2000567     1.1140376
 996     33.393     17.846     17.304     1     0.0000     1.1047202     1.2149061
 996     33.393     17.846     17.304     3     0.0000     1.2633130     1.1483776
 997     32.327     15.345     15.319     1     0.0000     1.1174994     1.2296702
 997     32.327     15.345     15.319     4     0.0000     1.2955097     1.1611632
 998     31.506     13.422     13.961     1     0.0000     1.1072736     1.2260148
 998     31.506     13.422     13.961     4     0.0000     1.3121358     1.1578264
 999     30.845     11.871     13.010     1     0.0000     1.0893670     1.2245304
 999     30.845     11.871     13.010     4     0.0000     1.3436116     1.1503487
1000     30.293     10.576     12.335     1     0.0000     1.0995403     1.2374613
1000     30.293     10.576     12.335     4     0.0000     1.4087461     1.1707628


      -----------------------------------------
      || SUMMARY OF MINIMUM FACTORS OF SAFETY |
      -----------------------------------------
      MOMENT EQUILIBRIUM: FELLENIUS OR ORDINARY METHOD
            41.9194=X-COOR.       57.9418=Y-COOR.       55.9460=RADIUS      1.0316763=F.S.
      283=SLIP#
      MOMENT EQUILIBRIUM: BISHOP SIMPLIFIED METHOD
            41.9194=X-COOR.       57.9418=Y-COOR.       55.9460=RADIUS      1.0614193=F.S.
      283=SLIP#
      FORCE EQUILIBRIUM: JANBU SIMPLIFIED METHOD (NO fo FACTOR)
            41.9194=X-COOR.       57.9418=Y-COOR.       55.9460=RADIUS      1.0410637=F.S.
      283=SLIP#


      NORMAL TERMINATION OF SLOPE

      MOST_CRITICAL #       SLIP_SURFACE #
      =================================
              1                 283
```

VITA